Università degli Studi di Ferrara

DOTTORATO DI RICERCA IN
"Scienze Chimiche"

CICLO XXX

COORDINATORE Prof. Carlo Alberto Bignozzi

Cyclodextrin and silica-based nanomaterials as new antibiotics carrier systems

Settore Scientifico Disciplinare CHIM/03

Dottorando	**Tutore**
Dott. Wankar Jitendra	Prof. Maria Teresa Indelli

(firma)   *(firma)*

Tutore esterno
Dott.ssa Ilse G. J. Manet

(firma)

Anni 2014/2017

Acknowledgements

Jitendra Wankar

Table of contents

Abstract

My research activity to obtain the PhD degree makes part of the 7FP-ITN CyclonHit project entitled "NANOCARRIERS FOR THE DELIVERY OF ANTIMICROBIAL AGENTS TO FIGHT RESISTANCE MECHANISMS". The aim of my research project was to identify new nanosize materials as delivery systems of known antibiotics in order to improve their administration perspectives and enhance their bioavailability and efficacy. In particular, we have studied in collaboration with consortium partners the interaction of Ethionamide (ETH) and Clofazimine (CLZ), two known antibiotics, with cyclodextrin- and silica-based nanomaterials as carriers.

Ethionamide interaction with cyclodextrin carriers

ETH is a well known second-line antituberculosis drug. This drug requires high therapeutic doses causing severe side effects and suffers from administration drawbacks due to its very low aqueous solubility and tendency to crystallize. To solve the solubility problem of the drug and improve its bioavailability, we chose a molecular complexation strategy with well established cyclodextrin-based nanocarriers. Optical spectroscopic techniques were used to understand the binding of ETH with natural βCyclodextrin (βCyD) as model, an epichlorohydrin-crosslinked βCyD polymer (pβCyD), a FITC-labeled βCyD polymer (FITC-pβCyD) and a γCyclodextrin (γCyD) oligomer labeled with nitrobenzofurazan.

ETH	CD spectra of ETH with increasing amount of pβCyD	Phase solubility diagram of ETH with pβCyD (red) and βCyD (blue)
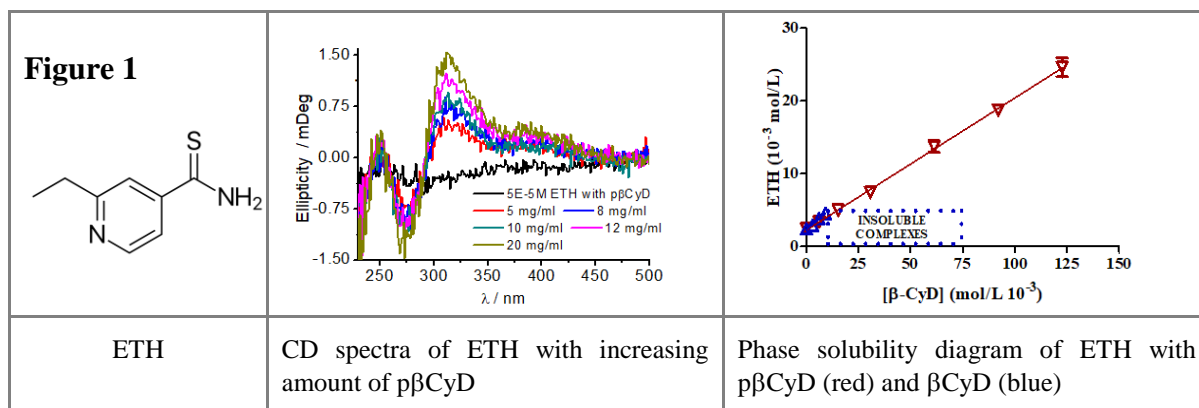
ETH is a non-fluorescent molecule and is not chiral, consequently it does not have any CD signal; anyway, complexation by the chiral CyD environment gives rise to an induced CD signal as shown in Figure 1 for pβCyD where ETH concentration is kept constant and pβCyD concentration increases. Performing a global analysis of multiwavelength data it was possible to calculate the binding constants: $\log(K_{1:1}/M^{-1})$ values of 1.7 for βCyD and FITC-pβCyD and 2.0 for pβCyD were found, assuming a 1:1 complexation model and expressing concentration in βCyD units. Remarkably, 4.2 mg/ml ETH could be dissolved

with 200 mg/ml pβCyD without the use of organic solvents, corresponding to a drug loading of about 2.1%. The hydrodynamic diameter of ca. 30 nm of the pβCyD particles does not change upon drug loading. Interestingly the FITC fluorescence intensity improves upon drug loading, an interesting feature for further development of the drug carrier system.

Ethionamide and booster co-encapsulation in pβCyD

It is known that a ten-fold improved efficacy of ETH can be obtained when co-administered with a booster. Boosters are synthetic organic molecules often insoluble in water representing a drawback for their practical use. In this context we studied the *contemporary* loading of ETH and booster in the pβCyD polymer. First, binding of five different boosters with the pβCyD polymer was studied. We have monitored the binding by means of different spectroscopic techniques like absorption, fluorescence, and circular dichroism. Multiwavelenght global analysis of the titration data afforded binding constants with $\log(K_{1:1}/M^{-1})$ values ranging from 2.28 to 3.37. Next, we studied spectroscopically the co-encapsulation of ETH and BDM43266 (Figure 2) in pβCyD in more detail including also molecular modeling and investigated competition between the two molecules for single βCyD cavities by means of phase solubility experiments.

Figure 2		
Booster BDM43266	Fluorescence spectra of booster BDM43266 with increasing amount of pβCyD; exc. at 280 nm	Phase solubility diagrams of ETH in pβCyD (∇), in pβCyD NPs followed by addition of BDM43266 (∇), and in pβCyD NPs containing Booster (∇).
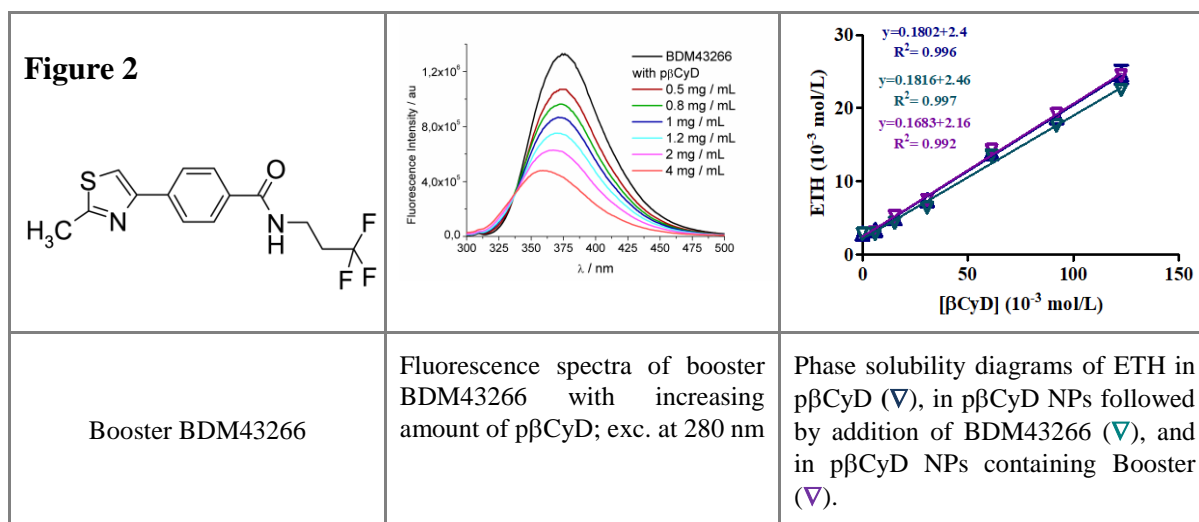
Interestingly, co-encapsulation of ETH and booster in the polymer is feasible and ETH and BDM43266, with solubility in water of 0.48 mg/ml and 0.01 mg/ml respectively, were successfully incorporated in pβCyD. Phase solubility diagrams indicated the polymer aqueous solution is able to dissolve both solid drug and booster resulting in 4.2 mg/ml dissolved drug amount and 1.2 mg/ml booster amount with 200 mg/ml pβCyD (Figure. 2). Also spectroscopic results show that the polymer is able to complex both molecules when

applying a molar concentration ratio [ETH]/[BDM43266] of 10:1. Circular Dichroism provided the evidence of ETH binding whereas interaction of a BDM-43266 with the same polymer was confirmed by fluorescence of the booster (see image in Figure 2). The booster did not acquire an induced CD signal indicative of conformational flexibility of the complex. In line with this result, molecular modeling afforded complex structures of ETH/βCyD and Booster/βCyD with features supporting the presence and absence of induced CD signals, respectively. Particle size slightly increases upon ETH and Booster co-encapsulation. The aqueous formulation of the polymer loading both drug and booster resulted suitable for microsprayer application.

Clofazimine interaction with SBE-βCyD-based carriers

We studied the encapsulation of the antileprosy drug CLZ, totally insoluble in water, with the sulfobutylether (SBE)-βCyD monomer and the epichlorohydrin-crosslinked polymer, SBE-pβCyD, and the rhodamine (Rho) labeled analogues. The monomers and polymers behaved as excellent solubilising tool for CLZ in film form and interaction was strongly supported by the data obtained from circular dichroism (see Figure 3). CLZ is not chiral but upon complexation with SBE-βCyD carriers, it acquired an induced CD signal confirming the CLZ interaction with SBE-βCyD and SBE-pβCyD. We managed to load up to 0.5 mg/ml drug in SBE-pβCyD without the use of any organic solvent. With the polymeric carriers we obtained nanoparticles with diameter in the 20 to 70 nm range. Microfiltration did not cause any loss in material. We have studied the polymer molar mass, particle size and CLZ encapsulation also by using AF4-MALS fractionation technique in collaboration with the CyclonHit private partner ByFlow. Gyration radius of the SBE-pβCyD nanoparticles changed upon drug loading: r_g value of 30.5 nm without CLZ and 22.3 nm with CLZ . This may be due to the drug presence inside the polymeric nanoparticle resulting in a more compact particle as more than one CyD unit may be participating in a single CLZ molecule complexation. A similar decrease in particle dimension was observed for the CLZ loaded polymer in DLS analysis. We measured a polymer molar mass value of around 53kDa. We performed a
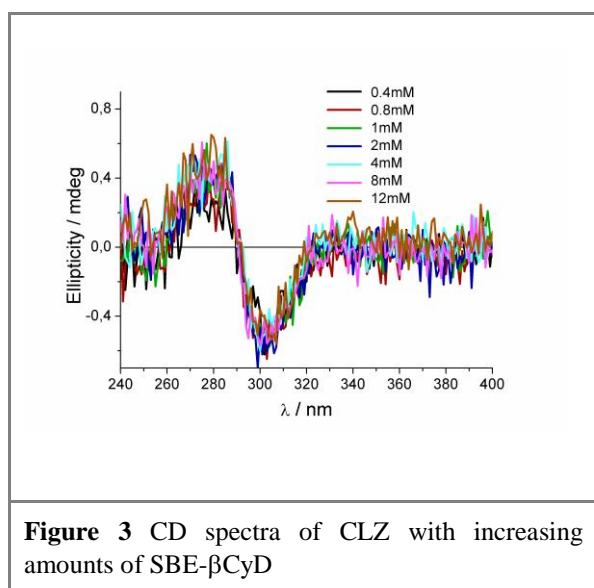
Figure 3 CD spectra of CLZ with increasing amounts of SBE-βCyD

similar experiment for Rho-labeled SBE-pβCyD with and without CLZ. It has a similar molar mass value. Differently, the gyration radius r_g value for the CLZ loaded Rho-SBE-pβCyD has a value of 60 nm larger than that without CLZ of 50 nm. The latter value can be explained assuming that the presence of Rho moieties, residing on the surface, induces aggregation phenomena of these particles. When both Rho and CLZ are present, other factors are likely playing a role like electrostatic repulsion between Rho and CLZ both bearing a positive charge. The loaded carriers were tested on their cytotoxicity and bactericidal activity. Of utmost importance, the encapsulated drug is not cytotoxic in VERO cell model up to 5 μM, while the drug alone is highly cytotoxic. Also the carriers alone are not cytotoxic in the range explored. Among the tested bacteria the best results were obtained with *S. epidermidis*. The drug has MIC_{50} values below 100 nM, similar to those of CLZ alone. The same holds also for the clinical isolates of *S. epidermidis*, some displaying MDR. We also performed *in vitro* drug release tests of CLZ/SBE-βCyD carrier systems through cellulose dialysis membranes (MW cut off 1600 Da) using a Franz diffusion cell but the results obtained are not promising as the membrane blocks the drug.

Clofazimine encapsulation in fluorescent mesoporous silica particles

We studied fluorescent mesoporous silica particles as CLZ carriers for theranostic applications. We developed silica particles with intrinsic luminescence not requiring the labeling with a fluorescent dye. Particle size, porosity, drug loading and photophysical features of the silica particles were thoroughly explored. Aminofunctionalisation followed by calcination up to 400°C resulted in the formation of fluorescent particles likely due to carbon dots formed in the pores. Suspensions of fluorescent silica particles, loaded and not with CLZ, were excited at different wavelengths. The fluorescence spectra shifted to the red with increasing excitation wavelength supporting the hypothesis of carbon dots inside the silica particles. Interestingly, the absorption and fluorescence spectra of the silica particles fall in the visible range, an appealing feature for imaging applications. Moreover, the particles showed multi-exponential decays with fluorescent lifetimes up to 9.0 ns that can be easily discriminated from intrinsic biological fluorescence with fluorescent lifetimes below 3-4 ns. Fluorescent particles encapsulating CLZ exhibit much shorter average fluorescence lifetimes that can be distinguished from the unloaded particle average fluorescence lifetimes offering thus a promising tool for theranostic purposes (see Figure 4).
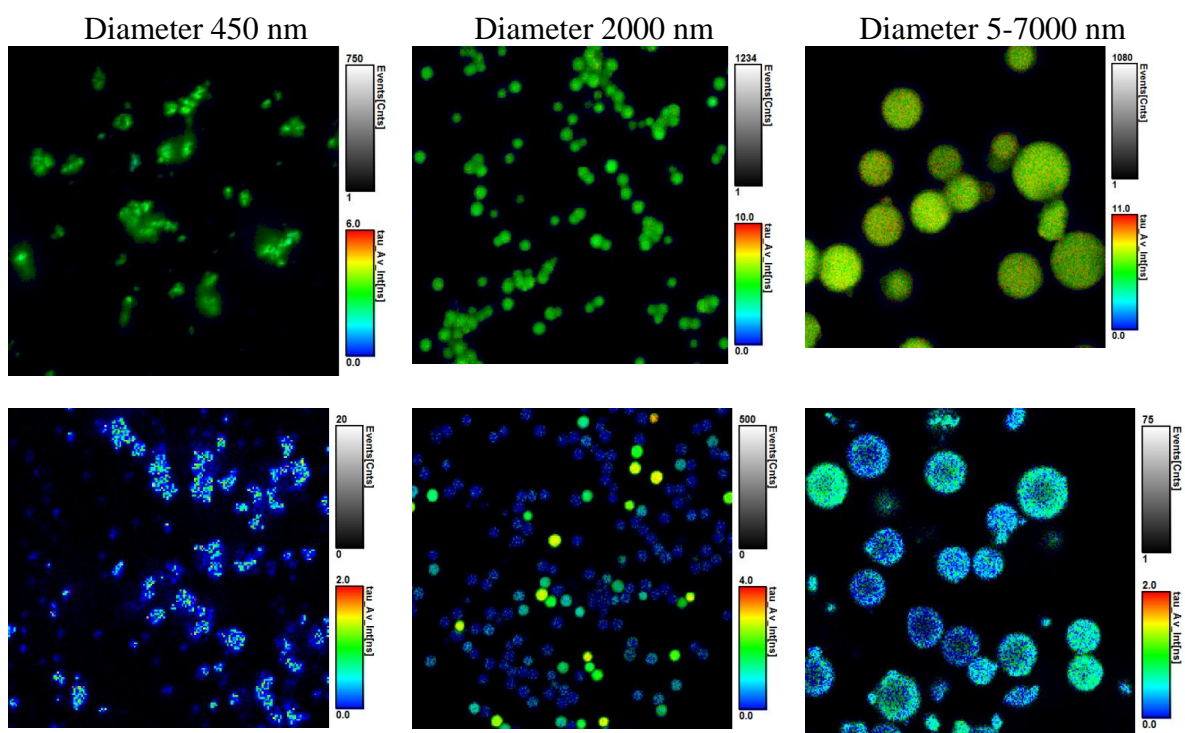
Figure 4: FLIM images: (top) unloaded fluorescent MSPs , emitted photons collected in the 500-550 nm range exciting at 405 nm; CLZ loaded MSPs, emitted photons collected in the 565-605 nm range exciting at 485 nm; (bottom) ; color refers to average lifetime according to the scale bar on the right.

During a secondment near the Swedish project partners, Nanologica and the Gothenburg University, fluorescent silica particles loading CLZ were further explored. At Nanologica, work focused on the loading of CLZ in differently sized mesoporous silica particles and its characterisation. These CLZ/Silica particles were further loaded in chitosan film and microcapsules for drug release studies using a cellulose dialysis membrane (MW cut off 1600 Da) mounted in a Franz diffusion cell but did not give satisfactory results.

At the Gothenburg University, a study was carried out on the penetration of differently sized silica particles in human skin monitored by means of two photon fluorescence microscopy. It was found that all particles adhere with the corneocytes of stratum corneum and the smallest particles can penetrate in strateum corneum furrows whilst the larger particles resided more superficially on the skin surface.

In conclusion my PhD research activity has been successful in achieving new carrier systems based on nanomaterials with the potential of driving innovation in the field of known drug delivery.

Chapter 1

Introduction

1.1 Nanotechnology for biomedical applications

Nanotechnology has gained importance in several fields and has become a very popular research area dealing with sensoring, environmental remediation, energy conversion and storage, semiconductors, biomedical applications, biomimetics, tissue regeneration, etc. Nanomedicine refers to the nanotechnology area addressing medical applications based on the use of nanosized materials. The field of nanomedicine has assumed a multifaceted aspect as it is addressing various issues like the delivery of conventional drugs by means of nanosize materials, development of new nanosize drugs, diagnostics by means of new nanomaterials with sensing, probing and labeling potential, and tissue regeneration with innovative nanomaterials in the field of regenerative medicine.[1] Generally, the field of drug development approaches nanotechnology when drugs suffer from drawbacks like (i) severe side effects due to the lack in target specificity or the low drug efficacy forcing to increment drug doses, (ii) low water solubility and/or crystallization during storage or *in vivo*, (iii) unfavorable pharmacodynamics and pharmacokinetics or (iv) problems related with drug resistance arising more and more and compromising approved conventional treatments. To overcome these drawbacks nanotechnology dealing with drug delivery offers a wide range of tools that allow to obtain a lot of advantages such as better drug stability and solubility, targeted delivery, improved bioavailability, reduced dosage and optimised dosage timing, reduced toxicity, improved permeability in both skin and intestinal tissues.[2] Moreover, nanotechnology is also broadening the palette of therapeutic strategies as it can help to implement in a smart way (i) co-administration of more drugs, (ii) synergic combination therapy including less routine approaches like photodynamic therapy and photothermal therapy, (iii) the blend of therapeutics with diagnostics, and so on.[3, 4] The nanotechnological toolkit relies on a careful nanomaterial design process keeping in mind the final biomedical application. Various components are brought together in a rationale way in order to obtain the new material with the desired functionalities. *Ad hoc* designed functional nanomaterials with biomedical potential often adopt a hybrid character gathering molecular and supramolecular components, inorganic substances in combination with organic and even biological components, polymeric materials mixed with inorganic building blocks etc.[5] This boosting field of research has resulted in some

concrete applications of nanotechnology-based drug delivery systems nowadays available on the market. One of the first examples of FDA approved nanoformulations for therapeutic applications is Doxil®. Doxil is a PEGylated liposome formulation approved by US-FDA in 1995 for the target-specific delivery of Doxorubicin in tumoral tissue displaying reduced drug cardiotoxicity compared to the pure drug.[6] Other nanoformulations of anthracyclines followed like liposomal daunorubicin (DaunoXome®), liposomal doxorubicin (D-99, Myocet™), and pegylated liposomal doxorubicin (Caelyx®), all delivery systems exploiting the enhanced permeation and retention (EPR) effect.[6, 7] The latter effect is due to the small dimension (<300 nm) of the nanoformulations enabling the drug to accumulate in the tumor tissues by crossing passively the fenestrations in the diseased vasculature of the tumoral tissue, called passive targeting, thus avoiding or reducing penetration in normal tissue with a consequent lower cytotoxic effect. Another well known FDA approved nanoformulation concerns a taxane, called paclitaxel. Abraxane® is a novel solvent-free formulation in which paclitaxel is complexed only with the serum albumin protein to form stable particles with a size of 130 nm. It is approved for the treatment of breast cancer with improved efficacy compared with the conventional paclitaxel formulation and exploits the EPR effect of the nanoparticle.[6] In spite of the huge efforts in the field of nanotechnology for known drug delivery very few innovative solutions have been proposed for the delivery of antibiotics. Indeed there is an urgent need for new therapeutic strategies to face one of the main problems encountered nowadays in the treatment of infectious diseases: the development and diffusion of antibiotic resistant bacterial strains.

1.2 Bacterial drug resistance

The era of antibiotics was launched by the penicillin discovery of Alexander Fleming in 1928. It was a life-saving drug for many decades but with time resistance has emerged for penicillin. A new class of beta-lactam antibiotics has been synthesised to overcome the problem of bacterial resistance developed against penicillin. Nevertheless, during 60' the first cases of multidrug resistant (MDR) *Staphylococcus Aureus* (MRSA) were reported in UK and USA. Infections due to drug resistant strains of gram positive bacteria like *S. Aureus, Enterococcus* and the most common respiratory pathogens, *Streptococcus Pneumoniae* and *Mycobacterium Tuberculosis* have nowadays become endemic all across the world. MDR strains of Gram negative bacteria like *Klebsiella Pneumoniae*, *Pseudomonas Aeruginosa* and *Acinetobacter* are also emerging and diffusing.[8, 9] WHO has

warned about an antibiotics resistance crisis as it will become even more critical in the future. The problem is clearly illustrated by data on Tuberculosis, one of the leading infectious diseases. Around 9.6 million people suffered from this disease and among 1.5 million died in 2014 according to WHO data. WHO reported that 480 000 cases were associated with multidrug resistant tuberculosis. This crisis is due to overuse and misuse for a long time of several antibiotics and the lack of interest for several decades in developing new antibiotics by pharmaceutical companies, because of the low profit compared with new drug development against metabolic diseases, a task requiring almost two decades due to stringent regulatory rules.[9] Bacterial drug resistance has occurred through the following process:

Reduced permeability: Hydrophilic antibiotics diffuse through outer membrane by means of porin channels. Downregulation of porins or replacement with alternative channels causes a reduced permeability of the membrane and results in a limited antibiotic entry.

Increased efflux: Bacterial efflux pumps are proteins actively transporting antibiotics out of the cell. They can be either substrate specific or active on a wide range of dissimilar antibiotics.

Changes in antibiotic targets by mutation: Most antibiotics specifically bind to their target with high affinity, thus inhibiting the normal activity of the target. Changes to the target structure due to genetic mutations can prevent efficient antibiotic binding, while maintaining the target normal activity, and thus confer resistance.

Modification (and protection) of targets: Protection by modification of the target can also be a cause of antibiotic resistance that does not require a mutational change in the genes encoding the target molecules. Modification of the target by addition of a chemical group, such as methylation, can prevent antibiotic binding without altering the target protein primary sequence.

Direct modification of antibiotics: bacteria can directly inactivate antibiotics by (i) hydrolysis involving cleavage of an amide or ester bond by enzymes, like the well-known penicillinase, or *(ii)* by transfer of a chemical group catalysed by transferase enzymes which chemically substitute the antibiotics with phosphoryl, adenylyl or acetyl group hampering the binding of antibiotics with target sites. [10]

1.3 Nanocarriers for antibiotics delivery

To overcome some MDR problems arising in the treatment of bacterial infections nanotechnology can help to find innovative solutions without the need of developing new drugs, a time consuming and expensive process. Indeed the field is mature to offer alternatives for the delivery of known antibiotics in a more fashioned way that allows circumventing the resistance problem. Encapsulation of antibiotics in nanocarrier systems can improve the fate of the drug inside the body and result in improved pharmacodynamics and pharmacokinetics by means of targeted delivery, different cellular internalisation mechanisms, controlled release, immune system escape and longer circulation times.[11] Several types of nanocarriers can be envisaged for the purpose of encapsulation and we cite some of the most popular actually under exploration as antibiotic carrier.

1.3.1 Polymeric nanocarriers

Polymeric nanoparticles can be obtained from natural or synthetic polymers. They are colloidal systems self assembling in particles with a size ranging from 10 to 100 nm. Due to FDA regulation, preference has been given to biodegradable and biocompatible polymers which do not solicit immunoreactions and whose metabolism is well known in the human body and not producing any harmful metabolites or toxic substances. Polymeric nanoparticles are prepared by various methods such as solvent evaporation, sonication, and emulsion.[12] Several biodegradable polymers are used for the preparation of nanoparticle as they offer various advantages. The most widely used biodegradable polymers are polyesters like polylactic and polyglycolic acid polymers or copolymers, polycaprolactone, polyhydroxybutyrate, chitosan, polyethylene oxide, poly(alkyl cynoacrylates).[13,14]

Drugs can be either entrapped in the NP and / or be adsorbed on the NP surface or shell in the case of coated systems. Release from polymeric NPs and subsequent polymer biodegradation are important for developing the successful formulations. The drug release modes and rates in polymeric NPs depend on: (i) desorption of the surface-bound/adsorbed drug; (ii) diffusion through the NP matrix of entrapped drugs toward the exterior; (iii) diffusion, in case of polymeric coated NPs, through the polymer wall; (iv) NP matrix degradation determined by polymer composition; and (v) a combined degradation/diffusion process.[15] Polymeric NPs can offer several advantages for the delivery of antibiotics as they can offer drug protection, escape the immune system, avoid

clearance, and /or enter the target cell by different mechanism compared to the drug alone (Figure 1.1).

A more recent category of *smart* NP drug delivery systems is represented by environmental stimuli-responsive polymeric nanoparticles. Physical, biochemical and physiological stimuli trigger the polymeric container to release the drug.[16] Stimuli-responsive nanosize carriers have been classified as (1) pH responsive polymeric nanoparticles, (2) enzyme responsive polymeric nanoparticles, (3) oxidiation/reduction sensitive polymeric nanoparticles, (4) thermoresponsive polymeric nanoparticles releasing the drug with a temperature change, (5) light activated polymeric nanoparticles starting release following irradiation, (6) magnetice field responsive nanoparticles.[16, 17]

As an example we cite ampicillin encapsulated polyhexylcyanoacrylate nanoparticles that were able to increase 120-fold the efficacy of the antibiotic in experimental murine salmonellosis.[18]
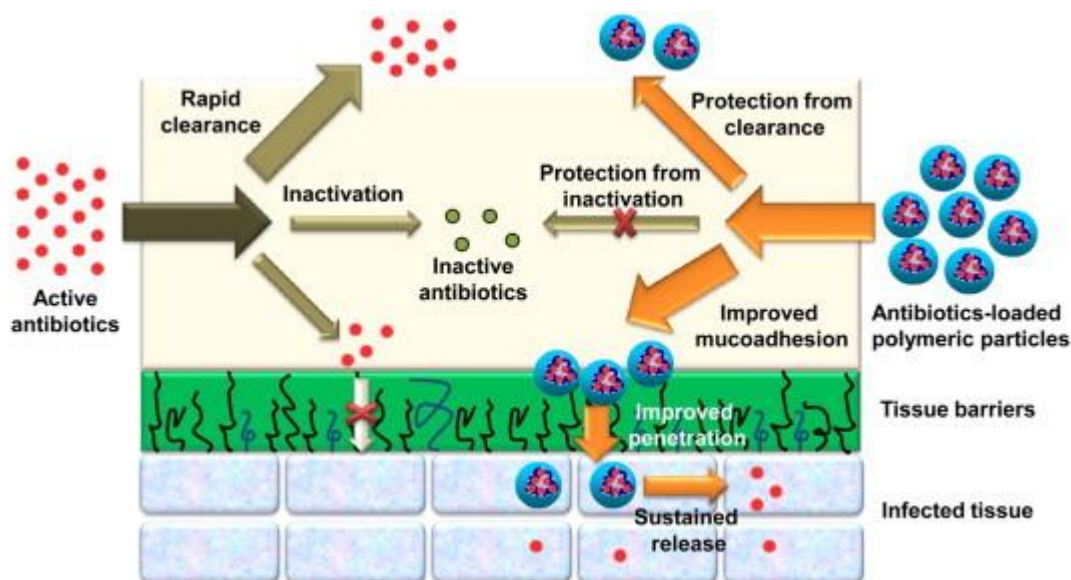
Figure1.1 Polymeric Nanoparticle approach to avoid MDR problems[19]

1.3.2 *Liposomes and vesicles*

The liposome is a tiny vesicle with a bilayered membrane composed of amphiphilic phospholipids with an entrapped aqueous core. Due to the amphiphilic nature of the liposome, it not only encapsulates the hydrophobic drug in the lipophilic exterior membrane but also encapsulates hydrophilic drugs in the aqueous core (Figure 1.2). Nowadays, liposomes are composed of natural and/or synthetic phospholipids, such as phosphatidylcholine, phosphatidylethanolamine, phosphatidylserine, and phosphatidylglycerol. In order to improve the physical stability of liposomes, cholesterol

has been added as an additional component of the lipid bilayers, as it can enhance membrane rigidity and *in vitro* and *in vivo* stability. Hydroxyl groups present at the outer surface can form hydrogen bonding with the aqueous surrounding which tends to improve the solubility of liposome drug systems. Liposomes are often surface modified, for example by PEGylation, and called "stealth liposomes" which are not easily recognised by the reticuloendothelial system and display a longer circulation time.
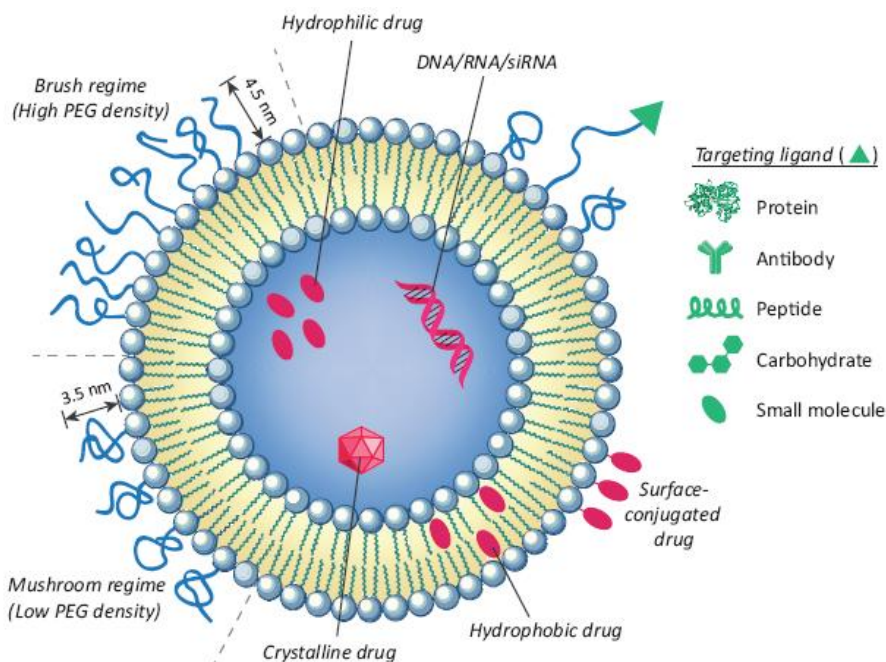
Figure 1.2 Liposome structure and functionalisation[20]

The most common way to produce liposomes is solvent evaporation from the lipid to form the thin film which is further dispersed in an aqueous system with slight agitation. Other methods of preparation are sonication (probe/ultrasound), injection-antisolvent method and dialysis of lipid dispersion.[21, 22]

Liposomes however show some drawbacks such as poor colloidal and chemical stability, rapid clearance from the blood circulation, high permeability of their membranes causing leakage of the entrapped drugs, high cost due to expensive phospholipids, etc. In order to overcome these problems, new generations of lipid-based vesicles have been developed. Based on their morphology and size, vesicles are defined as small (up to 100 nm) or large (100 nm to few μm) unilamellar vesicles (SUV, LUV) or multilamellar vesicles (MLV).[22]

As an example we report Amikacin encapsulated in neutral liposomes and given at 50 mg/kg, twice-weekly for 3 weeks to mice infected with *M. avium* being more active than the free drug.[18]

1.3.3 Cyclodextrin-based nanocarriers

Cyclodextrins (CyD) are cyclic oligosaccharides obtained from the enzymatic hydrolysis of starch. Three basic types of CyDs are widely used in the pharmaceutical field. These are αCyD, βCyD and γCyD with 6, 7, and 8 glucopyranose units, respectively, joined by α-1,4-glucosidic linkages (Figure 1.3). CyD has a unique bucket-like structure with a hydrophilic outer ring which is due to hydroxyl groups present at the outer surface and a hydrophobic interior inside the bucket due to alkyl functionality.[23]
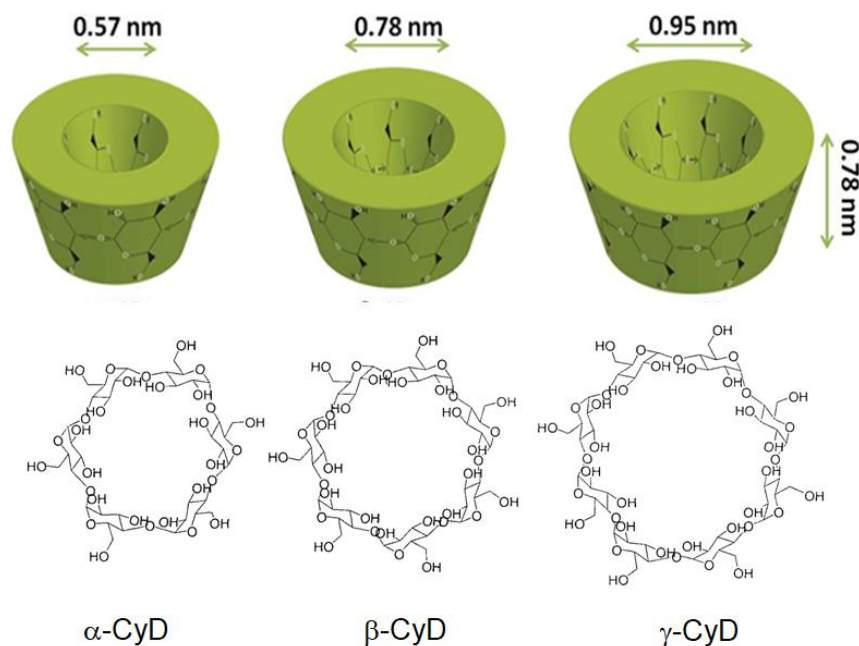
Figure 1.3 Cartoon and chemical structures of α, β and γCyD[24]

CyD has the unique ability of molecular encapsulation by means of non-covalent interactions. Several molecules were investigated for encapsulation by non-covalent binding in CyDs in solid phase or aqueous solution. Hydrophilic drugs interact with the hydrophilic exterior of CyD resulting in improved water solubility. Importantly, hydrophobic drugs interact with the hydrophobic cavity of CyD which improves also the solubility of the hydrophobic drug in the aqueous system. Drug encapsulation in CyD enhancing the solubility can potentially increase their oral bioavailability.[25,26]

Along with natural CyDs, various derivatives are examined as solubility enhancer for drug delivery purposes like Hydroxypropyl-β and γCyD, methyl-βCyD and sulfobutylether βCyD. Recently, CyD polymeric nanoparticles have become very popular and easily accessible and they have been investigated for drug delivery. Epichlorohydrin, an efficient crosslinking agent, causes the polymerisation of natural CyDs in basic aqueous environment and forms the CyD polymer with high CyD amounts reaching 70%

w/w. These polymers have the ability to form self assembled nanoparticles and improve the solubility of encapsulated drugs to a higher extent compared to monomeric CyD.[27, 28]

As an example we cite a hydroxyapatite (HA) functionalised hydroxypropyl-β-cyclodextrin polymer loaded with Ciprofloxacin and vancomycin showing a prolonged bacteriostatic activity against Staphylococcus aureus for the prevention of bone infection during bone-graft surgery.[29]

1.3.4 Metal organic frameworks

Metal organic frameworks (MOFs) are an emerging new class of materials gaining tremendous interest in drug delivery. The porous hybrid structure is made up of metal ions/clusters lined or bridged by organic linkers (Figure 1.4). Depending on the metal ion and the organic bridging linker they have versatile properties like high surface area, high porosity, well ordered structure which can allow high drug encapsulation efficiency.
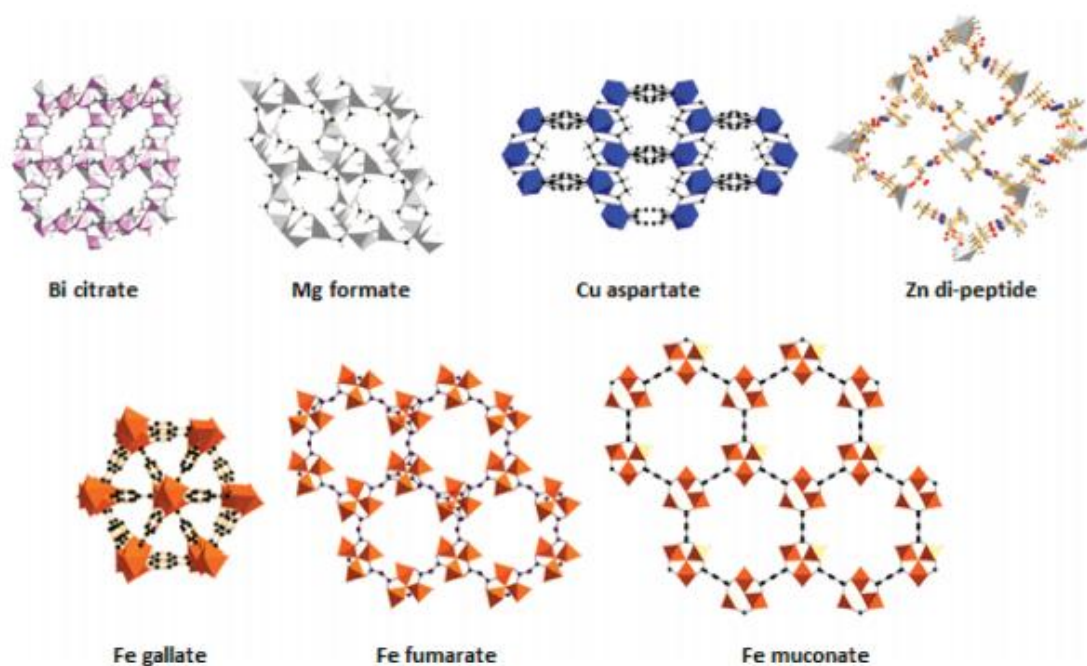
Figure 1.4 MOF examples of various metals unit with different linker systems[30]

MOFs are synthesised by tailoring branched and linear organic ligands to tune the surface area as well as particle dimension and pore size.[30,31] Typical ligands used for the synthesis of MOFs with application in drug delivery are organic ligands with carboxylate, phosphonate, or sulfonate groups. Choosing adequately the components one can obtain multifunctional MOFs for example magnetic ones based on Fe with potential in magnetic resonance imaging and luminescent MOFs interesting for optical imaging. So far no MOF is available on the market as drug delivery system. Fe(III)-carboxylate nanoscale MOFs

with the MIL-101 (Figure 1.5) structure were used for encapsulation of imaging agent (a BODIPY dye) and an ethoxysuccinato-cisplatin anticancer prodrug particles as a potential MOF-based carrier for optical imaging and anticancer therapy.[32]
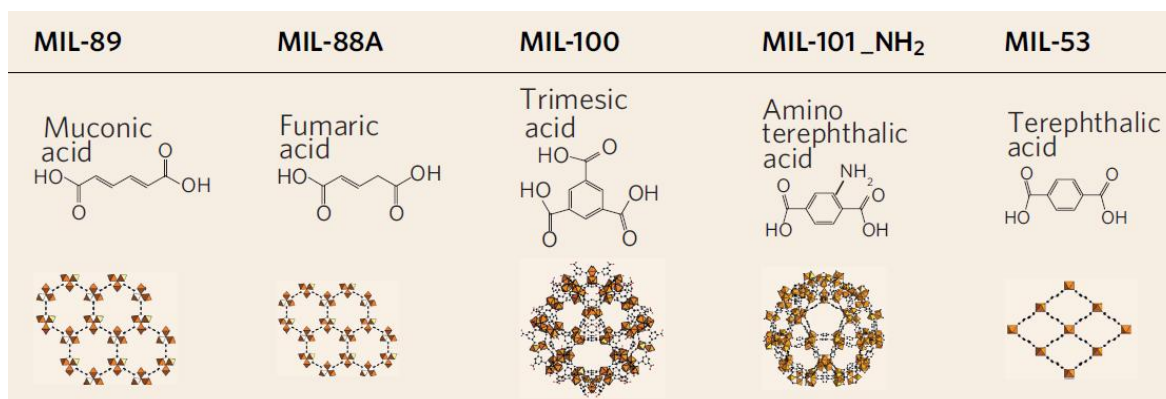
Figure 1.5 Structure of Fe(III)trimer based MIL-MOFs with different linker systems[30]

Tetrahedral phosphonate ligand, 1,3,5,7- tetrakis(4-phosphonatophenyl)adamantane (H8L), was used for direct the formation of an open framework upon metal complexation having a microporous phosphonate network containing unprecedented metal clusters.[31,33]

1.3.5   Silica particles

In the last two decades, mesoporous silica particles based on silicon dioxide have gained importance in the pharmaceutical field due to their versatile and appealing properties such as the porous structure within the solid framework, the large surface volume and the ease of modification to attach ligands for targeted drug delivery. Mesoporous silica particles (MSP) are prepared by template-based and sol-gel methods involving the replication of a surfactant liquid crystal structure, polymerisation of metal oxide precursor and removal of organic surfactant through the calcination process thus obtaining a porous structure.[34] Figure 1.6 represents the synthesis of nonporous/mesoporous silica hollow spheres by micelle and emulsion dual templating method of anionic surfactants and oil as a template. 3-aminopropyl-triethoxysilane (APES) and tetraethyl orthosilicate (TEOS) have been used as co-structure directing agent (CSDA) and silica source. The lamellar structured (a) and mesostructured (b) silica hollow spheres were formed without and with adding an alcohol co-solvent, respectively.[34] Mesoporous silica particles have often high drug loading capacity and exhibit low toxicity making them often the carrier of choice for controlled and targeted drug delivery.
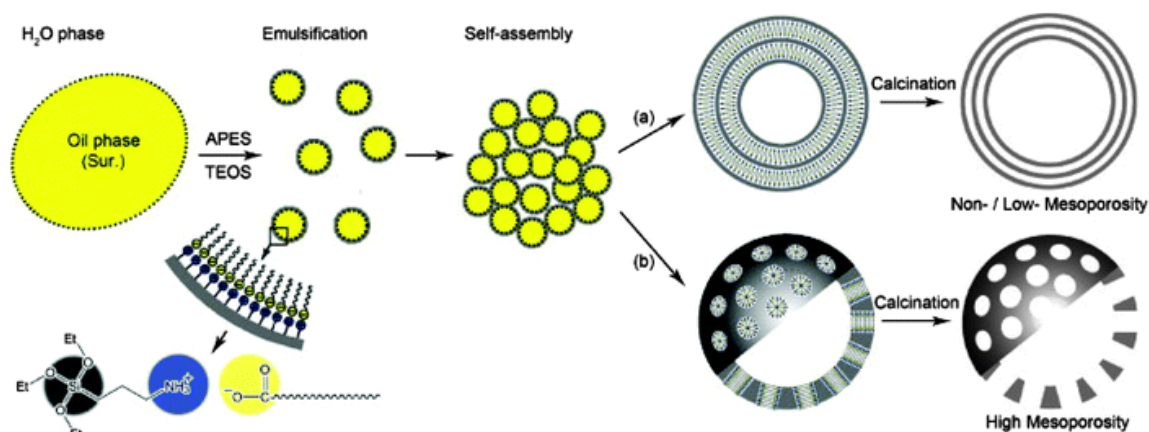
Figure 1.6 Silica particle and its schematic synthesis.[34]

Mesoporous silica particles which are stimuli responsive are currently under research. Several pH, redox, enzyme, and light activated MSP carrier systems have been developed to improve the therapeutic value of drugs and obtain multifunctional drug delivery systems.[35,36] For example, biodegradable silica xerogel loaded with gentamicin are more effective in treating murine salmonellosis infection in mice than the free gentamicin.[37]

1.3.6 *Hybrid nanoparticles*

Hybrid nanoparticles are made up of different components like metal oxides, organic, biological and inorganic components, polymers, etc. providing a more complex system that can assume a variety of structures and functions. For a comprehensive review we refer to Chemical Society Reviews issue 40 of 2011 giving a wide panorama of the existing hybrid materials for applications in various fields including nanomedicine. Several molecular approaches have been explored to design hybrid nanoparticle.[38-40] This is illustrated by some examples of hybrid systems used for antibiotic delivery. Islan et al. obtained inhalable hybrid carriers prepared by co-precipitation of CaCO3 in the presence of alginate and treated the resulting microparticles with alginate lyase to modify porosity and drug loading ability. The hybrid microparticles were loaded with a DNase mucolytic agent and levofloxacin, a wide-spectrum antibiotic. *In vivo* studies were performed by pulmonary administration of microparticles to healthy mice via nebulisation and dry powder inhalation, followed by drug quantification in lung tissue. The loaded microparticles delivered the antibiotic 3 times more efficiently compared to free drug.[41]

In another study Gaurav et al. used a combination of silver nanoparticles with well documented antifungal activity and a standard antifungal molecule Clotrimazole. Clotrimazole was included into a βCyD to render it water soluble; subsequently bovine

serum albumin coated silver nanoparticles were linked to drug loaded βCyD moiety using 1-ethyl-3-(3-dimethylaminopropyl) carbodiimide/N-hydroxysulfosuccinimide chemistry. This hybrid system was evaluated for its fungicidal activity on normal and clotrimazole resistant Candida cells. Improved IC50 values and synergic effects were reported for the hybrid clotrimazole loaded system.[42]

Zhang et al. reported a bioadhesive nanoparticle−hydrogel hybrid to enhance localised antimicrobial drug delivery. Cyprofloxacin was loaded in polymeric PLGA nanoparticles and then embedded into a 3D hydrogel network, based on acrylamide, poly(ethylene glycol), dimethacrylate, used as cross-linker, and poly(vinylalcohol), that confers adhesion to biological surfaces. The bioadhesive NP-gel showed superior adhesion and antibiotic retention under high shear stress on a bacterial film, a mammalian cell monolayer, and mouse skin tissue. The NP-gel inhibited the formation of an *E. coli* bacterial film. When applied on mouse skin tissue for 7 consecutive days, the NP-gel did not generate observable skin reaction, implying its potential as a safe local delivery platform.[43]

As last example, we cite a Ag polymeric hybrid nanocomposite investigated for the delivery of amoxicillin and further studied for cytotoxicity, free-radical scavenging, and antibacterial activities.[44]

1.4 Scope of the thesis

The main objective of the thesis is the exploration of CyD- and silica-based nanomaterials as carrier systems to improve the efficacy of some selected antibiotics, especially against bacterial MDR strains. In particular we have studied ethionamide, ETH, and clofazimine, CLZ, due to their very interesting activity against several bacteria. There clinical application is however strongly limited as they both suffer from administration limits and severe side effects.

1.4.1 Ethionamide

Scheme 1.1 Ethionamide
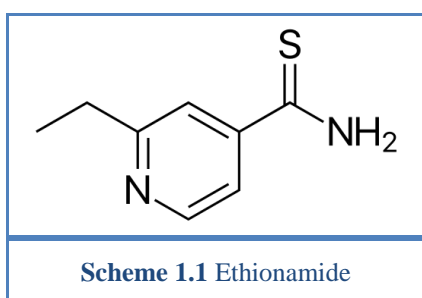
Ethionamide (ETH, scheme 1.1) is a thioamide that is very sparingly soluble in water, obtained from isonicotinic acid. Although ETH has a broad activity spectrum against Mycobacterium strains including *M. tuberculosis, M. bovis, M. smegmatis* and *M. lapre* and good efficacy in the treatment of tuberculosis, it remains

a second line drug due to its high dose related severe side effects including nausea, vomiting, diarrhea, and nervous system toxicity as well as hepatotoxicity. For these reasons WHO classified ETH as a reserve drug for the treatment of infections due to resistant strains of *M. tuberculosis*.[45] ETH is easily absorbed form the gastrointestinal tract and has a rapid distribution in body and fluids. It attains a significantly higher concentration in lungs, tuberculosis lesions and cerebrospinal fluid. As said above, side effects are mainly dose related and decreasing the dose without affecting the efficacy of the treatment should thus substantially increase patient compliance. Moreover, also low solubility and tendency of the drug to crystallize hamper its administration alternative routes for the delivery of ETH have been explored.[45] Few examples are present in literature focusing on nanomaterials for ETH delivery.

N. Vale et al. have evaluated porous silicon microparticles to improve the pharmacokinetics of ETH. They observed reduced toxicity when ETH is loaded within porous silicon particles and it was suggested as a potential formulation for multidrug resistant tuberculosis.[46] L. Garcia-Contreras et al. studied the pulmonary delivery of ETH in spray-dried particles. It was administered to guinea pigs by oral, intravenous and pulmonary route. Pharmacokinetics of drug was compared for the different routes of administration and it was found that the ETH bioavailability is 85% higher after pulmonary administration compared with 17% oral bioavailability. This pulmonary delivery of spray-dried ETH particles may be used in the future treatment of tuberculosis.[47]

1.4.2 *Clofazimine*

Clofazimine (CLZ, scheme 1.2) also known as B633 is a phenazine derivative. It is a red brown fine powder. It is available under the trade name "lamprene" and launched by Novartis as anti leprosy drug in 1969. It is the most recommended drug in combination therapy for leprosy treatment. It is also used in the treatment of chronic skin ulcer caused by *M. ulcercan*. It is known that CLZ affects a spectrum of Gram-positive but not Gram-negative bacteria. Gram-positive species reported sensitive to CLZ other than mycobacteria include Staphylococci, Streptococci, Enterococci, and Listeria. In the last few decades with the appearance of MDR resistant bacterial strains, CLZ has been studied for the treatment of drug resistant and sensitive strains of *M. tuberculosis*.[48]
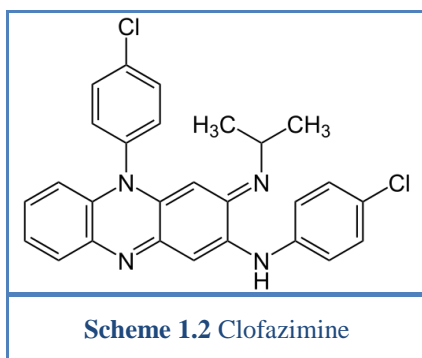
CLZ is practically insoluble in aqueous media making it unsuitable for intravenous use. Orally administered CLZ is not completely absorbed from gastrointestinal tract. As CLZ is highly lipophilic (LogP 7.5), it tends to be deposited predominantly in fat tissues and in cells of the reticuloendothelial system. CLZ has pKa of 8.35 thus it deposits mainly as cation in cell membranes at physiological pH. CLZ has a long half life of 79 days after repeated oral administration. CLZ administration is suffering from severe side effects like nausea, vomiting, diarrhea, skin discoloration.[49] Absorbed drug undergoes rapid metabolism in the liver. CLZ is metabolised in the liver into three main metabolites, hydrolytic de-halogenated, hydrolytic deaminated and hydroxylated glucuronide products. The pharmacological activity of these metabolites is not yet clear. Indeed, the exact mechanism of action of CLZ is not yet known but the bacteria outer membrane seems to be the primary target and activity is likely related with redox cycling processes and inhibition of K^+ transport. CLZ is believed to be a membrane-destabilising agent, dismantling membrane architecture both directly and via lysophospholipids, with consequent dysfunction of vulnerable K+ transporters. Secondly, CLZ possesses a high redox potential, -0.17 V at pH 7, is easily reduced in the presence of NADH, and re-oxidised in a process producing ROS like the hydrogen peroxide free radical. This may interact with the electron transport system and interfere with the bacterial respiratory chain.[48]

Some examples are now present in literature focusing on nanomaterials for CLZ delivery in order to overcome some administration drawbacks. Rahul Kumar Verma et all used CLZ leucine mixed inhalable dry powder microparticles and native CLZ against *M. tuberculosis* in human monocyte-derived macrophage cultures and in infected mice. Both formulations resulted in 99% killing of bacteria at 2.5 µg/ml *in vitro*. In infected mice, 480 µg and 720 µg CLZ loaded dry powder microparticles inhaled twice per week over 4 weeks reduced numbers of CFU in the lung by as much as $\log_{10} 2.6$; 500 µg oral CLZ achieved only a $\log_{10} 0.7$ reduction.[50]

Sabrina Valetti et all have studied encapsulation of CLZ in nanoporous silica particles to overcome mycobacterial drug resistance by improving the drug solubility in gastric fluid, the drug intestinal permeability and the stability on storage for more than 6 months in amorphous form.[51]

13

1.4.3 Thesis outline

In the following chapters we will present the results we obtained concerning:

1. Loading and interaction of ETH with natural βCyD, βCyD based polymer and Fluorescein tagged βCyD polymer

2. Co-encapsulation of ETH and booster molecules within βCyD based polymer

3. Loading and interaction of CLZ with sulfobutylether (SBE)-βCyD, SBE-βCyD polymer as well as their rhodamine tagged labeled analogues; the CLZ loaded carrier activity against gram positive bacteria like *S. aureus* and *S. epidermidis*.

4. Loading and interaction of CLZ with fluorescent mesoporous silica particles and the time-resolved confocal fluorescence imaging of the drug presence in the particles

1.5 References

1.   A. P. Ramos, M. A. E. Cruz, C. B. Tovani and P. Ciancaglini, *Biophys. Rev.*, **2017**, 9, 79-89.
2.   M. Zhu, G. Nie, H. Meng, T. Xia, A. Nel and Y. Zhao, *Acc. Chem. Res.*, **2012**, 46, 622-631.
3.   J. E. Lee, N. Lee, T. Kim, J. Kim and T. Hyeon, *Acc. Chem. Res.*, **2011**, 44, 893-902.
4.   L. Cheng, C. Wang, L. Feng, K. Yang and Z. Liu, *Chem. Rev*, **2014**, 114, 10869-10939.
5.   K. Raemdonck, K. Braeckmans, J. Demeester and S. C. De Smedt, *Chem. Soc. Rev.*, **2014**, 43, 444-472.
6.   R. Wang, P. S. Billone and W. M. Mullett, *J. Nanomater.*, **2013**, 2013, 1.
7.   Y. Nakamura, A. Mochida, P. L. Choyke and H. Kobayashi, *Bioconjugate Chem.*, **2016**, 27, 2225-2238.
8.   C. L. Ventola, *Pharm. Ther.*, **2015**, 40, 344.
9.   R. J. Fair and Y. Tor, *Perspect. Medicin. Chem.*, **2014**, 6, 25.
10.   J. M. Blair, M. A. Webber, A. J. Baylay, D. O. Ogbolu and L. J. Piddock, *Nat. Rev. Microbiol.*, **2015**, 13, 42-51.
11.   N. Abed and P. Couvreur, *Int. J. Antimicrob. Agents*, **2014**, 43, 485-496.
12.   K. S. Soppimath, T. M. Aminabhavi, A. R. Kulkarni and W. E. Rudzinski, *J. Control. Release*, **2001**, 70, 1-20.
13.   K. E. Uhrich, S. M. Cannizzaro, R. S. Langer and K. M. Shakesheff, *Chem. Rev.*, **1999**, 99, 3181-3198.
14.   V. Delplace and J. Nicolas, *Nat. Chem.*, **2015**, 7, 771-784.
15.   Y. Fu and W. J. Kao, *Expert Opin. Drug Deliv.*, **2010**, 7, 429-444.
16.   S. Mura, J. Nicolas and P. Couvreur, *Nat. Mater.*, **2013**, 12, 991-1003.
17.   M. A. C. Stuart, W. T. Huck, J. Genzer, M. Müller, C. Ober, M. Stamm, G. B. Sukhorukov, I. Szleifer, V. V. Tsukruk and M. Urban, *Nat. Mater.*, **2010**, 9, 101-113.

18. H. Pinto-Alphandary, A. Andremont and P. Couvreur, *Int. J. Antimicrob. Agents*, **2000**, 13, 155-168.
19. M.-H. Xiong, Y. Bao, X.-Z. Yang, Y.-H. Zhu and J. Wang, *Adv. Drug Del. Rev.*, **2014**, 78, 63-76.
20. M. Çağdaş, A. D. Sezer and S. Bucak, in *Application of Nanotechnology in Drug Delivery*, InTech, 2014.
21. T. M. Allen and P. R. Cullis, *Adv. Drug Del. Rev.*, **2013**, 65, 36-48.
22. N. Grimaldi, F. Andrade, N. Segovia, L. Ferrer-Tasies, S. Sala, J. Veciana and N. Ventosa, *Chem. Soc. Rev.*, **2016**, 45, 6520-6545.
23. T. Loftsson and M. E. Brewster, *J. Pharm. Sci.*, **1996**, 85, 1017-1025.
24. F. Kayaci and T. Uyar, *Food Chem.*, **2012**, 133, 641-649.
25. T. Loftsson, P. Jarho, M. Masson and T. Järvinen, *Expert Opin. Drug Deliv.*, **2005**, 2, 335-351.
26. K. Uekama and M. Otagiri, *Crit. Rev. Ther. Drug Carrier Syst.*, **1987**, 3, 1-40.
27. R. Gref, C. Amiel, K. Molinard, S. Daoud-Mahammed, B. Sébille, B. Gillet, J.-C. Beloeil, C. Ringard, V. Rosilio and J. Poupaert, *J. Control. Release*, **2006**, 111, 316-324.
28. E. Renard, A. Deratani, G. Volet and B. Sebille, *Eur. Polym. J.*, **1997**, 33, 49-57.
29. S. Leprêtre, F. Chai, J.-C. Hornez, G. Vermet, C. Neut, M. Descamps, H. F. Hildebrand and B. Martel, *Biomaterials*, **2009**, 30, 6086-6093.
30. P. Horcajada, R. Gref, T. Baati, P. K. Allan, G. Maurin, P. Couvreur, G. Férey, R. E. Morris and C. Serre, *Chem. Rev.*, **2011**, 112, 1232-1268.
31. P. Horcajada, T. Chalati, C. Serre, B. Gillet, C. Sebrie, T. Baati, J. F. Eubank, D. Heurtaux, P. Clayette and C. Kreuz, *Nat. Mater.*, **2010**, 9, 172-178.
32. K. M. Taylor-Pashow, J. D. Rocca, Z. Xie, S. Tran and W. Lin, *J. Am. Chem. Soc.*, **2009**, 131, 14261-14263.
33. J. M. Taylor, A. H. Mahmoudkhani and G. K. Shimizu, *Angew. Chem. Int. Ed.*, **2007**, 46, 795-798.
34. S.-H. Wu, C.-Y. Mou and H.-P. Lin, *Chem. Soc. Rev.*, **2013**, 42, 3862-3875.
35. C. Bharti, U. Nagaich, A. K. Pal and N. Gulati, *Int. J. Pharm. Investig.*, **2015**, 5, 124.
36. I. I. Slowing, J. L. Vivero-Escoto, C.-W. Wu and V. S.-Y. Lin, *Adv. Drug Del. Rev.*, **2008**, 60, 1278-1288.
37. M. N. Seleem, P. Munusamy, A. Ranjan, H. Alqublan, G. Pickrell and N. Sriranganathan, *Antimicrob. Agents Chemother.*, **2009**, 53, 4270-4274.
38. C. Sanchez, K. J. Shea and S. Kitagawa, *Chem. Soc. Rev.*, **2011**, 40, 471-472.
39. A. Mehdi, C. Reye and R. Corriu, *Chem. Soc. Rev.*, **2011**, 40, 563-574.
40. G. J. Soler-Illia and O. Azzaroni, *Chem. Soc. Rev.*, **2011**, 40, 1107-1150.
41. G. A. Islan, M. E. Ruiz, J. F. Morales, M. L. Sbaraglini, A. V. Enrique, G. Burton, A. Talevi, L. E. Bruno-Blanch and G. R. Castro, *J. Mater. Chem. B*, **2017**, 5, 3132-3144.
42. C. Gaurav, G. Nikhil, S. Deepti, S. Kalra, R. Goutam and G. K. Amit, *RSC Adv.*, **2015**, 5, 71190-71202.
43. Y. Zhang, J. Zhang, M. Chen, H. Gong, S. Thamphiwatana, L. Eckmann, W. Gao and L. Zhang, *ACS Appl. Mater. Interfaces*, **2016**, 8, 18367-18374.
44. T. Anirudhan and B. Deepa, *J. Appl. Polym. Sci.*, **2016**, 133.
45. T. Alliance, *Tuberculosis*, **2008**, 88, 106-108.
46. N. Vale, E. Mäkilä, J. Salonen, P. Gomes, J. Hirvonen and H. A. Santos, *Eur. J. Pharm. Biopharm.*, **2012**, 81, 314-323.

47. L. Garcia-Contreras, D. J. Padilla-Carlin, J. Sung, J. VerBerkmoes, P. Muttil, K. Elbert, C. Peloquin, D. Edwards and A. Hickey, *J. Pharm. Sci.*, **2017**, 106, 331-337.
48. C. M. O'Driscoll and O. I. Corrigan, *Analytical Profiles of Drug Substances and Excipients*, **1992**, 21, 75-108.
49. B. Lechartier and S. T. Cole, *Antimicrob. Agents Chemother.*, **2015**, 59, 4457-4463.
50. R. K. Verma, W. A. Germishuizen, M. P. Motheo, A. K. Agrawal, A. K. Singh, M. Mohan, P. Gupta, U. D. Gupta, M. Cholo and R. Anderson, *Antimicrob. Agents Chemother.*, **2013**, 57, 1050-1052.
51. S. Valetti, X. Xia, J. Costa-Gouveia, P. Brodin, M.-F. Bernet-Camard, M. Andersson and A. Feiler, *Nanomedicine*, **2017**, 12, 831-844.

Chapter 2

ETH inclusion complexes with CyD-based carriers

2.1 Introduction

This chapter deals with the inclusion of Ethionamide (ETH, scheme 2.1), an antitubercular drug, in CyD-based carriers. First line drugs like isoniazid and rifampicin for the treatment of tuberculosis are facing problems due to increasing microbial resistance.[1] ETH is a second line drug and has promising activity against multidrug resistant (MDR) strains of *M. tuberculosis*.[2,3,4] ETH is however suffering from poor water solubility and strong ability of forming crystals during storage both hampering its administration. Earlier research addressed the challenges associated with ETH administration by using nanocarrier systems made of poly(lactic acid) (PLA) or poly(lactic-co-glycolic acid) (PLGA).[5,6] However, preparation of the NPs required the use of toxic organic solvents such as methanol and dichloromethane and possible crystallization of the drug at the NP surfaces can compromise their positive effects.[5] In alternative we focused on CyDs for the delivery of ETH.
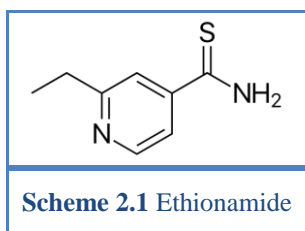
Scheme 2.1 Ethionamide

As mentioned in Chapter 1 Cyclodextrins (CyDs) are cyclic oligosaccharides composed of α-D-glucopyranose units coupled by α (1–4) linkages.[7] Different CyD-based nanocarriers have been developed as drug delivery system able of loading both hydrophobic and hydrophilic drug molecules promoted by non covalent interactions or labile covalent bonds.[8] The drug encapsulation by CyDs can inhibit the drug to adopt a self-assembled crystalline structure hampering the administration and *in vivo* application of the drug.[9] Recently, polymers made of CyDs have gained huge attention due to (i) their ease of preparation, (ii) better water solubility compared to monomeric CyDs, (iii) the presence of multiple CyD units in a confined space allowing a further improvement of the carrier solubilising potential compared to monomeric CyD, and, importantly, (iv) the contemporary loading of two or more drug molecules.[10] CyD polymers have been synthesised with different approaches such as crosslinking with epichlorohydrin in basic solution affording up to 70% w/w CyD content in the polymeric chain.[10] The reaction conditions are determining for the molecular weight of the polymer. Interestingly, epichlorohydrin crosslinked CyD polymers are able to form self-assembled nanoparticle in aqueous systems having a particle size of ca. 20 nm.[11] We investigated the possibility of

incorporating ETH in a epichlorohydrin crosslinked βCyD polymer with MW of 200 kDa using a green approach by reducing or even avoiding the use of organic solvents in preparation.

Additionally, we examined natural βCyD as model and a epichlorohydrin crosslinked βCyD polymer labeled with fluorescein (FITC-pβCyD, Scheme 2.2) promising for imaging tasks. ETH inclusion in βCyD, pβCyD and FITC-pβCyD was extensively investigated by means of optical spectroscopic techniques using circular dichroism (CD), UV vis absorption, and fluorescence measurements combined with HPLC based solubility phase diagrams. The βCyD epichlorohydrin crosslinked polymer organising in nanoparticle is able to load ETH in high amounts and to avoid ETH crystallization during particle preparation and storage.

2.2 Preparation of titration solutions

Titration solutions were prepared with different amounts of βCyD or pβCyD NPs in aqueous solutions ranging from 0.45-9 mg/ml and 5-20 mg/ml, respectively. A concentrated ETH solution in the mM range was prepared in methanol or ethanol. Afterwards, βCyD or pβCyD NPs aliquots were added to measured volumes of ETH solution and kept stirring for 1 h at room temperature under light protection. Organic solvent content in final mixture never exceeded 2%. The results obtained were compared with those of mixtures prepared dissolving solid ETH films, obtained upon evaporation of an organic solvent, with aqueous carrier solutions.

2.3 ETH interaction with βCyD
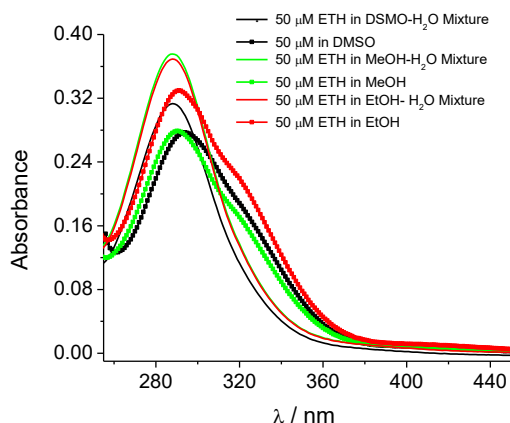
Figure 2.1 Absorption spectra of ETH in pure solvents and aqueous binary mixtures with less than 5% v/v organic solvents. d = 1.0 cm.

We studied the ETH interaction with βCyD by means of absorption and Circular dichroism (CD). ETH is a non-chiral molecule, so it is not endowed with an intrinsic CD signal. The molecule also lacks the ability to fluoresce in organic solvents like alcohols and DMSO or hydro-alcoholic mixtures used for the titration. The absorption spectrum of ETH dissolved in DMSO, MeOH or EtOH extends up to 425 nm and has a

characteristic peak at 288 nm as well as a shoulder at 320 nm (Figure 2.1). These spectra of ETH are different from the absorption spectra of ETH in binary aqueous mixtures having less than 5% organic solvent with the shoulder at 320 nm strongly diminishing in the aqueous mixtures.

Titration of ETH with βCyD up to 8×10^{-3} M causes a very small change in the absorption spectra characterised by an isosbestic point at 310 nm and a small hypochromic effect of the absorption at 288 nm and a more intense signal for the shoulder at 330 nm (Figure 2.2a) This might be due to the change in the local drug molecular environment which is more alcoholic inside the hydrophobic cavity of the βCyD.

Figure 2.2 (a) Absorption spectra of 1.25×10^{-4} M ETH solutions with increasing βCyD concentration (range 0.4-8 mM) in water, d = 1.0 cm. Note all samples contain 5% v/v MeOH; **(b)** Circular dichroism (CD) spectra of the same ETH solutions, d = 2.0 cm. **(c)** Calculated CD spectra (in molar ellipticity) of ETH, βCyD and the 1:1 complex obtained for a binding constant with $\log(K_{1:1}/M^{-1}) = 1.72 \pm 0.03$; **(d)** Equilibrium concentrations of ETH, βCyD and the 1:1 complex with increasing total βCyD concentration calculated with $\log(K_{1:1}/M^{-1}) = 1.72 \pm 0.03$.

Interestingly, an intense CD signal appeared with addition of βCyD to the drug solution. This signal is characterised by a negative signal at 280 nm in correspondence with the absorption maximum and a positive band at 320 nm with an intense shoulder at 380 nm (Figure 2.2b). These bands are likely due to $\pi,\pi*$ transitions of the pyridine and $n,\pi*$ transitions of the amine and thioamide chromophores.[12] The CD signal of both $\pi,\pi*$ and

n,$\pi*$ transitions in the presence of βCyD indicate that the optical asymmetry of the CyD environment and the conformational constraints in the diastereomeric complexes induce substantial rotational strength in the drug electronic transitions. The CD data were globally analysed with ReactLab[TM] Equilibria (Jplus Consulting Pty Ltd) for the determination of the equilibrium binding constant assuming a 1:1 complexation stoichiometry. Binding constant with $\log(K_{1:1}/M^{-1})$ value of 1.72 ± 0.03 was obtained. To the best of our knowledge no other value of the binding constant has been reported for ETH and βCyD. Figures 2.2c-d show the calculated CD spectrum of the 1:1 complex and the species equilibrium concentrations, respectively.

2.4 ETH interaction with the βCyD polymer

We performed a similar investigation for ETH and pβCyD nanoparticles (NPs). Figures 2.3a-b represent the absorption and CD spectra of 5×10^{-5} M ETH solution with varying amount of the pβCyD polymer. The addition of pβCyD caused similar changes to those of βCyD, *i.e.* small changes in the absorption spectra with the shoulder at 320 nm increasing with pβCyD concentration. CD spectra are also very similar to the ETH/βCyD spectra showing an intense signal upon mixing of the carrier and drug solution. This signal was characterised by a negative band at 280 nm and a positive band at 320 nm with an intense shoulder at 380 nm. We performed a global analysis with ReactLab[TM] Equilibria of the different CD spectra applying a simplified 1:1 complexation model of one ETH molecule with one βCyD unit. Therefore the pβCyD amount was expressed in βCyD units concentration. It enabled calculating the apparent equilibrium binding constant with a $\log(K_{1:1}/M^{-1})$ value of 2.00 ± 0.02 which is slightly higher than the one obtained for βCyD. The calculated CD spectrum (Figure 2.3c) of the ETH complex with βCyD in pβCyD NPs is similar in shape and intensity to that of calculated spectra of monomeric ETH/βCyD, but not identical. In particular the relative intensities of the three main bands at 275 nm, 315 and 375 nm vary among the two complexes. This suggests that the drug may experience different molecular environments in pβCyD complex compared to βCyD. In fact, drug molecules inside pβCyD NPs can probably locate both in the hydrophobic alcohol-like βCyD cavities and in other confined spaces inside the self-assembled crosslinked polymer.

To avoid the organic solvent in the final formulation ETH dried films were prepared upon organic solvent evaporation. This film was further dissolved with aqueous carrier solution to obtain ETH-carrier complex, not having the organic solvent in complex mixture. Figure

2.3e shows the CD spectra that are identical to those obtained in the presence of small amount of organic solvent.
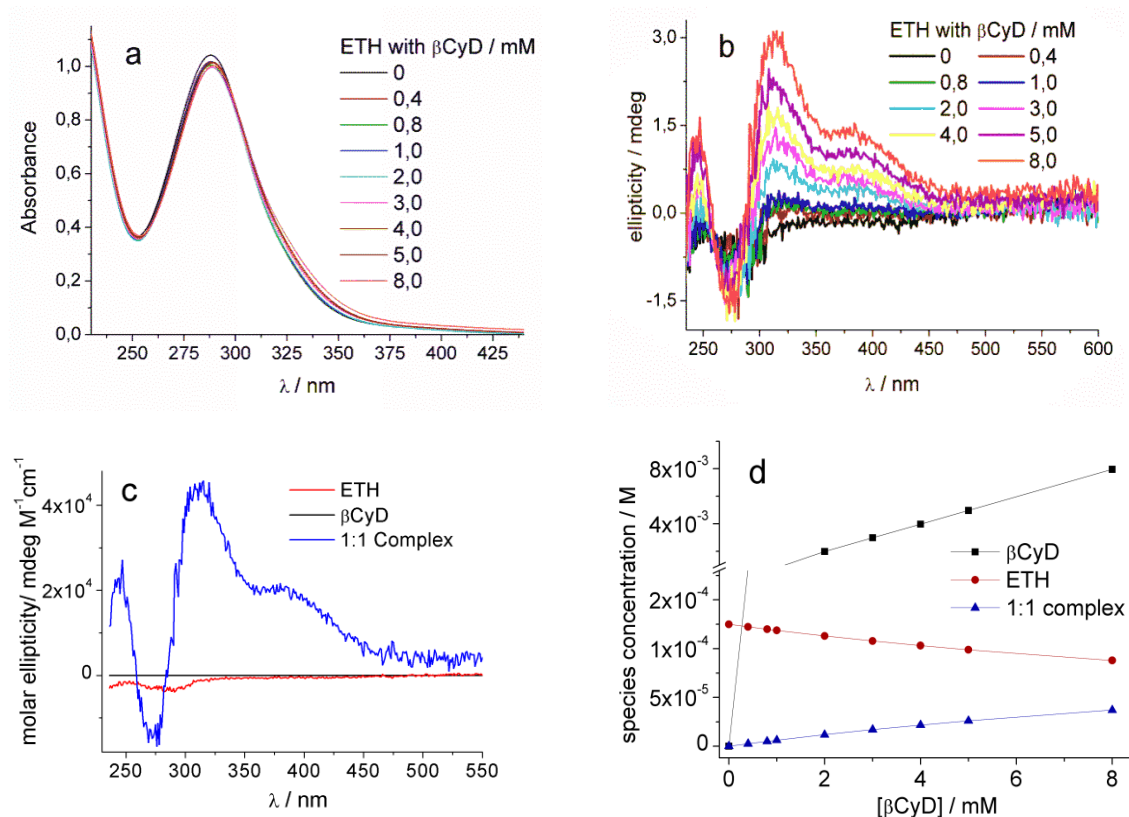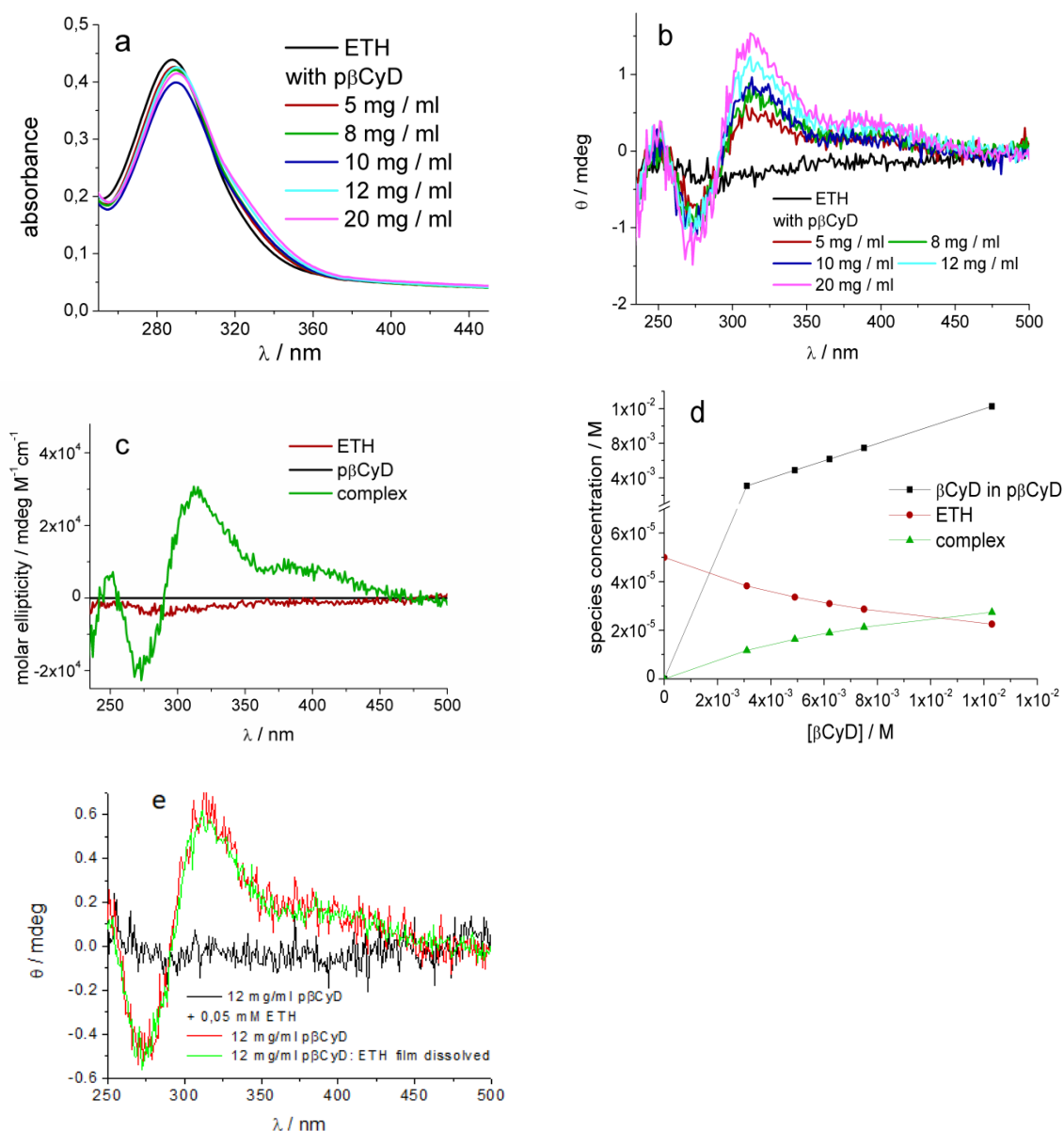

Figure 2.3 **(a)** Absorption spectra of 5×10^{-5} M ETH solutions with increasing pβCyD concentration (range 5-20 mg/ml) in water, d = 1.0 cm. Note all samples contain 2% v/v MeOH; **(b)** CD spectra of the same ETH solutions, d = 2.0 cm. **(c)** Calculated CD spectra (in molar ellipticity) of ETH, pβCyD and the 1:1 complex and **(d)** Equilibrium concentrations of ETH, βCyD and the 1:1 complex with increasing total βCyD concentration in the polymer obtained for $\log(K_{1:1}/M^{-1}) = 2.00 \pm 0.02$; **(e)** CD spectra of 5×10^{-5} M ETH solutions with 12 mg/ml pβCyD obtained dissolving ETH film (green line) or mixing ETH MeOH aliquot with aqueous carrier solution (red line), d = 2.0 cm.

2.5 ETH interaction with fluorescein labeled polymeric βCyD

In view of future *in vitro* experiments focusing on the cellular uptake and intracellular trafficking of pβCyD carriers, loaded or not with ETH, a βCyD polymer labeled with fluorescein was synthesised (Scheme 2.2).

21
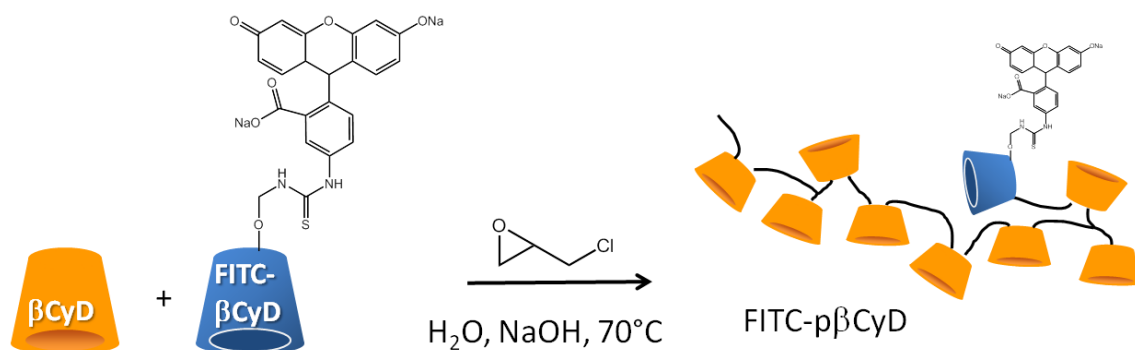
Scheme 2.2 Cartoon representation for the preparation of FITC-pβCyD using crosslinking with epichlorohydrin

Monomeric fluorescein labeled βCyD (FITC-βCyD), was prepared by Cyclolab according to a procedure already described.[13] Next, polymeric FITC-pβCyD was prepared by crosslinking a mixture of βCyD and FITC-βCyD (1%) with epichlorohydrin.[13]
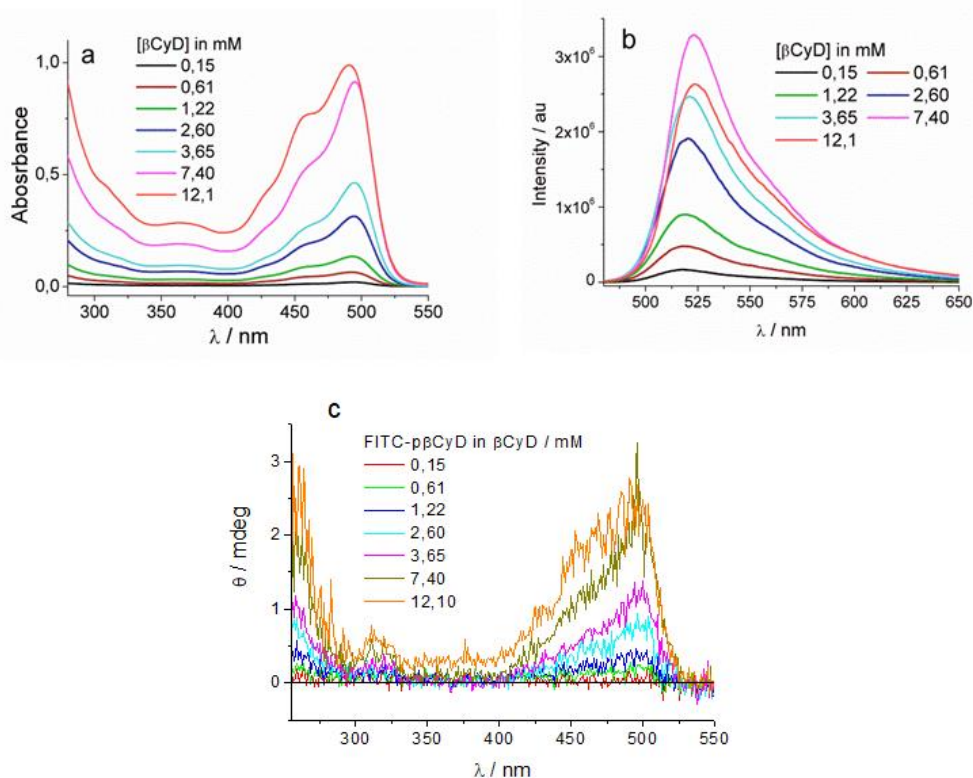
Figure 2.4 (**a**) Absorption spectra in water of the polymer FITC-pβCyD (range 0.15-12.1 mM in βCyD units), d = 1.0 cm; (**b**) Fluorescence spectra of the same solutions excited at 470 nm;. (**c**) Circular Dichroism spectra of the polymer FITC-pβCyD in water. The spectra of a pure water reference has been subtracted.

The photophysical behaviour of this polymer as well as its interaction with ETH were explored. Figures 2.4a-c show the absorption and fluorescence spectra of increasing concentrations of FITC-pβCyD in water together with the CD spectra characterised by a positive band in the 400–550 nm visible region due to the FITC moiety experiencing the chiral βCyD environment. It is clear from Figure 2.4a that the molar absorption coefficient is not directly proportional to the FITC concentration, particularly when reaching the

highest studied polymer concentration of 2.5×10^{-5} M (corresponding to 12.1 mM βCyD concentration).

To shed light on these findings, effect of the pH was investigated by performing a pH titration on FITC-pβCyD solutions monitoring both the absorption and fluorescence properties. It is known that monoanionic fluorescein, behaving as acid, has a pKa value of 6.3 and the two biologically relevant anionic forms behave differently from the photophysical point of view.[14] Indeed, the dianion has a molar absorption coefficient of 87 700 $M^{-1}cm^{-1}$ peaking at 490 nm while the monoanion has a molar absorption coefficient of 16 400 $M^{-1}cm^{-1}$ at 490 nm and 31 900 $M^{-1}cm^{-1}$ at 475 nm.[14,15,16]
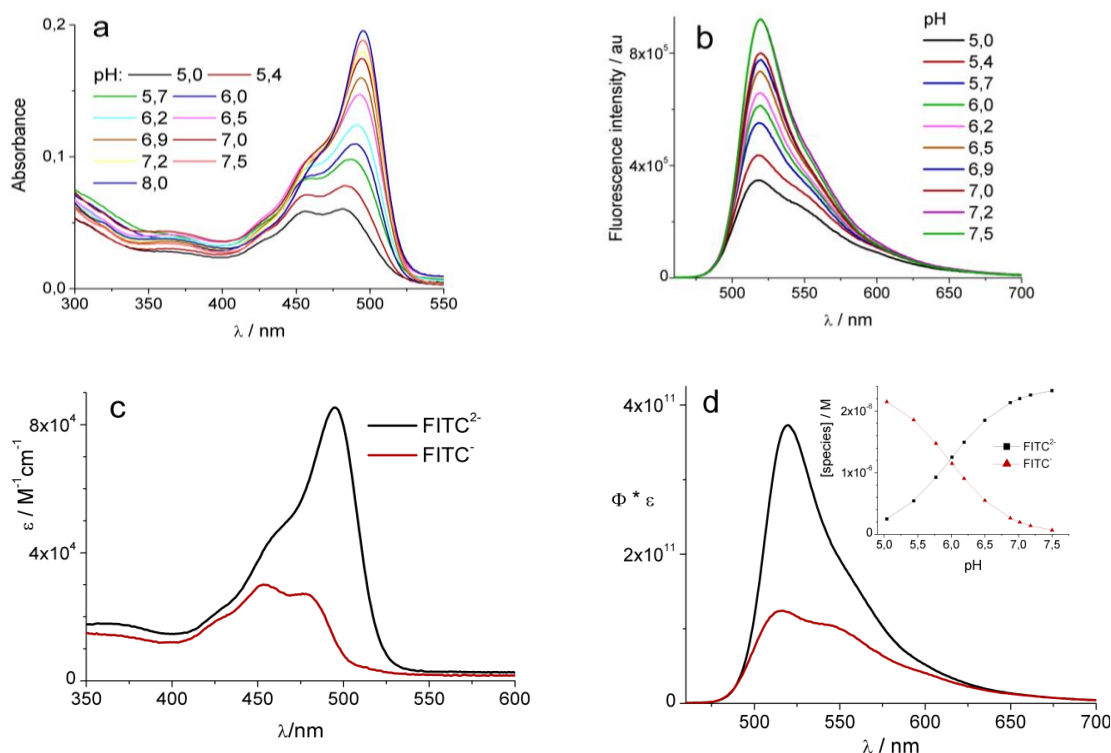
Figure 2.5 (**a**) Absorption spectra in water of the polymer FITC-pβCyD (1.22 mM in βCyD units) recorded in the pH range 5.0-8.0, d = 1.0 cm; (**b**) Fluorescence spectra of the same solutions excited at 440 nm. (**c-d**) Calculated absorption and fluorescence spectra of the monoanionic and dianionic form of FITC-pβCyD with the pK_a value 5.98 and 5.97, respectively, inset: the two species equilibrium concentrations at different pH values.

Our multiwavelength global analysis of the absorption and fluorescence spectra (Figures 2.5 a-b) of FITC-pβCyD afforded pKa values of 5.98 and 5.97, respectively. The calculated absorption and fluorescence spectra are reported in Figures 2.5 c-d and strongly resemble those reported for fluorescein in water.[17] The somewhat lower pKa value of FITC-pβCyD implicates that at physiological pH the dianionic form, ten times more abundant than the monoanion, is the main species present. The fluorescence decay was measured for all solutions exciting at 465 nm and monitoring decay at 530 nm. Global

analysis of all collected decays with a biexponential decay function enabled calculating two lifetimes of 1.32 ns and 4.55 ns with, respectively, descending and ascending pre-exponential factor with pH increase (Table 2.1).

Table 2.1 Fitting parameters of the global analysis with a biexponential function of the fluorescence decays of the FITC-pβCyD solutions at different pH values.

pH	a_1 for $\tau_1 = 1.32$ ns	a_2 for $\tau_2 = 4.55$ ns	χ^2	τ_{av}/ns
5.04	0.016	0.046	1.2	4.25
5.44	0.016	0.045	1.1	4.24
5.77	0.0115	0.049	1.0	4.34
6.01	0.011	0.049	1.0	4.35
6.19	0.009	0.050	1.1	4.34
6.50	0.009	0.050	0.95	4.40
6.88	0.007	0.052	1.1	4.42
7.02	0.006	0.053	1.0	4.44
7.18	0.005	0.054	1.0	4.47
7.50	0.005	0.053	1.0	4.46
8.01	0.003	0.054	1.0	4.50

At pH 8 the fluorescence decay of the FITC-pβCyD polymer can also be perfectly fitted with a mono-exponential function yielding a lifetime of 4.51 ns. The long lifetime can thus reasonably be assigned to the dianion and it is comparable to the one reported for fluorescein (4.30 ns).[17] The short lifetime is likely due to the fluorescein monoanion in the polymer, but is significantly shorter than the lifetime reported in literature, 3.70 ns, for the fluorescein monoanion measured in 1 mM phosphate buffer in the pH range 6.0–8.0.[17] The same authors have anyway reported a similar short lifetime value for fluorescein in the presence of 1 M phosphate buffer indicating that the buffer is participating in the fast equilibration of the two anionic excited species through excited state proton transfer. If two fluorescent species in solution excited at the same wavelength exhibit overlapping emission and decay independently, the fluorescence decay is biexponential. In this case the pre-exponential factors a_i depend on (i) the concentration, (ii) the molar absorption coefficient at the excitation wavelength, and (iii) the intensity at the observed emission wavelength of the emitting species. In the case of the FITC pβCyD only the concentration of the two anions is changing with pH, see Figure 2.5d inset, so the ratio of the concentrations should be the same as the ratio of the pre-exponential factors. As this is not the case, it can be concluded that other processes might influence the decay behaviour of

24

the two species which are not decaying independently. Since there's no buffer present in the polymer solution the FITC pβCyD is likely responsible and may participate in a proton transfer reaction in the excited state generating the dianonic species. Excited state proton transfer seems to occur on sub-ns time scale since the decay analysis did not evidence any negative pre-exponential factors.

The solutions with the absorption spectra in Figure 2.3a have pH values decreasing from 7.0 to 6.7 for the most concentrated FITC-pβCyD solution. Considering the pKa value 5.98 of the fluorescein monoanion in FITC-pβCyD polymer the ratio of the dianionic to monoanionic concentration decreases from 10 to 4 for the most concentrated polymer solution with pH 6.7. Therefore the observed spectral behaviour of the polymer solutions in Figure 2.3a can be assigned to increasing monoanionic fluorescein concentration in line with the pH titration data. Surprisingly, the long fluorescence lifetime of the labeled polymer is increasing with concentration from 4.35 ns to 5.10 ns (Table 2.2).

Table 2.2 Parameters of the fitting with biexponential function of the fluorescence decays of the FITC-pβCyD solutions of different concentrations

	fluorescein monoanion, F$^-$		fluorescein dianion, F^{2-}		
[βCyD]/mM	a_1	τ_1	a_2	τ_2	χ^2
0.15	0.005	2.23	0.053	4.34	1.1
0.61	0.007	2.20	0.053	4.42	1.1
1.22	0.005	1.58	0.056	4.44	1.1
2.60	0.005	1.30	0.055	4.59	1.1
3.65	0.005	1.68	0.054	4.73	1.0
7.4	0.004	1.37	0.055	5.00	1.0
12.1	0.005	1.42	0.053	5.10	0.9

The monoanionic species with the shorter fluorescence lifetime is hardly discernible with fractional intensity below 3% and disappearing completely at high concentrations. Again this is in line with the role played by the polymer itself favoring formation of the dianion likely through proton transfer. Moreover the fluorescence lifetime is very sensitive to the fluorophore local environment and intermolecular complexation of FITC molecules by βCyD units may be responsible for local changes and lifetime lengthening. It is known that FITC binds to βCyD with a log value of the association constant of 2.5 for the 1:1 complex and complexed FITC has a fluorescence lifetime of 4.6 ns in aqueous medium of pH 11 to be compared with 4.3 ns without βCyD at pH 11. Moreover binding to βCyD does not

significantly affect the absorption spectrum while a positive CD signal around 480 nm has been reported as indication of complexation.[18,19] Our CD spectra of FITC-pβCyD characteried by a positive band in the 400–550 nm visible region confirm that the FITC molecule is probably experiencing the chiral environment not only of the βCyD unit attached to the fluorophore but also intra and inter-molecular ones, especially at high concentrations. On the basis of these results we hypothesise that small pH changes in a critical range account for the hypochromic effect in the absorption spectra at the highest concentrations. Changes in the fluorescein local environment possibly due to the formation of tiny aggregates may explain the fluorescence lifetime lengthening with increasing concentration. The low fractional contribution of the monoanion in the overall fluorescence may be due to excited state proton transfer to the several alcoholic groups of the polymer involved in hydrogen bonds with their host occuring on very short time scales. Finally, in order to assess whether the loading of ETH would modify the properties of the FITC-pβCyD, the same spectroscopic and fluorescence study was performed. Complexation of ETH has been monitored keeping the drug concentration constant. In particular absorption and CD revealed changes useful to evaluate complexation ability of the labeled polymer. Figure 2.6a shows the absorption spectra of the reference solutions (lines and symbols), and the mixtures (lines). After subtraction two variations suggest complexation of ETH: i) a small shift of the maximum at 285 nm (peak mainly due to ETH) and ii) an increase in the visible FITC absorption band peaking at 498 nm. Binding of ETH to the polymer seems to favour the deprotonation of the FITC monoanion. High negative atomic charges have been reported for both nitrogens and the sulfur atom of ETH strongly involved in hydrogen bonding interactions.[20] Possibly these negatively charged atoms can act as proton acceptor in the complex favoring the deprotonation of FITC. Figure 2.6b shows the CD spectra of the mixtures subtracting the spectra of the polymer reference solutions. Below 420 nm the CD spectra have a signature in part similar to that of ETH/βCyD system. It can thus be concluded that FITC-pβCyD is also complexing ETH. To evaluate ETH affinity a simplified approach was used in which the host concentration is expressed in βCyD units, according to the known βCyD content of 70% w/w in the FITC pβCyD polymer. We assumed a 1:1 complexation stoichiometry when analysing the CD data of the subtracted spectra in the 260-450 nm range. We considered ETH alone and the polymer as not having any CD signal in this spectral range. The best fit was found for an apparent binding constant with $\log(K_{1:1}/M^{-1}) = 1.70 \pm 0.06$ and afforded the spectra in Figure 2.6c. On one hand, the binding constant is not significantly affected

by fluorescein grafting at this low labeling % compared to the monomer. On the other hand, the binding constant of FITC-pβCyD is less favorable compared to the one of pβCyD NPs. In the labeled polymer not all the βCyD cavities may be equally accessible as some may be involved in the interaction with FITC. We have also monitored the fluorescence of the FITC label upon complexation of the drug exciting the label at 470 nm. Data are shown in Figure 2.6d. Interestingly the complexation of ETH does not quench the fluorescence of the FITC label. Indeed, comparing the fluorescence intensity of the mixture with that of the reference we generally observe a higher intensity in the mixture containing ETH. In the presence of ETH the decay of FITC was monoexponential in all cases and the fluorescence lifetime increased from 4.26 ns to 5.3 ns, which represents a positive feature in view of the further development of the CyD-based carriers. Finally we tested the loading capacity of this carrier. With 50 mg/ml carrier up to 4 mM of ETH could be dissolved.
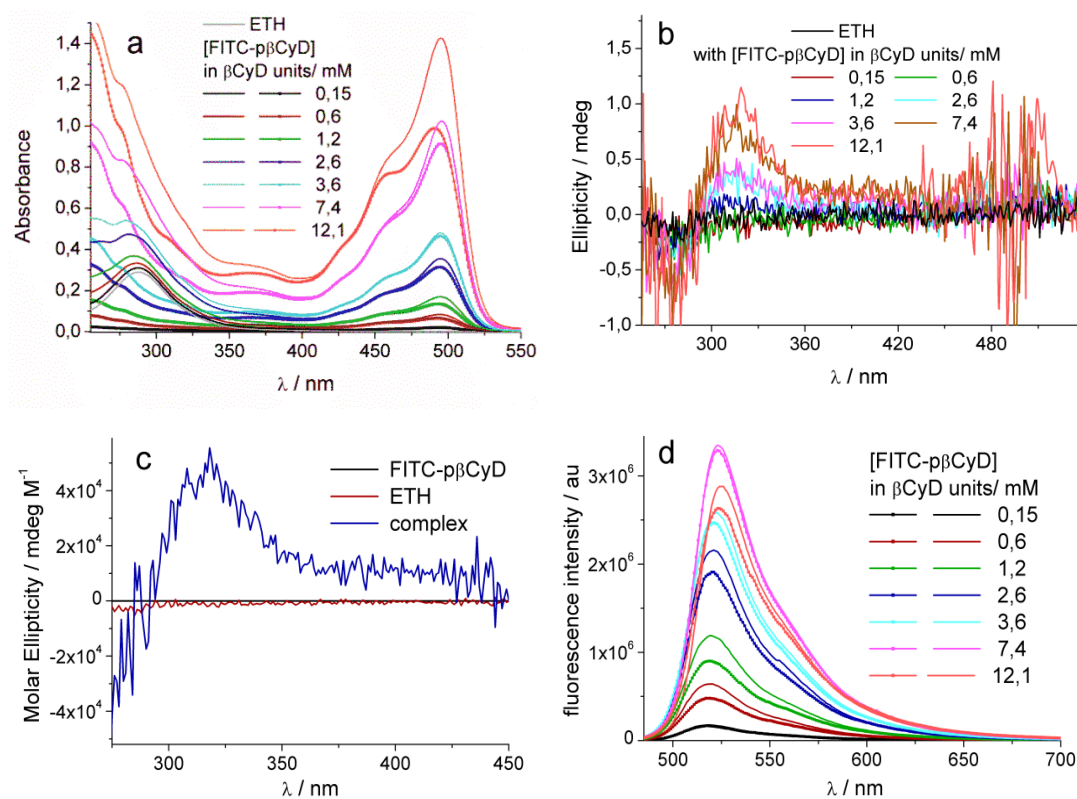
Figure 2.6 (a) Absorption spectra in water of 3×10^{-5} M ETH solutions (line) with increasing FITC-pβCyD concentration (range 0.15-12.1 mM in βCyD units) and the reference solutions (line and symbol) containing only the polymer, d = 1.0 cm. Note all samples contain 1% v/v MeOH; **(b)** CD spectra of the same ETH solutions, d = 2.0 cm subtracting the spectra of the polymer reference solutions. **(c)** Calculated CD spectra (in molar ellipticity) of ETH, FITC-pβCyD and the 1:1 complex obtained for a binding constant with log($K_{1:1}$/M^{-1}) = 1.70 ± 0.06. **(d)** Fluorescence spectra in water of 3×10^{-5} M ETH solutions (line) with increasing FITC-pβCyD concentration (range 0.15-12.1 mM in βCyD units) and the reference solutions (line and symbol) containing only the polymer; excitation at 470 nm. Note that all couples of mixtures and references have the same absorbance at the excitation wavelength except for the highest polymer concentration so only in this case we normalised the intensity for the absorbance the two samples.

2.6 ETH interaction with NBF-NH-γ CyD citric acid crosslinked polymer

We performed a preliminary study of the ETH interaction with nitrobenzofurazanyl-NH-γCyD/Citric acid polymer. γCyD citric acid crosslinked polymer was synthesised using γ CyD and citric acid in 1 : 3 and 1:5 molar ratios, respectively.[13,21] A 3×10^{-5} M ETH solution was mixed with 1 mg/ml solution of NBF-NH-γCyD/Citric acid Polymer. In the absorption spectra, we observe ETH maxima at 280 nm and polymer maxima at 335 and 475 nm due to nitrobenzofurazanyl moiety absorbing in visible.
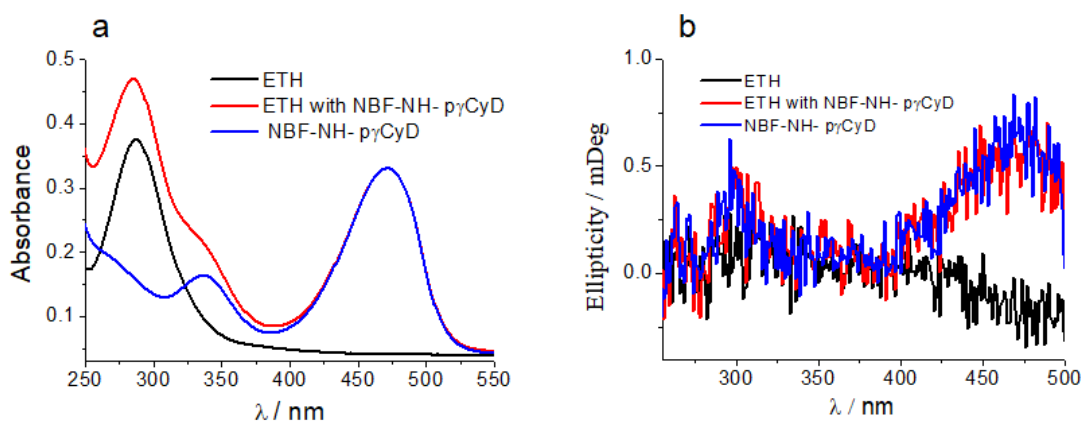
Figure 2.7 (**a**) Absorption spectra 3×10^{-5} M ETH with 1mg/ml NBF-NH-γCyD/Citric acid polymer; (**b**) Circular Dichroism spectra of the 3×10^{-5} M ETH with 1mg/ml NBF-NH-γCyD/Citric acid polymer. d = 1.0 cm.

The CD spectrum of ETH in the presence of this polymer is diffferent from that of the ETH complex with βCyD or pβCyD. It does not show the ETH signal discussed above but only the signal of nitrobenzofurazanyl group (Figure 2.7). A reason for this behaviour may be the larger cavity of the γCyD not allowing to establish the necessary interactions between drug and carrier to obtain a stable complex with chiral features. The results do not give a clear indication that this carrier is complexing well so we have not investigated the system further.

2.7 Conclusions

We have successfully studied the complexation of ETH with βCyD and pβCyD. Chirality induced upon complexation gives strong evidence of ETH complex formation with fair binding constants. Comparison of the CD spectra of ETH with βCyD and pβCyD suggests that ETH experiences more than one environment in the polymeric carrier. Interstingly, the fluorescence properties of the labeled polymer were improved after complexation with ETH. These promising results allow further development of these polymeric carriers for the delivery of ETH.

2.8 References

1. R. Laxminarayan, A. Duse, C. Wattal, A. K. Zaidi, H. F. Wertheim, N. Sumpradit, E. Vlieghe, G. L. Hara, I. M. Gould and H. Goossens, *Lancet Infect. Dis.*, **2013**, 13, 1057-1098.
2. M. Flipo, M. Desroses, N. Lecat-Guillet, B. Villemagne, N. Blondiaux, F. Leroux, C. Piveteau, V. Mathys, M.-P. Flament and J. Siepmann, *J. Med. Chem.*, **2011**, 55, 68-83.
3. S. D. Ahuja, D. Ashkin, M. Avendano, R. Banerjee, M. Bauer, J. N. Bayona, M. C. Becerra, A. Benedetti, M. Burgos and R. Centis, *PLoS Med.*, **2012**, 9, e1001300.
4. S. Thee, A. Garcia-Prats, P. Donald, A. Hesseling and H. Schaaf, *Tuberculosis*, **2016**, 97, 126-136.
5. G. Kumar, S. Sharma, N. Shafiq, P. Pandhi, G. K. Khuller and S. Malhotra, *Drug Deliv.*, **2011**, 18, 65-73.
6. N. Vale, E. Mäkilä, J. Salonen, P. Gomes, J. Hirvonen and H. A. Santos, *Eur. J. Pharm. Biopharm.*, **2012**, 81, 314-323.
7. M. E. Davis, *Adv. Drug Del. Rev.*, **2009**, 61, 1189-1192.
8. J. Cheng, K. T. Khin and M. E. Davis, *Mol. Pharm.*, **2004**, 1, 183-193.
9. K. Uekama, K. Ikegami, Z. Wang, Y. Horiuchi and F. Hirayama, *J. Pharm. Pharmacol.*, **1992**, 44, 73-78.
10. E. Renard, A. Deratani, G. Volet and B. Sebille, *Eur. Polym. J.*, **1997**, 33, 49-57.
11. M. Othman, K. Bouchemal, P. Couvreur, D. Desmaële, E. Morvan, T. Pouget and R. Gref, *J. Colloid Interface Sci.*, **2011**, 354, 517-527.
12. R. B. Dyer, R. A. Palmer, R. G. Ghirardelli, J. S. Bradshaw and B. A. Jones, *J. Am. Chem. Soc.*, **1987**, 109, 4780-4786.
13. M. Malanga, M. Bálint, I. Puskás, K. Tuza, T. Sohajda, L. Jicsinszky, L. Szente and É. Fenyvesi, *Beilstein J. Org. Chem.*, **2014**, 10, 3007.
14. N. Klonis and W. H. Sawyer, *J. Fluoresc.*, **1996**, 6, 147-157.
15. L. D. Lavis, T. J. Rutkoski and R. T. Raines, *Anal. Chem.*, **2007**, 79, 6775-6782.
16. R. Sjöback, J. Nygren and M. Kubista, *Spectrochim. Acta A*, **1995**, 51, L7-L21.
17. J. M. Alvarez-Pez, L. Ballesteros, E. Talavera and J. Yguerabide, *J. Phys. Chem. A*, **2001**, 105, 6320-6332.
18. L. N. Bogdanova, N. O. Mchedlov-Petrossyan, N. A. Vodolazkaya and A. V. Lebed, *Carbohydr. Res.*, **2010**, 345, 1882-1890.
19. L. Flamigni, *J. Phys. Chem.*, **1993**, 97, 9566-9572.
20. G. Rajalakshmi, M. S. Pavan and P. Kumaradhas, *RSC Adv.*, **2014**, 4, 57823-57833.
21. R. Anand, M. Malanga, I. Manet, F. Manoli, K. Tuza, A. Aykaç, C. Ladavière, E. Fenyvesi, A. Vargas-Berenguel and R. Gref, *Photochem. Photobiol. Sci.*, **2013**, 12, 1841-1854.

Chapter 3

Co-encapsulation of ETH and booster BDM43266 in pβCyD NPs

3.1 Introduction

Treatments with ETH, the drug selected for our study, require high therapeutic doses due to its limited efficacy often accompanied by severe side effects. Indeed, ETH is a prodrug and requires to be activated in order to exert its therapeutic activity against *M. tuberculosis*.[1] The mycobacteria produce the enzyme EthA, a monooxygenase that uses flavin adenine dinucleotide (FAD) as a cofactor and is NADH- and O_2-dependent for the conversion of the ETH prodrug to active S-oxide metabolite. Once ETH is converted in its active sulphoxide form, mainly in the liver, it inhibits cell wall biosynthesis. The production of the enzyme EthA is controlled by the transcriptional regulator EthR able to inhibit expression of EthA. Mycobacterium species which overexpress EthA are highly sensitive to ETH and species which overexpress EthR are resistant to ETH.[1] Importantly, new synthetic organic molecules have been discovered able to bind to the DNA binding site of EthR thus inhibiting its activity and increasing the efficacy of ETH as EthA expression is no longer repressed. These molecules, called boosters, have proven to be able to potentiate in vitro and in vivo efficacy of ETH against tuberculosis when co-administered consequently reducing side effects.[2, 3] The discovery of the "Booster" family in the past few years is a step ahead in the fight against MDR TB as it may help to upgrade ETH to a first line drug able to substitute other drugs suffering MDR. The boosters were selected through fragment screening and structure based molecular design. Among them booster BDM43266 (see Scheme 3.1) resulted in a 400-fold improved EthR inhibition activity compared to the starting hit fragment and a 10-fold activity increase of ETH with a very low inhibitory concentration of 80 nM.[4]

In this context, co-administration of the ETH/ booster pair is very appealing but associated with several challenges due to relatively poor aqueous solubility of the boosters. We have applied a nanoparticle-based approach in which polymeric cyclodextrins (CyD) have been used for simultaneous incorporation of the ETH/booster pair. In this chapter, we discuss the interaction of pβCyD NPs (the same discussed in chapter 2) with 5 selected boosters. Next we report on co-encapsulation of ETH and the selected booster BDM43266, studied

in depth by means of optical spectroscopic and chromatographic techniques as well as a molecular dynamics (MD) approach.

| **Scheme 3.1** | Ethionamide, ETH | Booster BDM43266 |
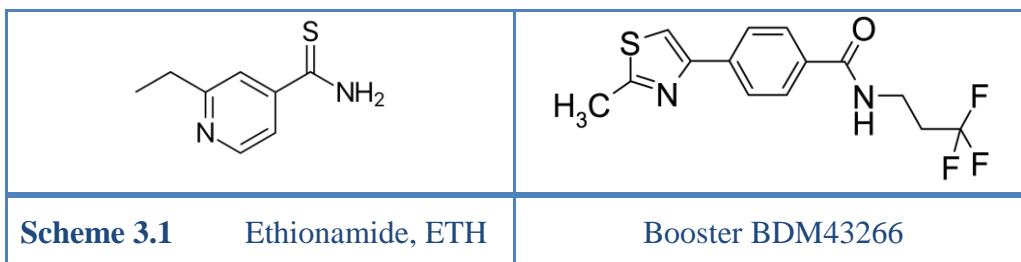
3.2 Study of the interaction of a family of boosters with pβCyD NPs

Initially, photophysical properties of all boosters (scheme 3.1 and 3.2) were assessed by means of optical spectroscopy. Booster molecules were dissolved in pure DMSO and water-DMSO mixtures to register the absorption and fluorescence spectra with DMSO content not exceeding 5% v/v.

Scheme 3.2 Chemical structure of boosters
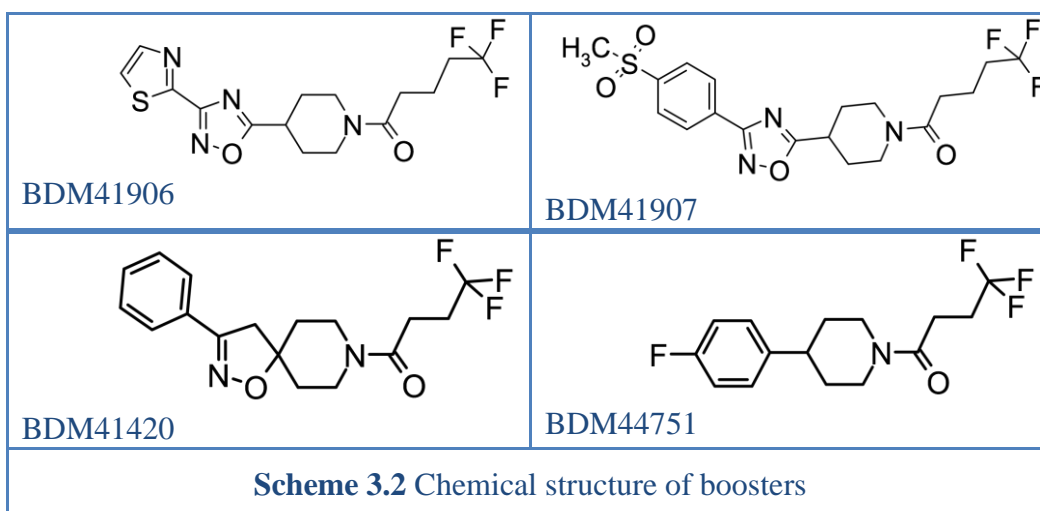
Table 3.1. Absorption maxima of BDM41907, BDM41906, BDM41420, BDM44751 and BDM43266 solutions in pure DMSO and DMSO/H$_2$O mixture and binding constant of BDM41907, BDM41906, BDM41420, and BDM43266 with pβCyD .

	Pure DMSO		**DMSO/H$_2$O Mixture**		**pβCyD**
Sample	λ (nm)	ε (M^{-1}cm$^{-1)}$	λ (nm)	ε (M^{-1}cm^{-1})	Log (K$_{1:1}$/M^{-1})
BDM41907	242, 280	1172	242 , 280	2672	2.59 +/- 0.01
BDM41420	265	17170	260	17016	3.37 +/- 0.02
BDM43266	288	24480	280	17428	3.03 +/- 0.01
BDM41906	278	10840	278	11 250	2.28 +/- 0.05
BDM44751	263	1174	263	930	-

ε (M^{-1}cm^{-1}) - Molar absorption coefficient, K (M^{-1}) - Binding constant

Figure 3.1 and Table 3.1 collect the booster absorption spectra and maxima, molar absorption coefficients in DMSO and DMSO/H_2O mixture, respectively. None of the boosters is chiral, so no CD signals have been observed when dissolved in pure solvents.
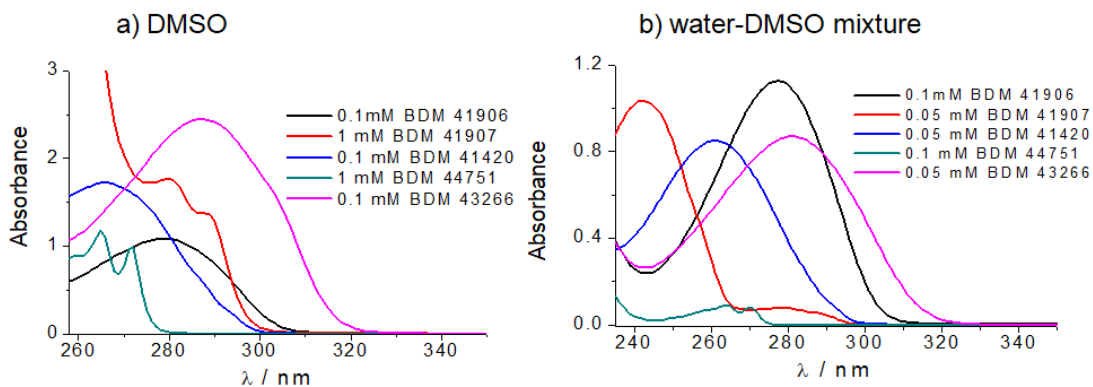
Figure 3.1 (**a**) Absorption spectra of BDM41907, BDM41906, BDM41420, BDM44751 and BDM43266 solutions in pure DMSO; (**b**) Absorption spectra of BDM41907, BDM41420, BDM43266 solution in DMSO/H_2O mixture (5% v/v DMSO), and BDM41906, BDM44751 solutions in DMSO/H_2O mixture (10% v/v DMSO), d = 1.0 cm.

Next, we used an optical spectroscopic approach to determine booster affinity for pβCyD NPs. We titrated constant amounts of 1×10^{-5} M BDM41906, 5×10^{-5} M BDM41907 and 5×10^{-6} M BDM41420, 5×10^{-6} M BDM43266 and 1×10^{-4} M BDM44751 with pβCyD NPs solutions of increasing concentration (0.3-7.55$\times10^{-3}$ M in βCyD units considering the polymer contains 70% w/w βCyD). We recorded the absorption, fluorescence and circular dichroism spectra of the titration mixtures and the most interesting data are shown in Figures 3.2, 3.3, 3.4 and 3.5. Note that none of the boosters is chiral, so only induced CD spectra can be observed in the presence of the carrier. The only booster that displayed an induced CD signal that could be exploited to evaluate the binding constant is booster BDM41420. As other techniques confirm that encapsulation occurs, the lack of induced CD is likely due to conformational freedom of the booster when complexed by the CyDs. Multiwavelength global analysis was performed for all booster titration data and we have calculated the equilibrium binding constant values reported in table 3.1 except for the booster BDM 44751. This booster displays no significant changes in its optical properties upon increasing polymer concentration allowing to calcalute the binding constant. Booster BDM43266 is discussed more in detail as is the only one used for co-encapsulation with ETH in the polymer.
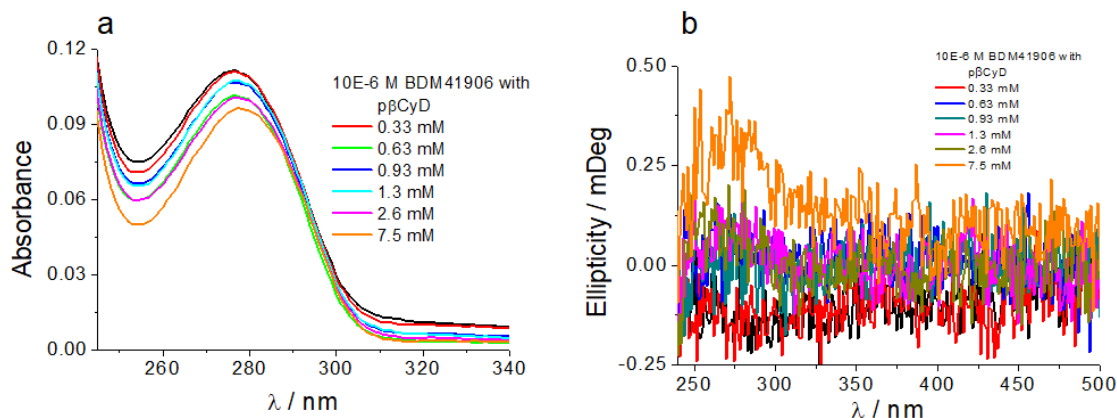
Figure 3.2 (**a**) Absorption spectra of 1×10^{-5} M BDM41906 solutions with increasing pβCyD concentration (range 0.3-7.5 mM βCyD unit) in water, d = 1.0 cm; all samples contain 1% v/v DMSO; (**b**) Circular Dichroism spectra of 10×10^{-6} M BDM41906 solutions with increasing pβCyD concentration, d = 1.0 cm. Binding constant obtained from the absorption spectra has log $(K_{1:1}/M^{-1})$ = 2.28 +/- 0.05.
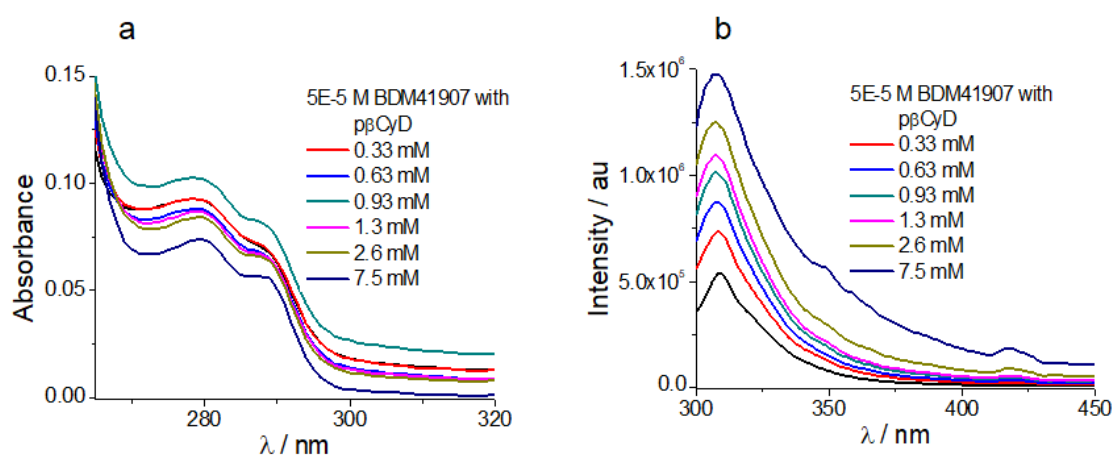
Figure 3.3 (**a**) Absorption spectra of 5×10^{-5} M BDM41907 solutions with increasing pβCyD concentration (range 0.3-7.5 mM βCyD unit) in water, d = 1.0 cm; all samples contain 5% v/v DMSO; (**b**) Fluorscence spectra of 5×10^{-5} M BDM41907 solutions with increasing pβCyD concentration, d = 1.0 cm and λ_{exc} = 280 nm. Binding constant obtained from the fluorescence spectra has log $(K_{1:1}/M^{-1})$ = 2.59 +/- 0.01.
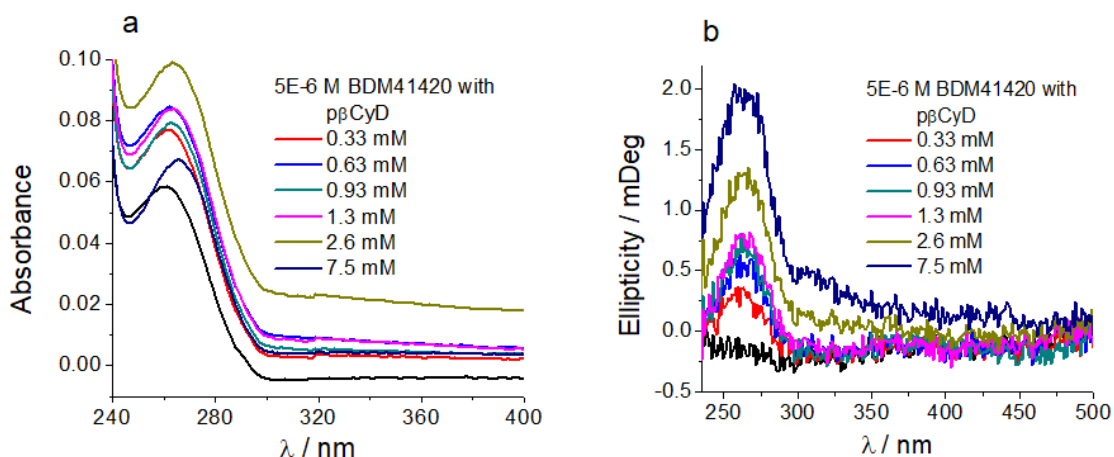
Figure 3.4 (**a**) Absorption spectra of spectra of 5×10^{-6} M BDM41420 solutions with increasing pβCyD concentration (range 0.3-7.5 mM βCyD unit) in water, d = 1.0 cm; all samples contain 1% v/v DMSO; (**b**) CD spectra of 5×10^{-6} M BDM41420 solutions with increasing pβCyD NPs concentration in water, d = 1.0 cm. Binding constant obtained from the CD spectra has log $(K_{1:1}/M^{-1})$ = 3.37 +/- 0.02.
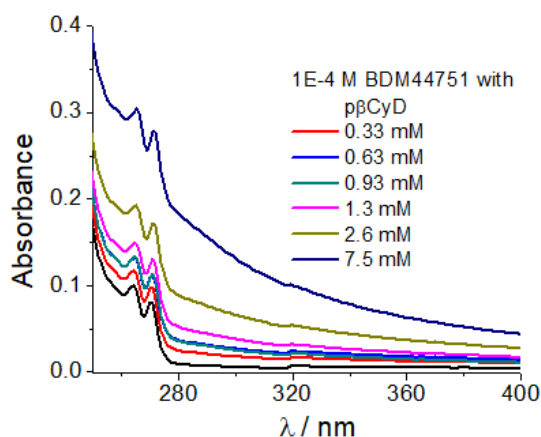
Figure 3.5 Absorption spectra of 1×10^{-4} M BDM44751 (10% DMSO) solutions with increasing pβCyD concentration (range 0.3-7.5 mM βCyD unit) in water, d = 1.0 cm.

The interaction of BDM43266 with pβCyD NPs was investigated by absorption, CD and fluorescence spectroscopy. Booster BDM43266 in Scheme 3.1 is a synthetic non-chiral thiazole-phenyl derivative having an intrinsic fluorescence signal. We titrated 5 μM BDM43266 solutions both with βCyD and pβCyD NPs solutions of increasing concentration. The absorption and fluorescence spectra of the titrations are displayed in Figure 3.6 and 3.7 for the polymer and monomer, respectively. In the absorption spectra in the presence of the polymer we can observe a very small shift to the red of the maximum at 280 nm. In Figure 3.6 the fluorescence spectra show a decrease in intensity and a strong blue shift of 24 nm of the maximum from 375 nm to 351 nm with increasing pβCyD concentration and confirm that complexation has occurred. Global analysis of the fluorescence spectra afforded the equilibrium binding constant with a $\log(K_{1:1}/\ M^{-1})$ value of 3.03±0.01. This value of binding constant is higher than that of ETH. We have obtained a higher binding constant for BDM43266 with the polymer compared to the monomer. Global analysis of the fluorescence data shown in Figure 3.7 yields a $\log(K_{1:1}/\ M^{-1})$ value of 2.20 ± 0.03 confirming again the better complexation ability of the polymer with respect to the monomer. Figure 3.6c shows the calculated fluorescence spectrum of the complex with the polymer. The large Stokes shift between the absorption maximum and the fluorescence maximum observed for the booster alone persists also in the booster complex. This is typically interpreted as strong nuclear reorganisation in the excited state. Apparently BDM43266 is still able to reorganise even in the more constrained environment inside the crosslinked pβCyD NPs. This conformational flexibility in the complex is also in line with BDM43266 not exhibiting any induced circular dichroism

34

signal with βCyD or pβCyD NPs (see also below). Among all boosters, BDM43266 has been chosen for further co-encapsulation with ETH discussed thoroughly hereafter.
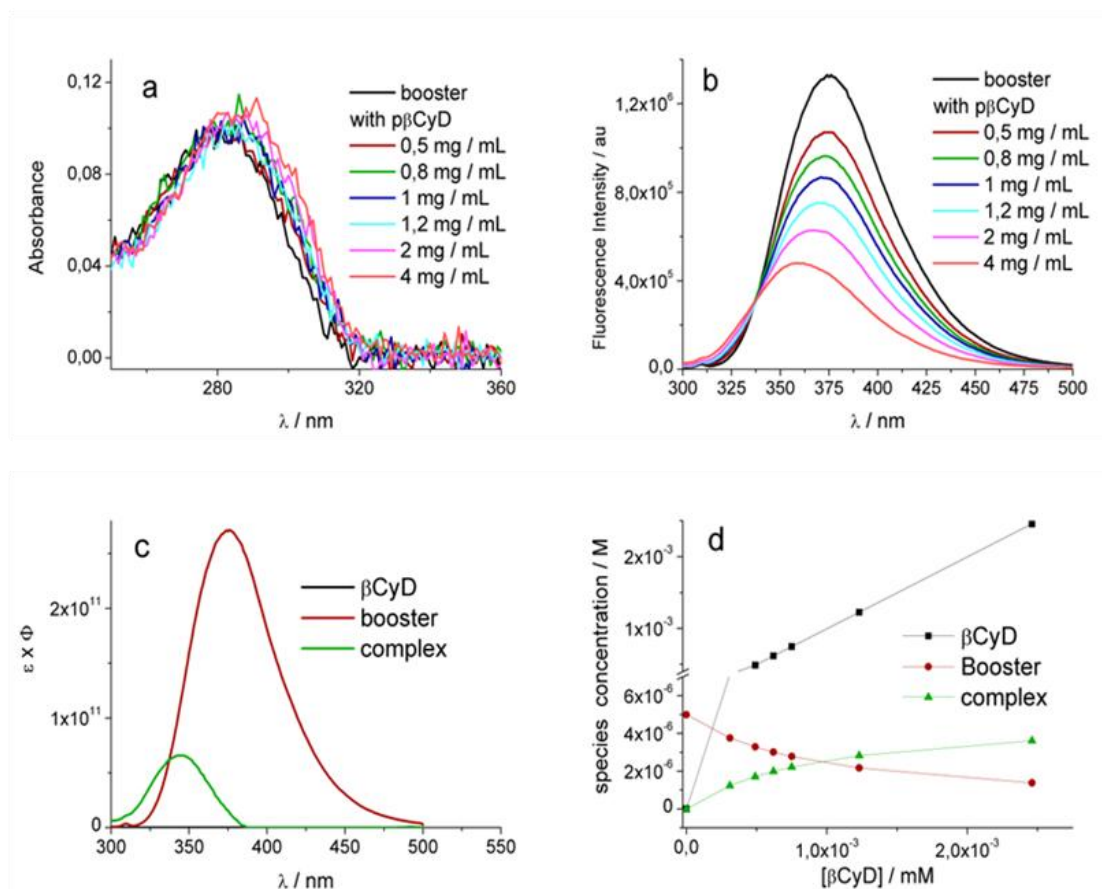
Figure 3.6 (**a**) Absorption spectra of 5×10^{-6} M booster BDM43266 solutions with increasing pβCyD NPs concentration (range 0.5-4 mg/ml) in water, d = 1.0 cm; spectra recorded using the integrating sphere. Note all samples contain 1% v/v DMSO to solubilise BDM43266; (**b**) Fluorescence spectra of the same BDM43266 solutions, d = 1.0 cm and λ_{exc} = 280 nm. (**c**) Calculated fluorescence spectra (in molar intensity) of BDM43266, pβCyD NPs and the 1:1 complex and (**d**) Equilibrium concentrations of BDM43266, βCyD and the 1:1 complex with increasing total CyD concentration in the polymer obtained for $\log(K_{1:1}/M^{-1})$ = 3.03 ± 0.01.
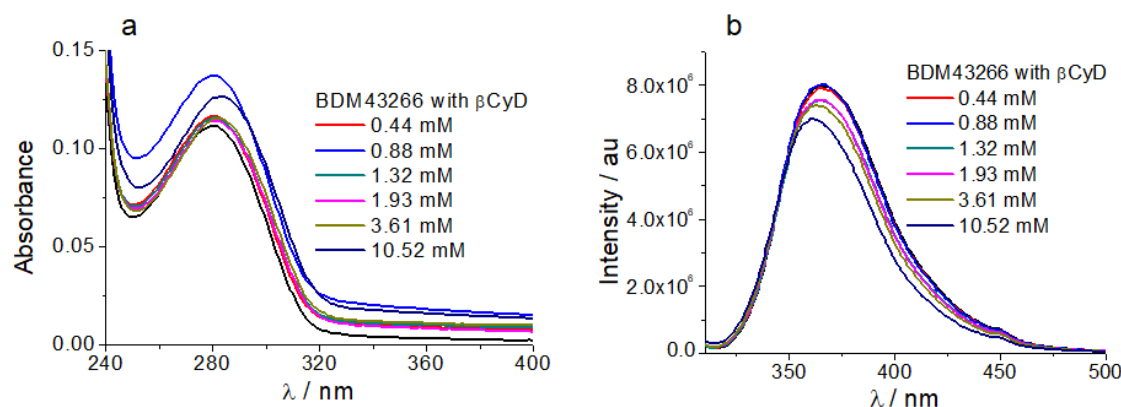
Figure 3.7 (**a**) Absorption spectra of 5×10^{-6} M BDM43266 with increasing concentrations of the βCyD (0.44-10.52 mM range) ; (**b**) Fluorescence spectra of 5×10^{-6} M BDM43266 with increasing concentrations of the βCyD (0.44-10.52 mM range); 1% v/v DMSO in the final mixtures. d = 1.0 cm.

35

3.3 Phase solubility competition studies of ETH and BDM43266

For the phase solubility studies a green approach was used to study the co-encapsulation of drug and booster BDM43266. First, we developed a Reversed-Phase-HPLC method for the simultaneous detection and accurate quantification of the two different molecules. Then, the loading of ETH and BDM43266 in βCyD and pβCyD NPs was evaluated using a solubility method in water at room temperature.[5] Natural βCyD and pβCyD NPs aqueous solutions of incrementing concentrations (0–200 g/l for pβCyD NPs and 0–15 g/l for βCyD) were prepared in vials containing an excess amount of solid ETH or BDM43266. The aqueous dispersions were protected from light, and kept under magnetic stirring at 300 rpm until the equilibrium was reached after 3 days for both ETH and BDM43266. Afterwards, the excess amount of undissolved ETH and BDM43266 was eliminated by ultracentrifugation to obtain ETH or BDM43266 loaded βCyD and pβCyD NPs. Next, the drug and booster were successfully extracted from the NPs by using mixture of DMSO/Acetonitrile in 1:10 v/v ratio, followed by centrifugation to remove the precipitated pβCyD NPs. At that point, the solubilised drug and booster concentration in the supernatants was quantified by HPLC. We used a similar procedure to perform the competition studies of ETH and BDM43266 for the βCyD cavities in pβCyD NPs. Briefly, a fixed amount of one component was dissolved in pβCyD solutions of increasing concentration and kept under stirring for three days until saturation point reached, followed by elimination of the undissolved drug or booster by ultracentrifugation. In the second step, increasing amounts of the second component were introduced. Once equilibrium reached, pβCyD NPs containing both ETH and BDM43266 were obtained by removal of the undissolved second drug by ultracentrifugation followed by estimation of the drug and booster content in the NPs by HPLC. The phase solubility diagrams (Figures 3.8a-d) were obtained by plotting the mean solubility of ETH or BDM43266 against βCyD concentrations. In case of pβCyD NPs, the βCyD concentrations were calculated assuming that polymers contains 70% w/w βCyD.

The binding constant (K) was calculated using the regression curve of the initial straight part of the solubility diagrams by assuming a 1:1 stoichiometry. The slope and slope intercept with Y axis were used to calculate K according to the following equation:

$$K = \text{slope intercept}/S0(1 \text{ slope})$$

where S0 is ETH or BDM43266 solubility in water
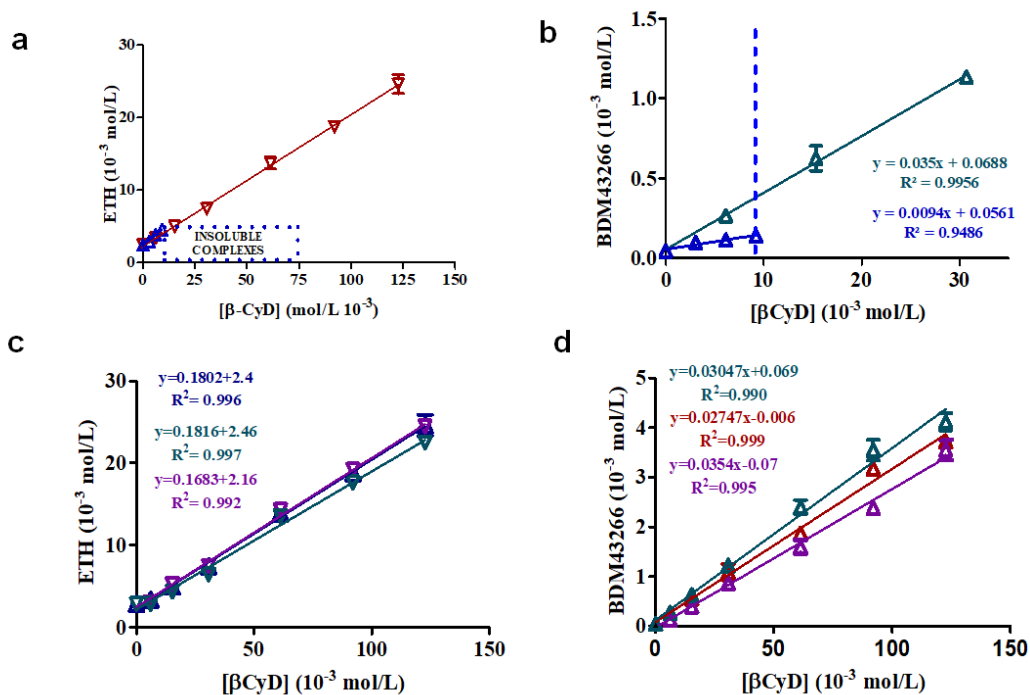
Figure 3.8. (a) Phase solubility diagrams of ETH in increasing concentration of βCyD (Δ) and pβCyD (∇); (b) Phase solubility diagrams of BDM43266 in increasing concentration of βCyD (Δ) and pβCyD NPs (Δ); **Competition studies (c and d). (c)** Phase solubility diagrams of ETH in pβCyD NPs (∇), of ETH in pβCyD NPs followed by the addition of BDM43266 (∇), and of ETH in pβCyD NPs containing Booster (∇); **(d)** Phase solubility diagrams of BDM43266 in pβCyD NPs (Δ), of BDM43266 in pβCyD NPs followed by the addition of ETH (Δ) and of BDM43266 in pβCyD NPs containing ETH (Δ). Data were obtained from the average of three different experiments performed by RP-HPLC analysis.

As shown in Figure 3.8b, the apparent solubility of BDM43266 increased linearly with increasing βCyD concentration up to the saturation solubility limit of βCyD (blue line). A similar result was obtained also for ETH/βCyD complex.[6] The obtained binding constant $\log(K_{1:1}/M^{-1})$ of ETH/βCyD and BDM43266/βCyD complexes were of 2.04 ± 0.04 and 1.57± 0.01, respectively (Table 3.2).

As to pβCyD NPs, a continuous linear increase of both BDM43266 and ETH solubility was observed with increase in pβCyD NPs concentration (Figure 3.8a-b). The phase solubility diagram, a typical AL-type[5] for the formation of soluble ETH/pβCyD NPs and BDM43266/pβCyD NPs complexes, afforded the binding constants of 1.90 ± 0.02 and 2.88 ± 0.03, respectively (Table 3.2). The high aqueous solubility of pβCyD NPs allowed a significant increase of the solubility of both ETH and BDM43266. Indeed, a pβCyD NPs concentration of 200 mg/ml is able to enhance about 10 times ETH aqueous solubility, while a βCyD concentration of 15 mg/ml (1.3×10^{-2} M) at saturation point allowed only a

2-fold increase of ETH apparent solubility. In the case of BDM43266, a pβCyD NPs concentration of 200 mg/ml leads to 90-fold increase of solubility while with native βCyD concentration of 15 mg/ml (1.3×10^{-2} M) only a 3-fold increase in solubility was obtained. So, ETH and BDM43266 having a very low solubility in water of 0.48 mg/ml and 0.01 mg/ml, respectively, were successfully incorporated into pβCyD NPs with this green approach resulting in a drug concentration of 4.2 and 1.2 mg/ml with 200 mg/ml pβCyD.

Table 3.2 Log value of the binding constant K obtained from the regression curves of the phase solubility diagrams of ETH and BDM43266. Log value of the binding constant K obtained in the competition studies from the solubility curves of ETH with pβCyD dissolved before or after BDM43266 and of BDM4366 with pβCyD dissolved before or after ETH.

Complex	*log K	Complex	*log K
ETH/βCyD	2.04 ± 0.04	BDM43266/βCyD	1.57 ± 0.01
ETH/pβCyD	1.90 ± 0.02	BDM43266/pβCyD	2.88 ± 0.03
Competition Studies	**logK ETH**	**logK BDM43266**	
pβCyD ETH + BDM43266	1.88 ± 0.02	2.81 ± 0.03	
pβCyD BDM43266 + ETH	1.84 ± 0.01	2.76 ± 0.05	

These results provide evidence on the significance of using pβCyD NPs instead of the natural βCyD to enhance the solubility of both ETH and the BDM43266. As to the competition studies of ETH and BDM43266 in the pβCyD NPs figures 3.8 c-d show the phase solubility diagrams of ETH loaded in pβCyD NPs before and after BDM43266 (Figure 3.8c, green and violet regression lines, respectively) and BDM43266 loaded before and after ETH (Figure 3.8d, red and violet lines, respectively). Binding constants are summarised in Table 3.2. The presence of a second drug in pβCyD NPs does not cause a significant change in the phase solubility profile of either ETH or BDM43266. These results give strong evidence that there is no competition for βCyD cavities and none of the components is displaced by the other which highlights the interest of using pβCyD NPs to co-encapsulate high amounts of both drugs.

3.4 Spectroscopic study of contemporary ETH and BDM43266 loading in pβCyD NPs

In order to confirm the simultaneous binding of ETH and BDM43266 to pβCyD NPs, we have used complementary spectroscopic techniques. A competition study was performed preparing BDM43266/pβCyD NPs mixture with and without ETH. We first evaluated the BDM43266//pβCyD mixtures and then we introduced ETH at a fixed concentration of 50

μM. Figure 3.9a shows the absorption spectra of all mixtures. Subtracting the spectra of pβCyD NPs or BDM43266/pβCyD NPs we obtained spectra of both compounds similar to those obtained for complexation with a single component. The fluorescence spectra in Figure 3.9b exhibit maxima at 351 nm corresponding to that of complexed BDM43266 and a trivial intensity increase with increasing BDM43266 concentration. Addition of ETH causes no change in the fluorescence maximum at 351 nm confirming that BDM43266 is not displaced from the polymer (Figure 3.9c). When comparing the intensity of the fluorescence signal with and without ETH we observe decreased intensity in the former case that may be due to the inner filter effects exerted by ETH with absorption overlapping that of the booster. Figure 3.9d shows the induced CD spectra of ETH with different amounts of BDM43266 in the polymer.
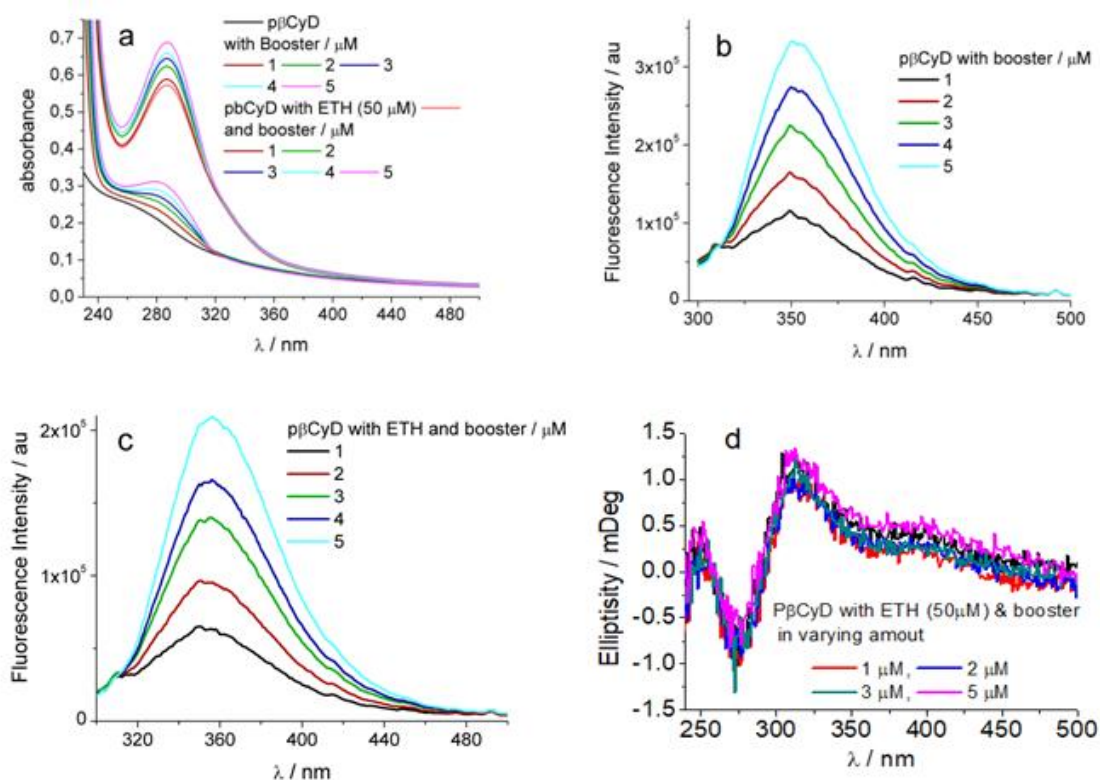
Figure 3.9 (a) Absorption spectra of 5×10^{-6} M BDM43266 solutions with pβCyD NPs (12 mg/ml) in water, and the same solutions with 5×10^{-5} M ETH, d = 1.0 cm. Note all samples contain 1% v/v DMSO to solubilise BDM43266 and ETH; **(b)** Fluorescence spectra of 5×10^{-6} M BDM43266 solutions with pβCyD NPs (12 mg/ml) and **(c)** 5×10^{-5} M ETH in water, d = 1.0 cm; λ_{exc} = 280 nm; **(d)** CD spectra of 5×10^{-5} M ETH solutions in the presence of pCyD NPs (12mg/ml) and 5×10^{-6} M booster, d = 2.0 cm.

The CD signal in the 320 and 280 nm range is similar in shape and intensity to that of the ETH/pβCyD NPs system[6] so the presence of BDM43266 does not induce any significant change in CD spectrum indicating that ETH occupies likely more than one type of complexation site, inside the βCyD cavity and microdomains in the pβCyD NPs as we

hypothesised for the ETH/ pβCyD NPs system in chapter 2. Overall these observations confirm that ETH and booster are not competing for the complexation sites in the pβCyD NPs although they are both included within the pβCyD NPs in line with the phase solubility experiments. We concluded this part of the study with an investigation of the particle size. 25 mg/ml pβCyD solutions were used for the DLS study of ETH loaded and unloaded nanoparticles (Table 3.3). Polymer solution was used to dissolve ETH and BDM43266 films.

We measured a particle diameter similar for the ETH loaded and unloaded NP. When booster was loaded on the same NP (ETH-pβCyD), size increased up to 46 nm, which indicate the loading of two molecules has a significant effect on the particle diameter. Table 3.3 reports the average zeta potential values was for pβCyD alone, for ETH/ pβCyD, and for ETH/ BDM43266/pβCyD. Z-potential values fall in a range typical for stable NPs and likely the negative surface charge assists to maintain the stability of self assembled nanoparticles avoiding aggregation due to electrostatic repulsion.

Table 3.3 Average particle and zeta potential of pβCyD, ETH/pβCyD, and ETH/ BDM43266/pβCyD

Sample	Average particle size (nm)	Average Zeta Potential (mV)
pβCyD	29	-10
PβCyD/ETH	27	-13
PβCyD/ BDM43266	46	-11

3.5 pβCyD NPs containing ETH/BDM43266 for microspayer application

We have studied the suitability for pulmonary administration of co-encapsuled ETH and BDM43266 inside the pβCyDs prepared without the need for organic solvents. Nebulisation is one of most promising strategies to deliver antibiotics or other drugs in lung tissue. It directly deposits the drug in the form of powder or solution in the lung allowing easily to achieve the effective drug concentration killing the bacteria with reduced side effects.[7] It is not permissible to use organic solvent based systems to deliver drugs by means of microsprayer which causes severe damage to lung tissue. We have examined the suitability of drug loaded pβCyD NPs nebulised systems to deliver the formulation to the lungs by using MicroSprayer[TM]. The most challenging task was the passing of pβCyD NPs formulation through the sub-miniaturised atomizer of the Microsprayer without altering the physical properties of the pβCyD NPs dispersion. In the

first step, the formulation viscosity with and without drug has been evaluated. pβCyD NPs at 150 mg/ml empty and loaded with ETH have a low viscosity of 3.6 cP and 4.0 cP, respectively, so loading of ETH in pβCyD NPs at its maximum amount does not affect the viscosity of the NP dispersions. Furthermore, empty pβCyD NPs and pβCyD NPs loaded with ETH/BDM43266 combination were sterilised by filtration though a 0.22mm filter. After filtration, possible loss in NPs and both drugs was evaluated.

Table 3.4 Recovery of pβCyD NPs ETH and BDM43266 after filtration and after passing the formulations through Microsprayer. Data were obtained from the average ±SD of three different experiments.

	After filtration(wt %)*			After Microsprayer®(wt %)		
Formulations	pβCyD NPs	ETH	BDM43266	pβCyD NPs	ETH	BDM43266
Plain pβCyD	103 ± 6.1	-	-	101 ± 5.0	-	-
pβCyD ETH/ BDM43266	101±6.2	101 ± 2.6	99 ± 3.0	99 ± 4.0	95 ± 3.1	94 ± 2.0

*Passed through a 0.22 μm filter.

A complete recovery of loaded NPs after filtration without loss of both drugs was recorded. Finally, empty or loaded NPs were passed through a MicroSprayer[TM] repeatedly. Similarly, the formulations were totally recovered (101±5.0 wt%) and each nebulised dose delivered a constant amount of both ETH and BDM43266 (Table 3.4) validating the possibility to use the formulations for pulmonary administration by using a MicroSprayer.

3.6 Molecular modelling studies of the βCyD complexes

To gain inside in the binding process of ETH and BDM43266 with βCyD cavities molecular modelling studies were performed. The relative stabilities of the inclusion complexes of ETH and BDM43266 with βCyD with reference to energies, geometrical parameters including fluctuations of the reciprocal distances, and changes in dimensions along MD trajectories were analysed.[8] In the starting geometries in Figure 3.10a-b where the guest molecule at the beginning was out of the βCyD cavity near peripheral hydroxyl moieties, the hydrophobic guest molecule in very few picoseconds moved the molecular section with the -CH3 terminal group into the cavity. All trajectories ultimately become identical to those with initial arrangements in Figure 3.10c-d.
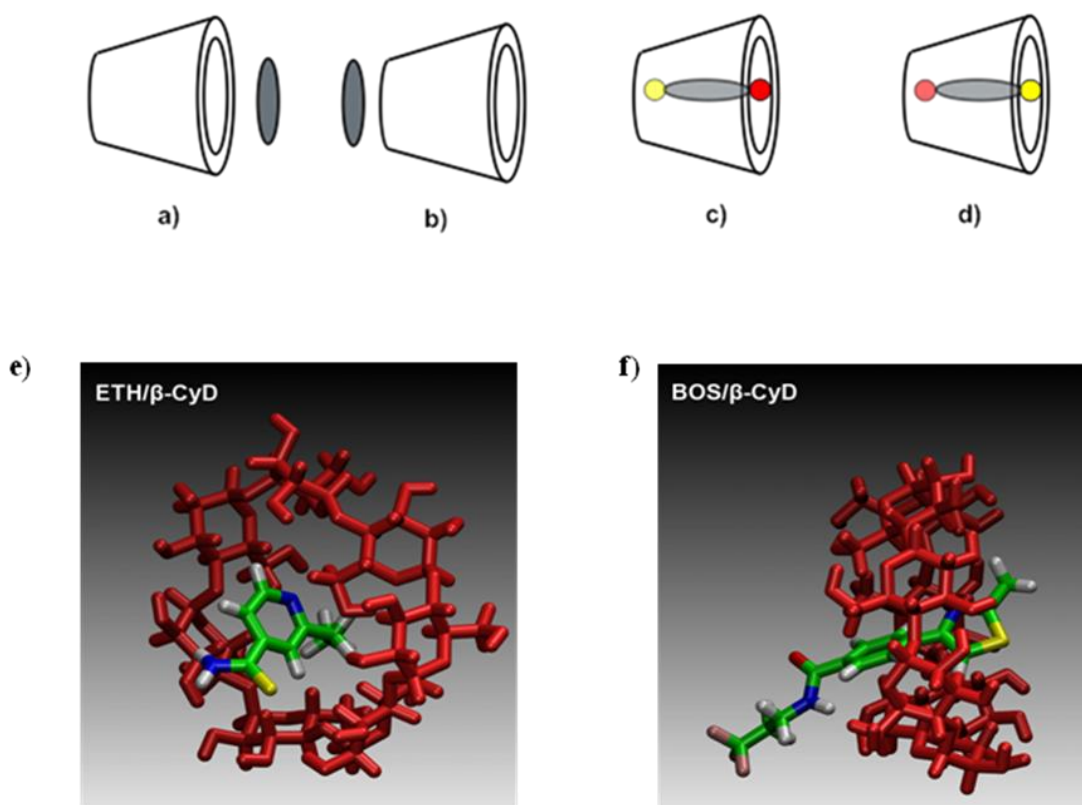
Figure 3.10 (**a–d**) Initial geometries for MD studies. Different initial molecular arrangements were prepared, where ETH and BDM43266 are placed outside the βCyD ring, either at the primary or (**a**) Secondary -OH side and (**b**) inside the βCyD ring with the -CH3/-CF3 terminal groups facing alternatively the primary or (**c**) The secondary hydroxyls rims (**d**); (**e–f**). Computed geometries of ETH/βCyD (**e**) and BDM43266/βCyD (**f**) at the minimum in total energy for the initial molecular arrangements in Figure 3.10c.

When we visualised the trajectories after equilibration step at given temperature, pressure and number of molecules of the MD runs, the solvated 1:1 inclusion complexes are fairly stable, displaying rather persistent reciprocal arrangements. Figure 3.10e-f displayed the inclusion complex geometries for ETH and BDM43266, in the absence of water molecules at the lowest total energy frame along trajectories starting from arrangement c in Figure 3.10. Table 3.5 reports the average values of the total energies which represent the the βCyD/guest interaction energies and the radii of gyration. Once the equilibration is achieved, energies and geometrical parameters shows a small standard deviation from their average values (<0.5% for the total energy). Complexes stability along the trajectories was confirmed by their negative interaction energies and small standard deviations in the values of radii of gyration. Lower interaction energies confirm that BDM43266 inclusion is more stable in comparison to ETH inclusion complex. Comparison of the different trajectories for the same complex is less precise by considering the standard deviations of interaction energies. The degree of interpenetration of the two components can be

determined by using the values of r gyr of the complex, which is an equivent to the corresponding r gyr of the βCyD molecule.

Table 3.5 Values of total energies, interaction energies between βCyD and the guest molecule, radii of gyration. Average values with the corresponding standard deviations are computed for the MD runs listed in column 1.

Complex	Energy Average [kcal mol^{-1}]	Interaction Energy Average [kcal mol^{-1}]	r_{gyr} (complex) Average [Å]	r_{gyr} (βCyD) Average [Å]	r_{gyr} guest Average [Å]
βCyD/ETH (Fig.3.10a)	-46631 ± 139	-21.9 ± 4.9	5.87 ± 0.08	6.07 ± 0.09	2.66 ± 0.04
βCyD/ETH (Fig.3.10b)	-48214 ± 145	-26.3 ± 3.9	5.94 ± 0.05	6.23 ± 0.05	2.99 ± 0.04
βCyD/ETH (Fig.3.10c)	-45439 ± 137	-23.0 ± 5.1	5.85 ± 0.09	6.08 ± 0.07	2.64 ± 0.04
βCyD/ETH (Fig.3.10d)	-45193 ± 137	-25.2 ± 4.4	5.82 ± 0.07	6.11 ± 0.08	2.65 ± 0.04
βCyD/BDM43266 (Fig.3.10a)	-49144 ± 143	-29.2 ± 4.1	6.08 ± 0.15	6.13 ± 0.05	4.85 ± 0.17
βCyD/BDM43266 (Fig.3.10b)	-51030 ± 145	-32.0 ± 5.0	6.00 ± 0.14	6.12 ± 0.06	4.82 ± 0.20
βCyD/BDM43266 (Fig.3.10c)	-49715 ± 143	-29.6 ± 4.2	6.06 ± 0.15	6.12 ± 0.06	4.82 ± 0.19
βCyD/BDM43266 (Fig.3.10d)	-49991 ± 146	-28.0 ± 4.6	5.99 ± 0.14	6.11 ± 0.05	4.82 ± 0.20

Further understanding was obtained by studying the H-bond dynamics between βCyD and guests and between guests and water molecules. Trajectory analysis demonstrated that when the -CH3 group of ETH approaches to the secondary hydroxyl side of βCyD (Figure 3.10a-c) the ETH S-atom forms the largest number of H-bonds with hydroxyls of βCyD followed by the N atom in the ring. Whereas, when the -CH3 group is at the primary hydroxyl side, then -NH2 group provides the largest number of H bonds with βCyD, while the sum of contributions by other acceptors (S and N) are significantly lower. When we compared the H bonds between ETH and water, a different scenario was observed. In this case, -NH2 group provides the largest number of H-bonds which is about twice the number formed by the S atom and the N atom in the pyridine structure. While in case of BDM43266 complexes, H-bonds between host and guest involved predominantly an O atom in the BDM43266 molecule and contributions by other atoms seems negligible. We have also recoreded a similar tendency for H-bonds between BDM43266 and water, where BDM43266 O atom still plays the major role, although the contributions by the -NH group and the Fluorine atoms was slightly higher. Globally,the number of H-bonds between

solvent and guest considerably exceeds the H-bonds formed between guest and βCyD host. Therefore, complex stability might be compromised due to the the competition between solvent and host molecule to form H-bonds with the guest molecules. However, additional stabilising factor are provided by water molecules forming H bond bridges between βCyD and guest.

As discussed, induced CD signal was detected only for ETH inclusion in βCyD, whereas this feature was absent in the case of BDM43266/βCyD spectra. As we know inclusion of achiral molecules into the chiral cavity of βCyD can result in formation of chiral complexes, MD trajectories have been extensively studied to gain information about constrained conformations of the guest moiety, as a possible source of the induced CD signal. In ETH, rotation around the torsion angle involving the -NH2 group and the pyridine ring demonstrate the presence of two conformers (cis and trans) with respect to the CH3 terminal moiety. Figure 3.11a represent the values of this torsion angle for the trajectory corresponding to arrangements in Figure 3.10b. These data are in line with those obtained for most of the trajectories.

The torsion angle shows a small oscillation around its average value, but the original *cis* conformation was consistent along the whole trajectory. A different behaviour is reported in Figure 3.11b. The displacements of the ETH molecule in the βCyD cavity at significant extent led to a change in conformation (from cis to trans). However, the new conformation obtained was consistent along the remaining part of the trajectory. Thus, we can conclude that interactions of ETH with βCyD can somewhat hinder free rotation around the measured torsion angle, considerably fixing the relative proportion of the two stereoisomers. In these scenario, the induced CD may be obtained due to interactions of diastereoisomers with the stereogenic centers of βCyD.[9,10] Scrutiny of changes in the BDM43266 torsion angles is more problematic as cis/trans interconversions depend on three torsion angles at least. The torsion angles values along the trajectories have been estimated, but relative correlations to well define cis/trans conformers were not discovered. For an example Figure 3.11c display values of the torsion angle between the -NH group and the N atom in the thiazole ring at the opposite molecule side. The torsion angle values which could conform to a cis/trans conformer with the -CH3 terminal group, show a random trend along the trajectory. Thus, we can conclude that complexes of BDM43266 with βCyD do not exhibit defined populations of diastereomers as in the case of ETH.
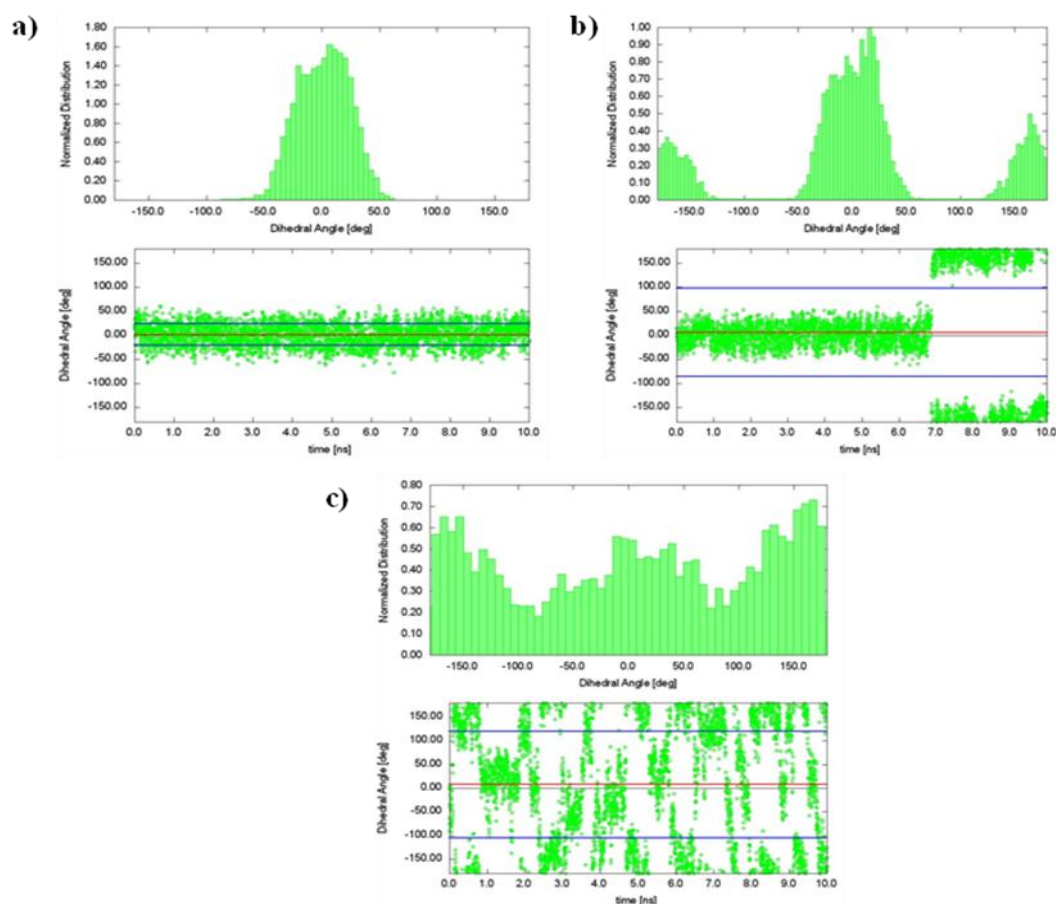
Figure 3.11 (a). (top) Normalised Distribution of the ETH torsion angle between the -NH2 group and the pyridine ring for the inclusion complex in Figure 3.10b. (Bottom) Values of the ETH torsion angle vs. time. The red line corresponds to the average value and the blue lines to ± 1σ (standard deviation). (**b**) (top) Normalised Distribution of the ETH torsion angle between the -NH2 group and the pyridine ring for the inclusion complex in Figure 3.10d. (Bottom) Values of the ETH torsion angle vs. time. The red line corresponds to the average value and the blue lines to ± 1σ (standard deviation); (**c**) (top) Normalised Distribution of the BDM43266 torsion angle between the –NH group and the thiazole ring for the inclusion complex in Figure 3.10a. (Bottom) Values of the BDM43266 torsion angle *vs.* time. The red line corresponds to the average value and the blue lines to ± 1σ (standard deviation).

3.7 Conclusions

We studied the potential of pβCyD NPs for the co-encapsulation of two molecules, ETH and booster BDM43266 in pβCyD NPs. We were able to obtain ETH/Booster pβCyD formulations in pure water without the need of using organic solvents. The ETH and BDM43266 molecules do not compete for the binding sites in the polymer confining large number of sites in a small volume. We also obtained good binding constants for the other four booster. The pβCyD NPs formulation of ETH and BDM43266 holds promises for pulmonary administration to treat infections of MDR-strains of M. tuberculosis in the near future.

3.8 References

1. A. R. Baulard, J. C. Betts, J. Engohang-Ndong, S. Quan, R. A. McAdam, P. J. Brennan, C. Locht and G. S. Besra, *J. Biol. Chem.*, **2000**, 275, 28326-28331.
2. N. Willand, B. Dirié, X. Carette, P. Bifani, A. Singhal, M. Desroses, F. Leroux, E. Willery, V. Mathys and R. Déprez-Poulain, *Nat. Med.*, **2009**, 15, 537-544.
3. M. Flipo, M. Desroses, N. Lecat-Guillet, B. Dirié, X. Carette, F. Leroux, C. Piveteau, F. Demirkaya, Z. Lens and P. Rucktooa, *J. Med. Chem.*, **2011**, 54, 2994-3010.
4. B. Villemagne, M. Flipo, N. Blondiaux, C. l. Crauste, S. Malaquin, F. Leroux, C. Piveteau, V. Villeret, P. Brodin and B. O. Villoutreix, *J. Med. Chem.*, **2014**, 57, 4876-4888.
5. T. Loftsson and M. E. Brewster, *J. Pharm. Sci.*, **1996**, 85, 1017-1025.
6. J. Wankar, G. Salzano, E. Pancani, G. Benkovics, M. Malanga, F. Manoli, R. Gref, E. Fenyvesi and I. Manet, *Int. J. Pharm.*, **2017**, 531, 568-576.
7. R. Pandey and G. Khuller, *J. Antimicrob. Chemother.*, **2005**, 55, 430-435.
8. W. Humphrey, A. Dalke and K. Schulten, *J. Mol. Graph.*, **1996**, 14, 33-38.
9. S. Allenmark, *Chirality*, **2003**, 15, 409-422.
10. F. Zsila, *Pharmaceutical Sciences Encyclopedia*, **2010**.

Chapter 4

Clofazimine loading in SBE-βCyD carrier systems

4.1 Introduction

CLZ is a riminophenazine antibiotic presenting as a red powder and is a well known antileprosy drug that has been in use for many decades (Scheme 4.1).[1] CLZ has a broad antibiotic spectrum with inhibitory activity against many Gram-positive bacteria including mycobacteria, staphylococci, streptococci, enterococci, and listeria.[2] The exact mechanism of action of CLZ is not yet known and several mechanisms have been proposed relying on its lipophilic character as well as its redox potential of -0.18 V at pH 7. The suggested ways of action are related to redox cycling processes as well as membrane-disruptive properties of the cationic amphiphilic molecule. As to the former, CLZ competes for electrons with menaquinone, a substrate of type 2 NADH:quinine oxidoreductase, a protein triggering initial events in the bacterial respiratory chain. The reduced CLZ undergoes spontaneous oxidation producing thus ROS compromising bacterial survival. The second way of CLZ action refers to cell membrane disruption reported for *Staphylococcus aureus* involving inhibition of bacterial K^+ active transporter proteins followed by ATP depletion and growth inhibition.[2, 3] This quite unique combination of several mechanisms has prevented up to now the development of resistance against CLZ.
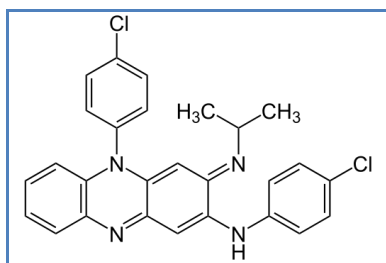
Scheme 4.1 Clofazimine

Emergence and spreading of MDR resistant bacterial strains in the last few decades has caused a renewal of interest in CLZ for the treatment of some MDR and drug-sensitive bacterial strains including *M. tuberculosis*.[2] Nevertheless upgrade of CLZ to first-line drug for the treatment of infectious diseases different from leprosy is hampered by unfavourable pharmacokinetics. Indeed, CLZ is a highly lipophilic molecule having logP 7.5 which makes CLZ practically insoluble in water and favours accumulation in fat tissues. As high doses are required, its use is associated with several severe side effects like nausea, vomiting, diarrhea and skin discoloration.[4] In this frame we envisage encapsulation of CLZ in nanocarrier systems to improve its bioavailability. Some approaches based on nanotechnology to solve CLZ administration issues have already been reported. CLZ leucine mixed inhalable dry powder microparticles and native CLZ were evaluated for activity against *Mycobacterium tuberculosis* in human monocyte-derived

macrophage cultures and in infected mice. Both formulations resulted in 99% killing of bacteria at 2.5 μg/ml *in vitro*. In infected mice, 480 μg and 720 μg CLZ loaded dry powder microparticles inhaled twice per week over 4 weeks reduced numbers of CFU in the lung by as much as $\log_{10}$ 2.6 while 500 μg oral CLZ achieved only a $\log_{10}$ 0.7 reduction.[5] In another study, CLZ encapsulation in nanoporous silica particles was investigated to improve the drug solubility in gastric fluid, the drug intestinal permeability, and the stability on storage for more than 6 months in amorphous form.[6]

For our study, we focused on negatively charged CyD-based carriers as CLZ is present in cationic form at physiological pH. We used sulfobutylether (SBE) derivatives of βCyD and epichlorohydrin crosslinked SBE-βCyD polymers with and without rhodamine (Rho) label. We have investigated the interaction of CLZ with the CyD carriers, the encapsulation efficacy of the various carriers, the efficacy against staphylococci, in particular drug sensitive and MDR resistant clinical isolates of *S. epidermidis* and the cytotoxicity of CLZ loaded SBE-βCyD carrier systems on a VERO cell line model.

4.2 Experimental part

Materials:

The epichlorohydrin crosslinked sulfobutylether βCyD polymer (estimated CyD content, 50-70% w/w), labeled and not with Rho (Rho labeled SBE-βCyD content of 1 %), sulfobutylether βCyD, Rho labeled sulfobutylether-βCyD sodium salt (DS-6.5 for SBE) were obtained from Cyclolab, Hungary. Clofazimine was purchased from Santa Cruz Biotechnology (Heidelberg, Germany). Tween 20 was purchesed from Sigma Aldrich.

Preparation of titration solutions:

CLZ was dissolved in Methanol or DMSO as it is insoluble in water. Aqueous carrier solutions of varying concentrations were prepared and added to CLZ aliquots previously dissolved in MEOH to obtain 6 and 60 μM CLZ mixtures with a very low final alcohol amount of 1 or 5% v/v. To determine aqueous solubility of CLZ using the carriers, weighed amounts of solid CLZ were kept mixing with aqueous carrier solutions of various concentrations to allow dissolution of drug in pure aqueous solution. All solutions were protected from light. Excess amount of undissolved drug was eliminated by centrifugation. Absorption and circular dichroism spectra were recorded to monitor the mixtures.

4.3 Spectroscopic determination of standard solubility curve

CLZ is a riminophenazine and presents as a red solid powder. The absorption spectra of CLZ in various means are shown in Figure 4.1a-b. The absorption spectra in EtOH and DMSO are quite similar peaking at 280 nm and 450 nm. Addition of water or PBS to the solvent causes a strong shift to the red. The likely reason for this is the protonation of CLZ considering the reported pKa value of 8.51 of the isopropyl amine group.[4] Among the solvents explored only in DMSO the fluorescence of CLZ could be observed, presenting a broad band with two peaks at 540 and 580 nm, see Figure 4.1c. CLZ fluorescence excitation spectra were also recorded and are very similar to the absorption spectra (Figure 4.1d). In DMSO, CLZ has a very short fluorescence lifetime of 0.11 ns, below the instrumental time limit, and a lifetime of 2.35 ns with fractional intensity of 80 and 20 %, respectively.
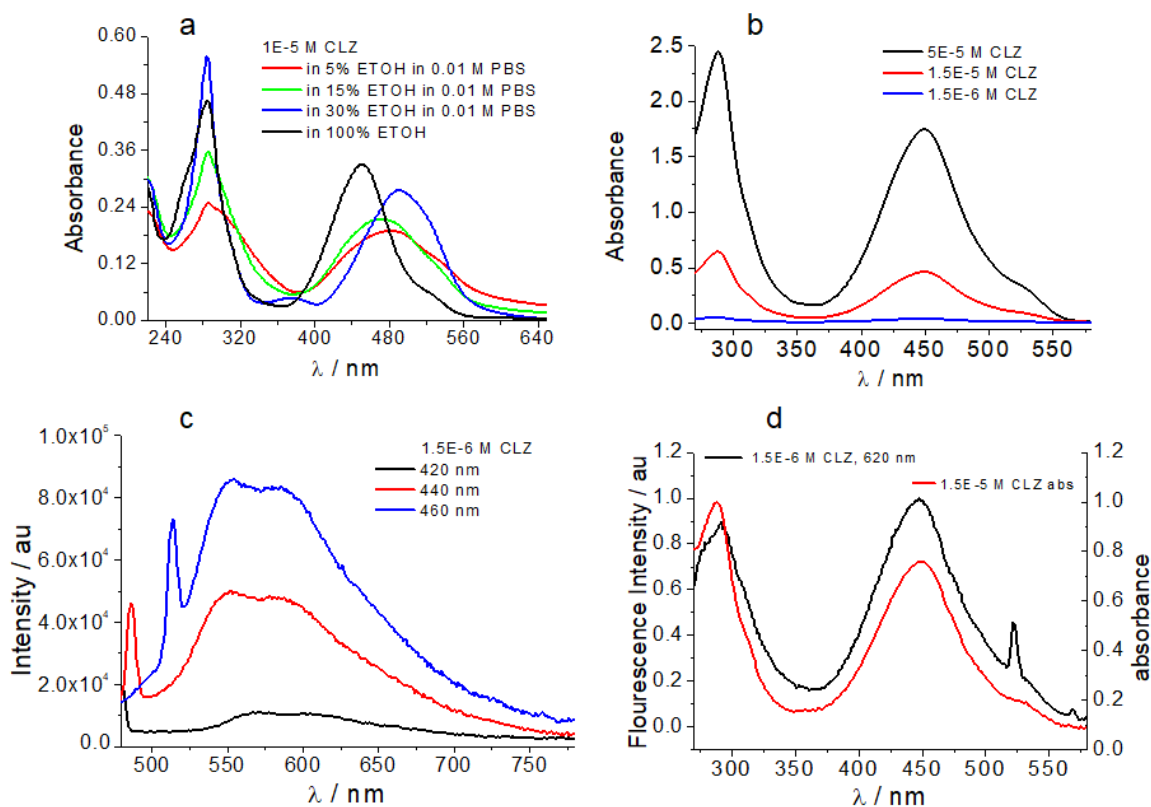
Figure 4.1 (**a**) 1×10^{-5} M CLZ absorption spectra in pure EtOH and EtOH/water mixtures; (**b**) CLZ absorption spectra in DMSO (**c**) Fluorescence emission spectra of 1.5×10^{-6} M CLZ in DMSO, excitation wavelengths are 420, 440 and 460 nm; (**d**) Fluorescence excitation spectrum (black) registered at 620 nm of 1.5×10^{-6} M CLZ in DMSO, d=1cm compared with the absorption spectrum (red) of a more concentrated solution.

Next, we prepared a concentrated solution of CLZ in MeOH. The CLZ standard solubility curve was prepared using as diluting solvent 0.01M Na^+ PBS (pH 7.4) with 1.5% w/v Tween 20 surfactant micelles. CLZ was adequately diluted with the PBS Tween mixtures

keeping the final MeOH amount below 1% v/v. The UV VIS absorption spectra are shown in Figure 4.2 and show two main peaks at 286 and 492 nm with a molar absorption coefficient of 31600 $M^{-1}cm^{-1}$ at the latter wavelength. Absorption at 492 nm was plotted against CLZ concentration. This standard curve was used to calculate subsequently the loading of CLZ in SBE-βCyD carrier systems.
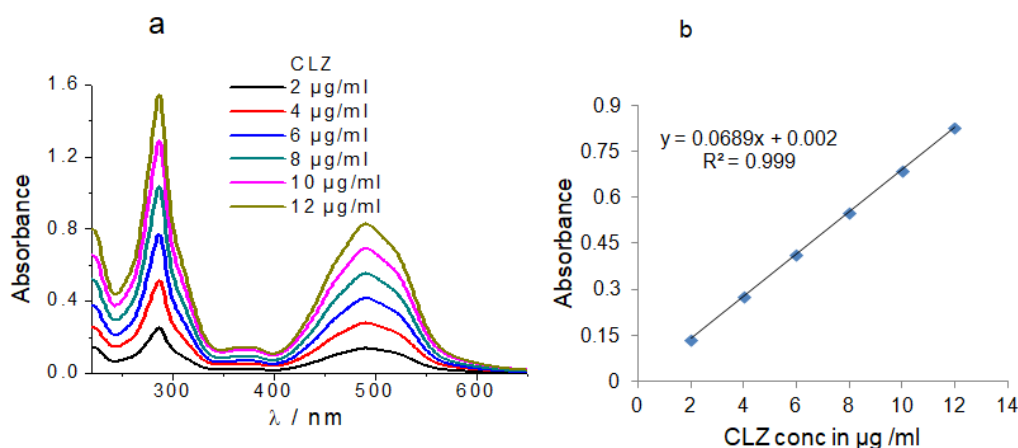
Figure 4.2 (**a**) Absorption spectra 2-12 μg/ml CLZ in 0.01M PBS with 1.5% w/v Tween 20 and (**b**) Standard solubility curve plotting absorbance at 492 nm vs CLZ amount, 2-12 μg/ml CLZ in 0.01M PBS with 1.5% w/v Tween 20; d=1cm.

4.4 CLZ loading in SBE-βCyD carrier systems

As CLZ is a hydrophobic molecule with negligible aqueous solubility, we performed a test to determine solubility with known amounts of SBE-βCyD carrier systems. We have used aqueous solutions of 50 mg/ml and 100 mg/ml of each carrier system with an excess amount of solid CLZ to prepare the aqueous colloidal dispersions.
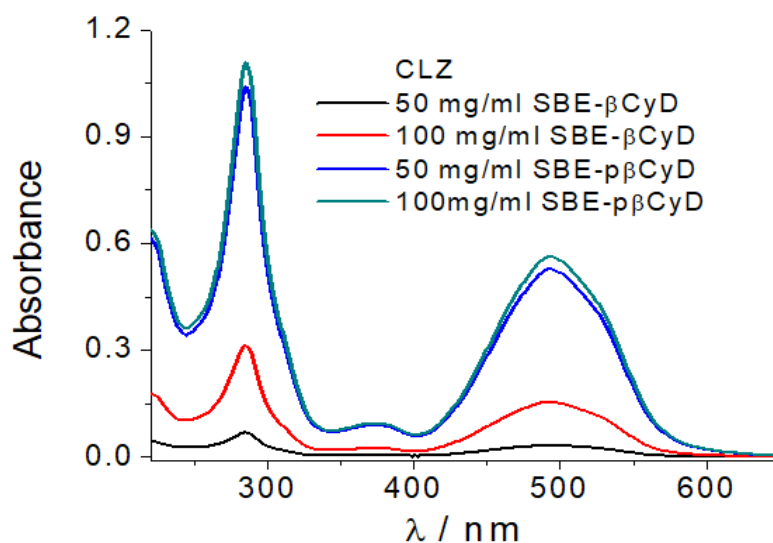
Figure 4.3 Absorption spectra of diluted supernatant of solid CLZ dissolved with SBE-pβCyD and SBE-βCyD in water; d = 1cm.

50

This dispersion was kept stirring for more than 72 hours at room temperature in the dark. Absorption of the supernatant (Figure 4.3) was used to calculate the maximum amount of CLZ with SBE-βCyD polymer and monomer. As evidenced by the data in table 4.1 SBE-pβCyD solubilise the highest extent of CLZ in aqueous media corresponding to 0.25 mg/ml. We obtained a first proof of CLZ loading in SBE-βCyD carriers avoiding the use of organic solvents.

Table 4.1 Amount of solid CLZ dissolved by SBE-pβCyD and SBE-βCyD carrier systems calculated from the absorbance at 492 nm of diluted supernatant.

Sample	Abs at 492 nm	CLZ in mg/ml
50mg/ml SBE-pβCyD +CLZ	0.527	0.12 mg
100mg/ml SBE-pβCyD +CLZ	0.563	0.25 mg
50mg/ml SBE-βCyD +CLZ	0.033	0.007 mg
100 mg /ml SBE-βCyD+CLZ	0.155	0.035 mg

4.5 Spectroscopic study of CLZ interaction with the SBE-βCyD-based carriers
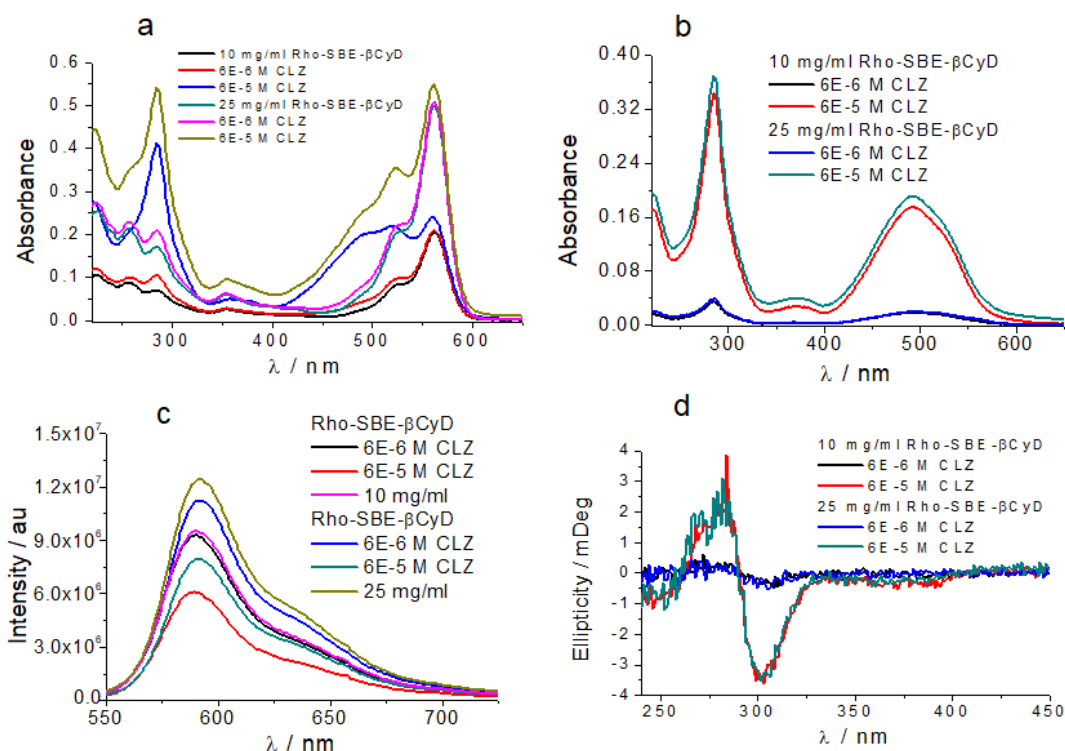
Figure 4.4 (a) Absorption spectra of 6×10^{-6} M and 6×10^{-5} M CLZ with Rho-SBE-βCyD (10 and 25 mg/ml) in water, d = 0.1 cm, (**b**) Absorption spectra of 6×10^{-6} M and 6×10^{-5} M CLZ with Rho-SBE-βCyD (10 and 25 mg/ml) after subtracting Rho-SBE-βCyD reference solution, (**c**) Fluorescence spectra of 6×10^{-6} M and 6×10^{-5} M CLZ with Rho-SBE-βCyD (10 and 25 mg/ml), $\lambda_{exc} = 530$ nm and (**d**) CD spectra of 6×10^{-6} M and 6×10^{-5} M CLZ with Rho-SBE-βCyD (10 and 25 mg/ml), d = 0.5 cm.

51

Interaction of CLZ with the various carriers has been studied with various optical spectroscopic techniques to get insight in the binding process. Absorption spectra of CLZ films dissolved by SBE-βCyD carrier solutions in water are shown in Figures 4.4 and 4.5 for the Rho-labeled ones and Figures 4.6 and 4.7 for the unlabeled. CLZ absorption falls in the ultraviolet region with a peak at 285 nm and a second band in the visible region which is partially covered by the rhodamine peak at 570 nm present in the complex mixture. Subtracting the carrier absorption spectra, we obtain the spectra typical of CLZ in an aqueous environment and very similar to the ones obtained in the PBS/Tween 20 mixture. Indeed we can observe a maximum at 492 nm, in the presence of the carrier compared to 490 nm in the PBS/Tween mixture. CLZ is likely present in its protonated form. The same features are observed for the unlabeled carriers loading CLZ, see Figures 4.6 and 4.7. Interestingly, filtration through a filter with 0.22 μm pores is not reducing the amount of drug and carrier and this feature has been exploited for the sterilisation of the mixtures for the biological tests.
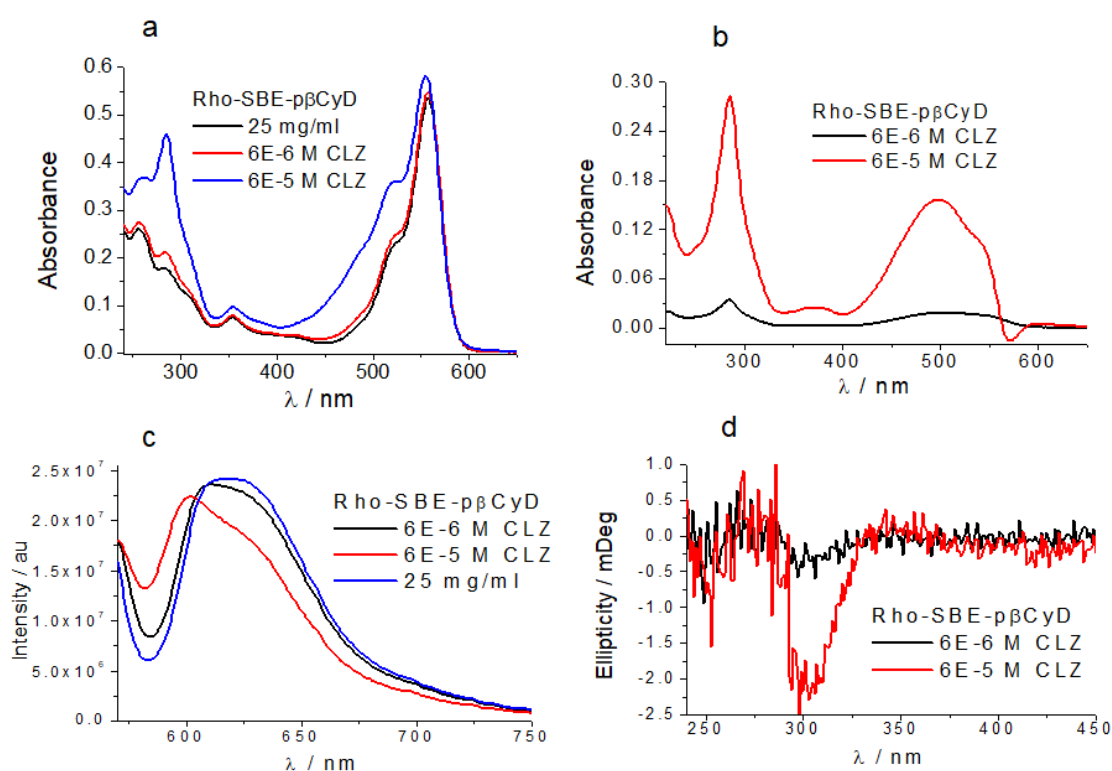
Figure 4.5 (a) Absorption spectra of 6×10^{-6} M and 6×10^{-5} M CLZ in Rho-SBE-pβCyD (10 and 25 mg/ml) in water, d = 0.1 cm (**b**) Absorption spectra of 6×10^{-6} M and 6×10^{-5} M CLZ in Rho-SBE-pβCyD (10 and 25 mg/ml) after subtracting Rho-SBE-pβCyD reference solution, (**c**) Fluorescence spectra of 6×10^{-6} M and 6×10^{-5} M CLZ in Rho-SBE-pβCyD (10 and 25 mg/ml) and (**d**) CD spectra of 6×10^{-6} M and 6×10^{-5} M CLZ in Rho-SBE-pβCyD (10 and 25 mg/ml), d = 0.5 cm.

As to the fluorescence spectra of the mixtures, shown in Figure 4.4c and 4.5c, we did not observe a CLZ contribution to fluorescence while the rhodamine fluorescence is partially

quenched upon CLZ loading in the monomeric and polymeric carrier compared to free rhodamine labeled monomer and polymer. Reliable quantitative information on quenching cannot be obtained due to the high label absorbance. A biexponential decay has been observed at 610 nm for excitation at 465 nm that yields two lifetimes, shown in table 4.2, also in the absence of the drug. Likely the label experiences different environments attached to the carrier. The lifetimes are in line with other values found in the literature for Rho. Conservation of the Rho fluorescence upon drug complexation is particularly interesting for the further development of the drug carrier system.

Table 4.2 Parameters of biexponential fitting of fluorescence decay at 610 nm for excitation at 465 nm with and without CLZ.

Sample	τ_1/ns	τ_2/ns	f_1	f_2	χ^2
Rho-SBE-pβCyD/6 μM CLZ	1.43	3.48	0.31	0.69	0.98
Rho-SBE-pβCyD/60 μM CLZ	1.29	3.36	0.26	0.74	1.04
Rho-SBE-pβCyD	1.19	3.38	0.24	0.76	1.09

As CLZ is not chiral, it does not have an intrinsic CD signal but induced circular dichroism spectra were observed upon complexation with all SBE-βCyD carriers shown in Figures 4.4-4.7. CD spectra were characterised by a positive band at 280 nm and a negative band at 300 nm in correspondence of the most intense absorption band. In the visible region, we do not observe any induced signal. The UV signal may be due to inclusion of the chlorophenyl moieties in the βCyD cavity leaving the rest of the molecule exposed to the solvent. Dried films of CLZ dissolved with aqueous carrier solutions without organic solvent behave similarly from the spectroscopic point of view suggesting the small amount of organic solvent is not altering the CLZ binding features.
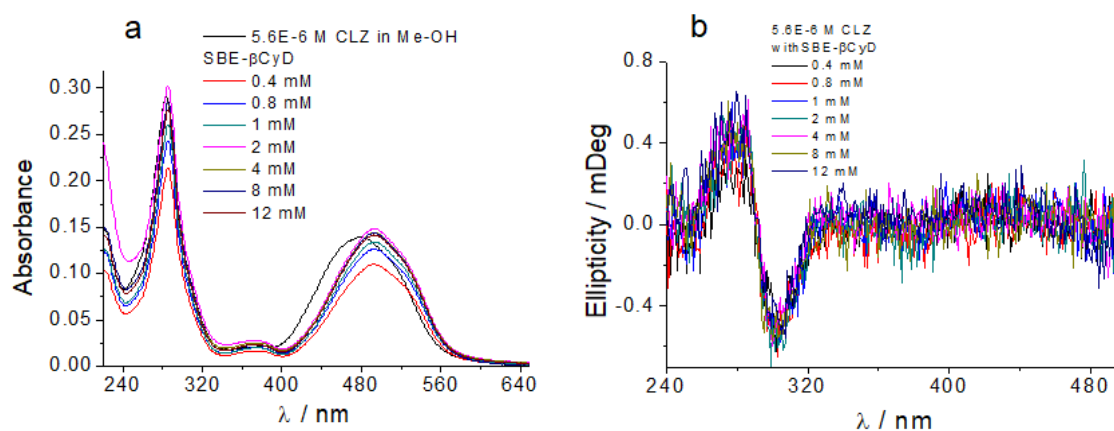
Figure 4.6 (a) Absorption spectra of 5.6×10^{-6} M CLZ with SBE-βCyD (0.4-12×10^{-3} M) in water with 1% MeOH and **(b)** CD spectra of 5.6×10^{-6} M CLZ with SBE-pCyD (0.4 - 12×10^{-3} M); d = 1cm.
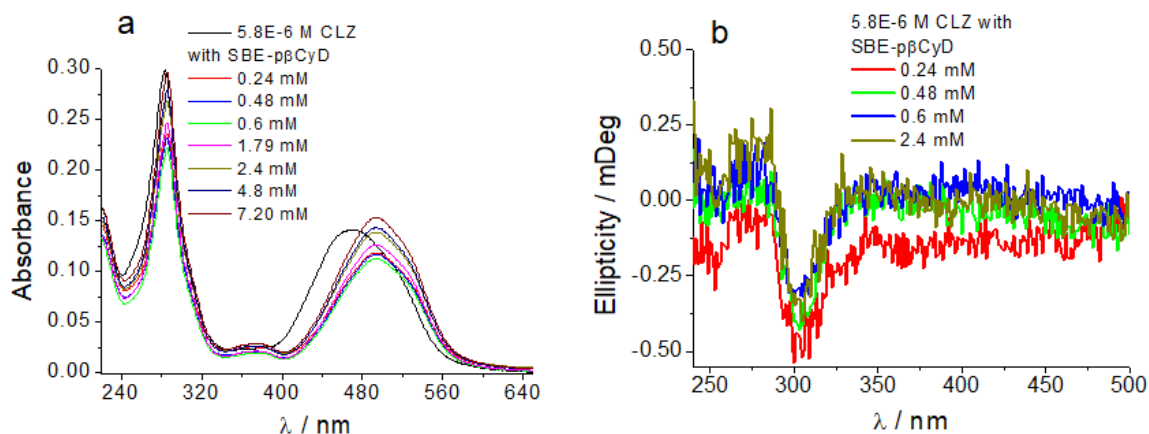
Figure 4.7 (**a**) Absorption spectra of 5.8×10^{-6} M CLZ with SBE-pβCyD ([SBE-βCyD] = $0.24-7.20 \times 10^{-3}$M) in water with 1 % MeOH and (**b**) CD spectra of 5.8×10^{-6} M CLZ with SBE-pβCyD ([SBE-βCyD]= $0.24-7.20 \times 10^{-3}$ M); d = 1cm.

4.6 AF4-MALS analysis of carriers loaded and not with CLZ

To further characterise the polymeric carriers the AF4-MALS technique was used.[7] After chromatographic separation (see chapter 6 for more information) online detection of the eluted species was performed with a UV/Vis spectrophotometer, a multi angle light scattering (MALS) detector and an Optilab T-rEX refractive index (RI) detector. The molar masses were determined from the RI and MALS signals using dn/dc values previously measured through calibration curves for each sample in milliQ water (data not shown). Figure 4.8a reports the fractogram obtained for the injection of SBE-pβCyD unloaded polymer. The fractogram shows one main band slightly retained (tR= 7 min). A molar mass of 5.287×10^4 Da was calculated. In addition, the r_g value obtained by the AF4-MALS fractionation indicates the polymer is fairly homogenous with a particle size of ca. 30.5 nm (PDI=1.021). In Figure 4.8a the 3D absorption spectrum (200-800 nm) of the eluted sample is reported. At the retention time of the polymer, only a signal at λ= 220 nm can be detected.
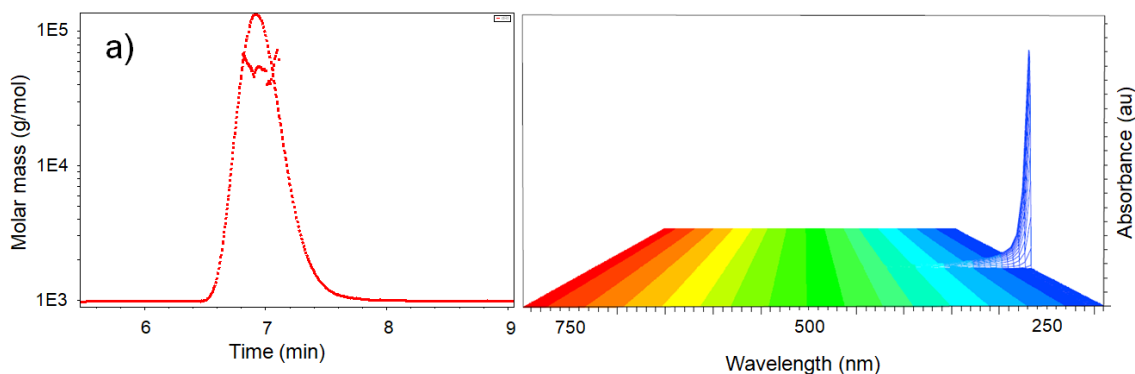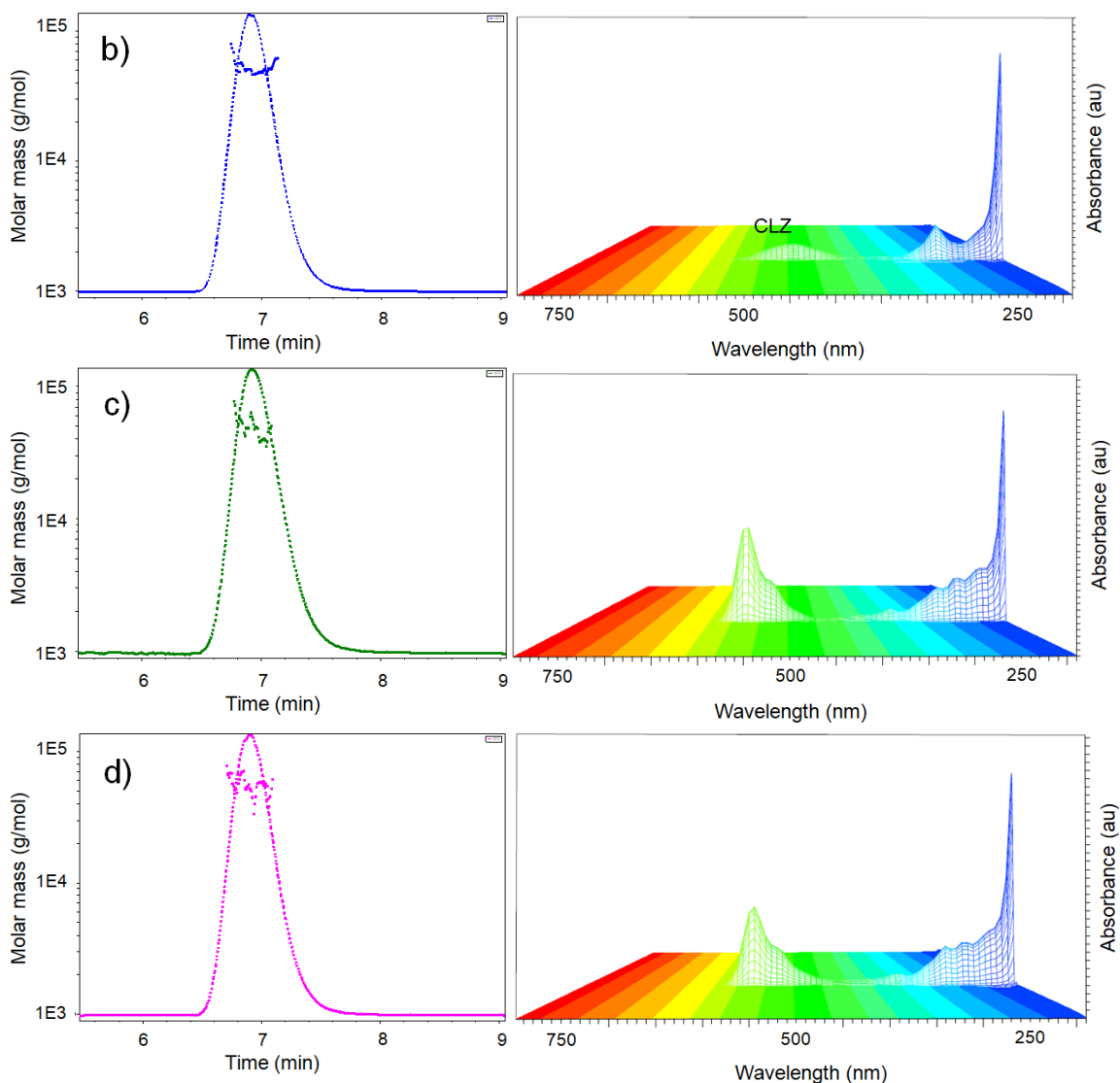
Figure 4.8 (**a**) Fractogram and 3D absorption spectra of SBE-pβCyD, (**b**) CLZ/SBE-pβCyD (**c**) Rho-SBE-pβCyD (**d**) CLZ/Rho-SBE-pβCyD.

The same analysis was performed on SBE-pβCyD loaded polymer (CLZ-SBE-βCyD) and the fractogram is reported in Figure 4.8b. The fractogram shows the same band at tR= 7 min, suggesting that the loaded polymer has a hydrodynamic radius similar to the unloaded sample. A molar mass of 5.096×10^4 Da and an r_g of ca. 22.3 nm (PDI=1.012) were obtained. In addition, in the absorption spectrum (Figure 4.8b) recorded at the polymer retention time, a signal at λ= 490 nm appears, confirming the presence of drug in the polymer sample. The calculated molar mass is similar for the two samples as expected. Both samples present the same retention time with a similar hydrodynamic radius, while the gyration radius for the loaded polymer is lower than the unloaded one. This can be explained by the drug presence inside the polymer resulting in a more compact sample (Figure 4.9a-b). The same decrease in the loaded polymer dimensions was observed from

DLS analysis shown in table 4.3. Figures 4.8c and 4.8d represent some AF4-MALS data for the Rho-labeled SBE-pβCyD polymer, unloaded (Rho-SBE-βCyD) and loaded (CLZ/Rho-SBE-βCyD). A molar mass of about ca. 5.3×10^4 Da was measured for both samples that have the same retention time. The absorption spectrum recorded at the polymer retention time shows the signal characteristic of rhodamine ($\lambda= 550$ nm) for both samples; while for the loaded polymer also a low signal due to the drug absorption can be observed. For the gyration radius we observed an opposite situation with respect to unlabeled polymer: the r_g value for the loaded one is higher (rms ca. 60 nm) than for the unloaded (rms ca. 50 nm).
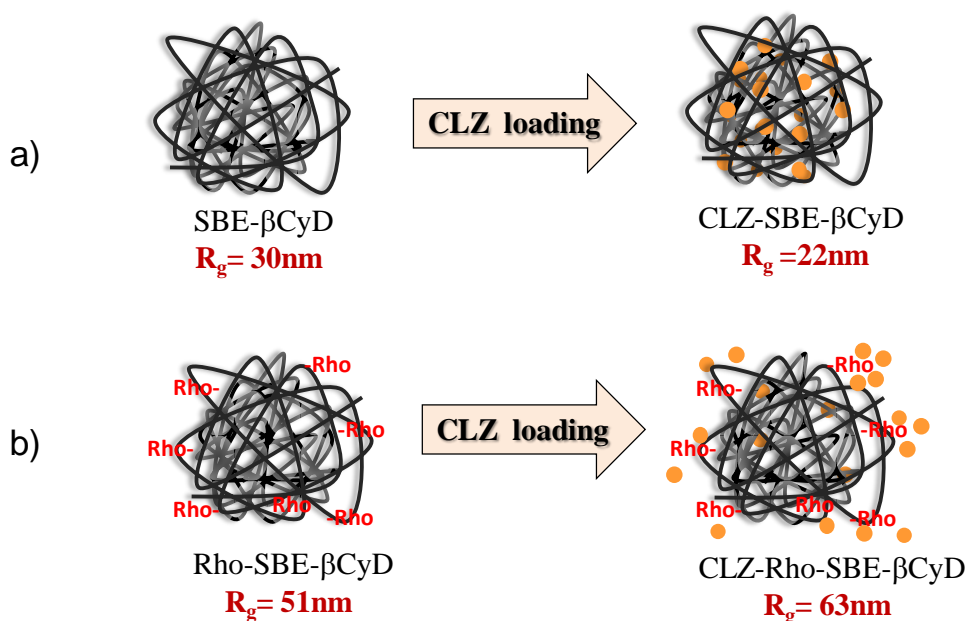
Figure 4.9 Cartoon representation of change in dimension for CLZ in (**a**) SBE-pβCyD and (**b**) Rho-SBE-pβCyD carriers systems

It is known that βCyD complexes Rho with a binding constant of 6E3 M^{-1}.[8] This behaviour can induce some polymer aggregation if Rho interacts with βCyDs unit from a second polymer. Further both drug and label carry a positive charge that may cause some electrostatic repulsion and increased gyration radius.

Table 4.3 DLS measurement of SBE-pβCyD with and without CLZ

Sample	Particle size (nm)	Polydispersity index
SBE-pβCyD	52	0.320
CLZ/SBE-pβCyD	42	0.307

4.7 Biological assays on the CLZ carrier systems

4.7.1 Determination of MIC values for reference bacterial strains

The antibacterial properties of the CLZ drug and of the CLZ/carrier systems were assayed at first on a set of reference bacterial strains including 3 Gram positive and 1 Gram negative (*E. coli*) bacteria. *E. faecalis* and *E. coli* proved to be resistant to CLZ drug also when encapsulated in the complex systems, at all tested concentrations. These results are in accordance with data from literature.[9]

Table 4.4 MIC values of the CLZ free drug and of the four samples against *S. epidermidis* ATCC reference strain.

	MIC$_{50}$ (95% CI) (µM)	MIC$_{90}$ (95% CI) (µM)
CLZ	0.092 (0.083-0.101)	0.121 (0.109-0.134)
CLZ/SBE-β-CyD Polymer	0.092 (0.078-0.107)	0.112 (0.098-0.129)
CLZ/Rho SBE-β-CyD Polymer	³0.25	³0.25
CLZ/Rho SBE-β-CyD Monomer	0.106 (0.090-0.125)	0.148 (0.122-0.179)
CLZ/SBE-β-CyD Monomer	0.079 (0.067-0.093)	0.105 (0.075-0.147)

CLZ drug and its preparation in the monomer carrier systems (with and without rhodamine label) inhibited *S. aureus* growth only at the highest concentration tested (0.5 µM) while all samples except CLZ/Rho SBE-β-CyD polymer displayed remarkable activity towards *S. epidermidis* with MIC values in the nanomolar range. Comparing MIC values in Table 4.4 of free and complexed CLZ within the three carrier systems no statistically significant differences were measured in the inhibitory activity. Possibly CLZ drug encapsulated in the Rho SBE-βCyD polymer did not achieve bacterial targets because of its size changing in the medium used for the biological assays.

Having demonstrated the potent activity of the samples towards the reference strain of *S. epidermidis*, 4 clinical isolates presenting different antibiotic susceptibilities were tested. The antibiotic-resistant profile of each clinical strain and the antibacterial activity of the samples are reported in table 4.5.

Table 4.5 MIC_{50} values (µM) against clinical isolates of *S. epidermidis.*

	CLZ	CLZ/SBE -pβCyD	CLZ/Rho SBE-pβCyD	CLZ/Rho SBE-βCyD	CLZ/SBE-βCyD	Antibiotic-resistance profile
Isolate 1	0.07	0.07	0.25	0.11	0.06	CM^S, E^S, LVX^S, OX^S, TE^S, SXT^S
Isolate 2	0.02	0.03	0.25	0.02	0.03	CM^S, $\mathbf{E^R}$, LVX^S, OX^S, TE^S, SXT^S
Isolate 3[§]	0.05	0.06	0.25	0.06	0.06	CM^S, $\mathbf{E^R}$, $\mathbf{GMN^R}$, $\mathbf{LVX^R}$, $\mathbf{OX^R}$, TE^S, SXT^S
Isolate 4[§]	0.07	0.07	0.25	0.06	0.06	CM^S, $\mathbf{E^R}$, GMN^S, LVX^S, $\mathbf{OX^R}$, TE^S, $\mathbf{SXT^R}$

CM = Clindamicyn; E = Erythromycin; GMN = Gentamicin; LVX = Levofloxacin; OX = Oxacillin; TE = Tetracycline; SXT = Trimethoprim/Sulfamethoxazole
R = Resistant; S = Susceptible; I = Intermediate, as defined following the EUCAST guidelines, [§]*Staphylococcus* species resistant to oxacillin were declared, by convention, methicillin-resistant.

The antibacterial activity of CLZ drug and CLZ/SBE-β-CyD monomer was further characterised by means of time kill assays (Figure 4.10).
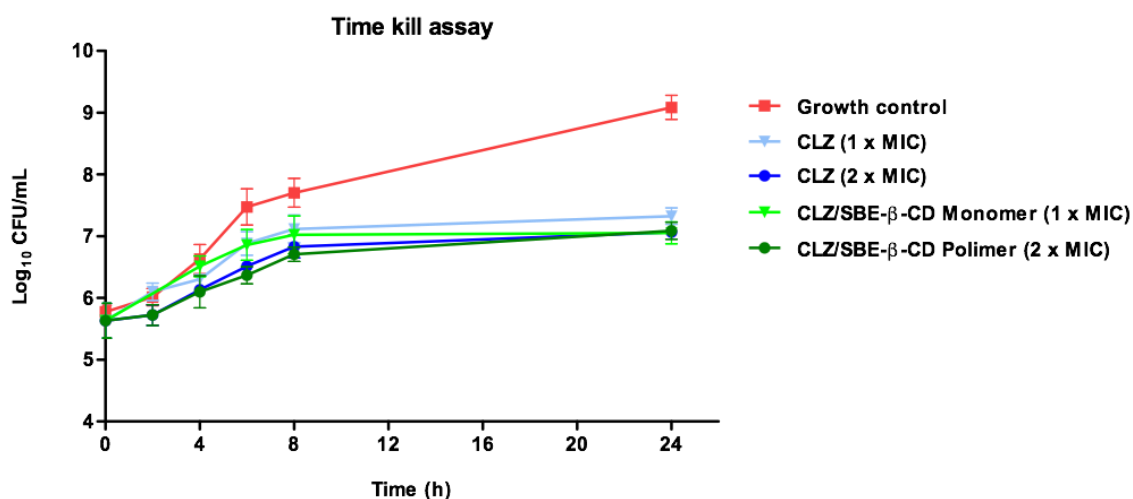
Figure 4.10 Time kill assay of CLZ-SBE-βCyD and CLZ-SBE-pβCyD against *S. epidermidis* at single and double MIC concentration along with control sample.

The activity observed for CLZ against *S. epidermidis* is not bactericidal at the tested concentrations as regrowth of bacteria was observed when samples were plated on MH plates. However, a significant reduction of 2 log units for log_{10} CFU/ml was measured comparing the control samples with the samples containing the drug at the two concentrations irrespective of carrier presence. In addition, growth inhibition seems to be concentration dependent up to 8 h of incubation with all CLZ samples, thereafter a similar final effect was achieved for all experimental conditions.

4.7.2 Cell viability
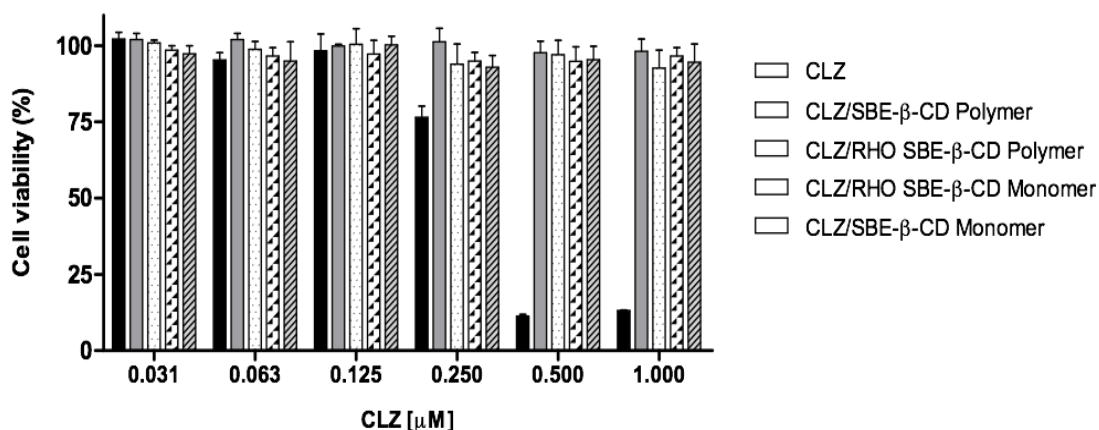
Figure 4.11 Cell viability test of CLZ, CLZ/SBE-βCyD, CLZ/SBE-pβCyD, CLZ/Rho-SBE-βCyD and CLZ/Rho-SBE-pβCyD in Vero cell line model
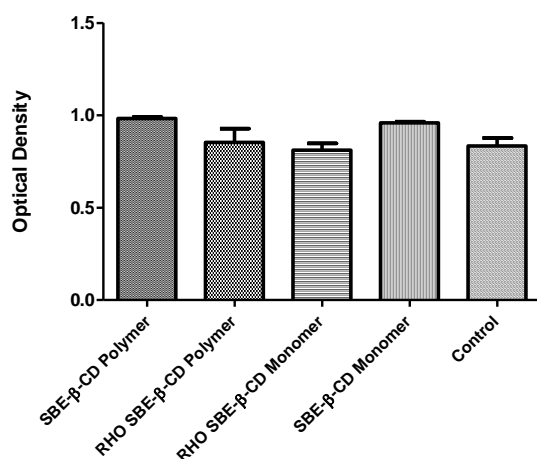
Figure 4.12 Cell viability test of SBE-βCyD carriers at 1 μM concentration in Vero cells

Finally, CLZ reference drug and all carrier sample preparations, containing CLZ and not as controls, were assayed for their effects on cell metabolism using Vero cells as experimental model.[10] Following 72-h of treatment with different concentrations of samples in the range 0.031-1 μM of CLZ, none of the CLZ/carrier preparation displayed cytotoxicity while the CLZ free compound completely inhibited cell proliferation at 0.5 and 1 μM (Figure 4.11). The lack of cytotoxicity holds also for the carriers alone (Figure 4.12). This is in line with literature data reporting SBE-βCyD is not cytotoxic while the data for the polymer have not been reported yet. Interestingly, the negatively charged polymer displays a behaviour that is similar to that of the neutral βCyD polymer.

4.8 CLZ release from SBE-pβCyD-chitosan film

CLZ with SBE-βCyD and SBE-pβCyD loaded chitosan films were prepared by solvent evaporation method.[11] CLZ with SBE-βCyD and SBE-pβCyD were dispersed in 1% chitosan solution prepared in 0.1M acetic acid and stirred, and then propylene glycol 200 (0.5%) was added as a plasticizer. The resulting dispersion was degassed to remove the air bubbles and poured in the petri dish (15 ml). This dispersion was dried at $36^{\circ}C$ for more than 24 hours. Films formed in the petri dish were peeled off and stored at room temperature in a closed environment. These prepared films were studied for CLZ release.

Drug release study was performed using a Franz diffusion cell holding PBS (pH-7.4) with 1.5% Tween 20. Receptor compartment was filled with diffusion media. Next, 2 cm^2 pieces of CLZ with SBE-βCyD and SBE-pβCyD loaded chitosan films were mounted on the cellulose dialysis membrane (MW cut off 12,000 Da) and tightened with donor compartment using clamps. This assembly was kept stirring at room temperature for 12 hours. 3ml samples were withdrawn from the receptor compartment at fixed time intervals. Absorption spectra were recorded to calculate drug release. Sink condition was maintained by replacing fresh media equivalent to sample amount withdrawn. We did not observe the absorption signal typical of CLZ for the 3 ml sample withdrawn from the Franz cell. This is indicative of low release efficacy. We observed coloration of the membrane suggesting the drug may be blocked in it.

4.9 Conclusions

We explored different carrier systems based on SBE-βCyD to load CLZ, an antibiotic with promising behaviour against multiple gram positive bacterial strains. We manage to load up to 0.5 mg/ml drug without the use of any organic solvents. With the polymeric carriers we obtained nanoparticles with size in the 20 to 70 nm range. Microfiltration is not causing any loss in material. The loaded carriers were tested on their cytotoxicity and bactericidal activity. Of utmost importance, the encapsulated drug is not cytotoxic up to 5 μM, while the drug alone is highly cytotoxic. Also the carriers alone are not cytotoxic in the range explored. Among the tested bacteria the best results were obtained with *S. epidermidis*. The drug has MIC_{50} values below 100 nM, similar to those of CLZ alone. The same holds also for the clinical isolates of *S. epidermidis*, some displaying MDR. Taken all together these results are very promising and in the future the loaded carrier will be tested in *in vivo* models.

4.10 References

1. *Tuberculosis*, **2008**, 88, 96-99.
2. M. C. Cholo, H. C. Steel, P. B. Fourie, W. A. Germishuizen and R. Anderson, *J. Antimicrob. Chemother.*, **2011**, 67, 290-298.
3. B. Lechartier and S. T. Cole, *Antimicrob. Agents Chemother.*, **2015**, 59, 4457-4463.
4. C. M. O'Driscoll and O. I. Corrigan, *Analytical Profiles of Drug Substances and Excipients*, **1992**, 21, 75-108.
5. R. K. Verma, W. A. Germishuizen, M. P. Motheo, A. K. Agrawal, A. K. Singh, M. Mohan, P. Gupta, U. D. Gupta, M. Cholo and R. Anderson, *Antimicrob. Agents Chemother.*, **2013**, 57, 1050-1052.
6. S. Valetti, X. Xia, J. Costa-Gouveia, P. Brodin, M.-F. Bernet-Camard, M. Andersson and A. Feiler, *Nanomedicine*, **2017**, 12, 831-844.
7. B. Roda, A. Zattoni, P. Reschiglian, M. H. Moon, M. Mirasoli, E. Michelini and A. Roda, *Anal. Chim. Acta*, **2009**, 635, 132-143.
8. S. F. Lincoln, J. H. Coates and R. L. Schiller, *J. Incl. Phenom. Macrocycl. Chem.*, **1987**, 5, 709-716.
9. C. Van Rensburg, G. Joone, J. O'sullivan and R. Anderson, *Antimicrob. Agents Chemother.*, **1992**, 36, 2729-2735.
10. C. Van Rensburg, A. Van Staden and R. Anderson, *Cancer Res.*, **1993**, 53, 318-323.
11. L. B. Rodrigues, H. F. Leite, M. I. Yoshida, J. B. Saliba, A. S. C. Junior and A. A. Faraco, *Int. J. Pharm.*, **2009**, 368, 1-6.

Chapter 5

Study of Clofazimine encapsulated in fluorescent Mesoporous Silica Particles for theranostic purposes

5.1 Introduction

In the last chapter, we focus on new fluorescent theranostic systems based on Mesoporous Silica Particles (MSPs) as carriers for antibiotics, in particular CLZ. MSPs consist of amorphous silicon dioxide having a porous structure within the solid framework, characterised by a large surface area and high pore volume.[1] They have been extensively explored in drug delivery and biomedical applications thanks to their high drug loading capacity, ease of surface functionalisation combined with good biocompatibility and low toxicity.[2,3,4] Various studies have reported that MSPs have the potential to increase the aqueous solubility of lipophilic drugs and enhance their bioavailability in *in vivo* models.[5] Additionally, MSPs have been modified through the covalent attachment of fluorescent labels making them useful tools for fluorescence-based techniques.[1] The latter approach is associated with a limitation as more synthetic steps to introduce the fluorescent label are required. Moreover, the fluorescent labels can occupy sites for drug loading or reduce drug accessibility to the pores. A challenging goal is thus the design of luminescent label-free MSPs easily synthesised with inexpensive procedures not requiring expensive, bulky or sometimes photolabile fluorophores. In this frame recent literature reports the development of stable and strongly fluorescent MSPs by *in situ* generation of small carbon dots (CDs) within the porous structure.[6,7] CDs were created upon partial decomposition of carboamino groups linked to the surface of the MSPs.[6] Intrinsically fluorescent MSPs can become interesting tools for theranostics, affording the possibility of contemporary drug delivery at the target site and particle tracking by means of fluorescence.

Fluorescence-based assays are very popular and intensitvely used in the biomedical field but often depend on the fluorescence intensity feature which is influenced by the fluorophore local environment and autofluorescence from biological species can hamper data interpretation and analysis. Consequently, advanced fluorescence tools have been developed which monitor ratiometric fluorescence signals or fluorophore spectral features.[8,9] Only few exploit the fluorescence lifetime even though it is one of the most powerful and environment-sensitive features that provides information even when fluorescence intensity and spectral data fail to obtained details about the

sample.[10,11,12] Fluorescence lifetime imaging has become a powerful tool for the investigation of biological matter and a valuable technique in the theranostic field. [8,10,13,14]

Scheme 5.1 Clofazimine (CLZ)
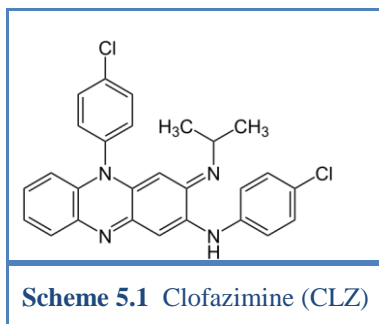
In this context, we extensively studied luminescent label-free MSPs prepared by the Swedish company Nanologica. We report in the following how the fluorescence properties change with the textural features (i.e., surface area, pore size and pore volume) of MSPs as well as the amount of carboamino groups linked to the surface. Next, clofazimine (CLZ, scheme 5.1), was encapsulated in fluorescent MSPs. In order to assess the possibility of tracking both particle and drug separately in biological environments, we performed an in-depth study of the photophysical properties of both CLZ and CLZ loaded MSPs and time-resolved fluorescence measurements allowed to differentiate between the drug/carrier and carrier systems.

5.2 Information on the preparation of luminescent Mesoporous Silica Particles

Three types of Mesoporous Silica Particles (MSPs) have been studied, all prepared by Nanologica. **NLAB3** samples are MSPs synthesised via anionic surfactant-templated condensation using N-lauroyl-L-alanine as anionic template.[15] Condensation of 3-aminopropyl triethoxysilane (APTES) as co-structure directing agent and tetraethyl orthosilicate (TEOS) in the presence of the template results in gel formation. The gel was filtered out and further dried at room temperature under atmospheric condition. The anionic template was removed by calcination at $600\,^{\circ}C$ for 6 hours and the powder was isolated. The procedure affords 100-500 nm particles with an internal mesostructure organised in a 3D bicontinuous cubic structure (*Ia3d*). **NLAB8** samples are synthesised using the cationic surfactant, cetyltrimethylammonium bromide (CTAB) as template under alkaline condition.[16] Their preparation is based on the well established MCM-41 procedure, that consists in the calcination of aluminosilicate gels in the presence of a template, adopting a 50:50 mixture of water:acetone instead of water used in the standard method. Monodispersed silica particles of around 2 μm form having a mixed 2D hexagonal and 3D cubic structure suggested by low angle XRD. The pores have a diameter of ca. 30 Å equivalent to that of the template surfactant micelles. **NLAB14** samples are mesoporous silica particles synthesised using a sol-gel emulsion method with a silica precursor to obtain a particle size of 5 μm. Pores were due to condensation and drying of gel which led

a broader pore size in comparison to the template methods. It is further calcinated at 600°C for 6 h to remove organic solvent residues. NLAB14 sample do not display any specific crystallographic space group symmetries, suggesting the presence of disordered mesostructures.[17]
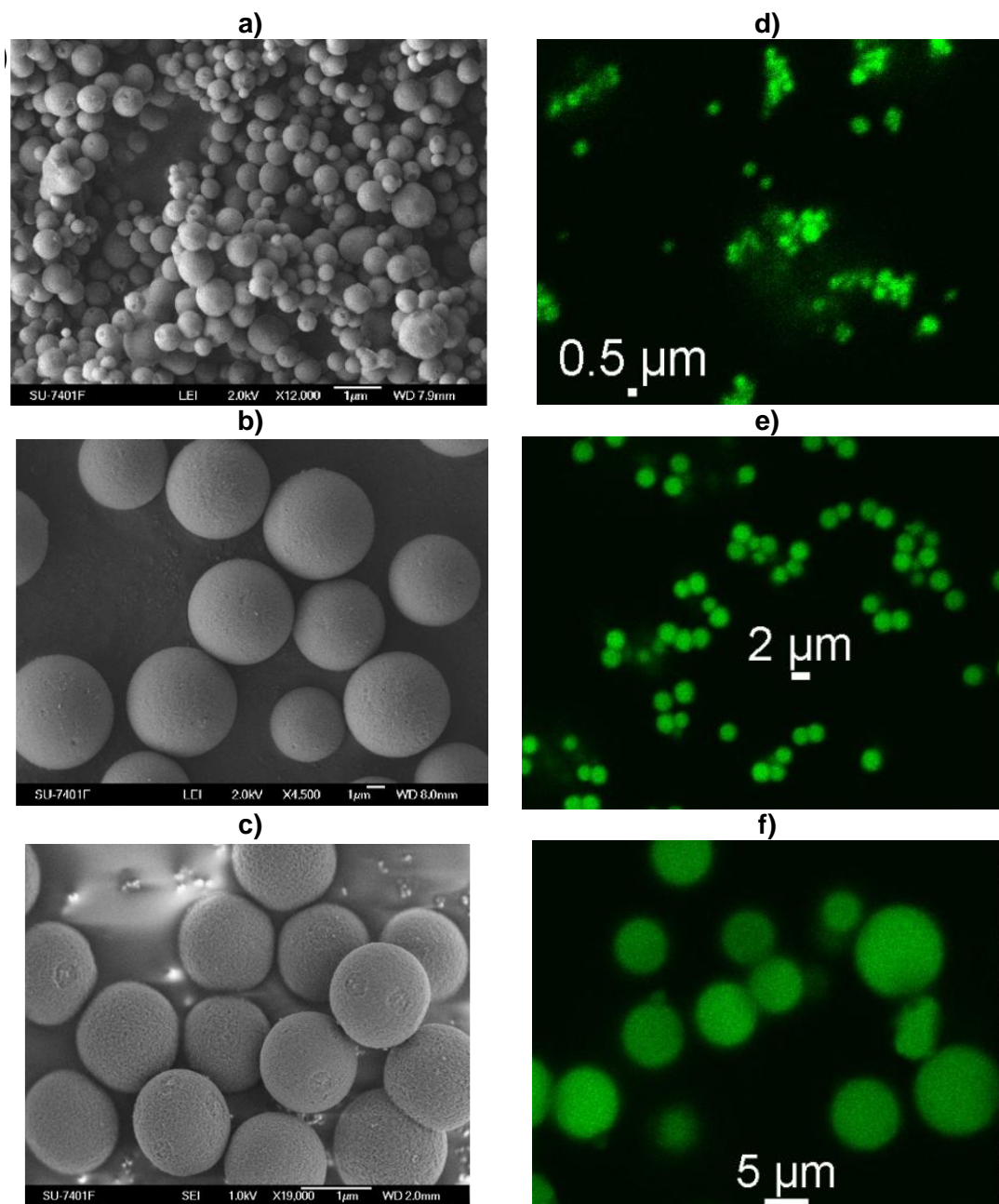
Figure 5.1 (**a–c**) Scanning electron microscopy images of unfunctionalised MSPs and (**d–f**) Confocal fluorescence microscopy images of fluorescent MSPs showing a particle diameter of around 0.5 μm for NLAB3 (**a** and **d**), 2 μm for NLAB8 (**b** and **e**) and 2–7 μm for NLAB14 (**c** and **f**); MSPs were excited at 405 nm and emission was collected in the 500–550 nm range (SEM images were obtained in collaboration with Nanologica, Sweden).

Next, carboamino-functionalisation was performed using APTES for the NLAB8 and NLAB14 particles. Calcined samples were rehydrated to afford the silanol groups (SiOH). The amount of APTES added corresponds to an APTES:SiOH molar ratio of 1:3 with

SiOH amount determined by TGA. In the case of NLAB14 different APTES:SiOH molar ratios of 0.05:3, 0.5:3, 1:3, were used to have respectively low (L), medium (M) and high (H) functionalisation amount. In the case of NLAB3, carboamino functions were already present in the particles after synthesis since APTES was used as a co-structure directing agent. The as-made solid particles were refluxed with EtOH and HCl 20% w/w for the complete removal of the surfactant leaving carboamino groups on the silica surface (NLAB3-carboamino). Finally to obtain fluorescent particles, a controlled calcination up to 400 °C was performed for NLAB3-carboamino, NLAB8-carboamino and NLAB14-carboamino samples.

All particles are spheres (Figure 5.1) with different sizes and significant differences in mesoporous properties. The particle sizes chosen are well accepted for oral and aerosol drug administration.[18] Table 5.1 collects all porosity features obtained from low angle X-ray diffraction and nitrogen adsorption and desorption curves shown in Figure 5.2. The data refer to MSPs before and after carboamino functionalisation, as well as after calcination of the functionalised MSPs. NLAB3 MSPs have a large surface area and high pore volume (Table 5.1). NLAB8 MSPs consist in particles with a large surface area but low pore volume. NLAB14 MSPs display a low surface area with high pore volume.
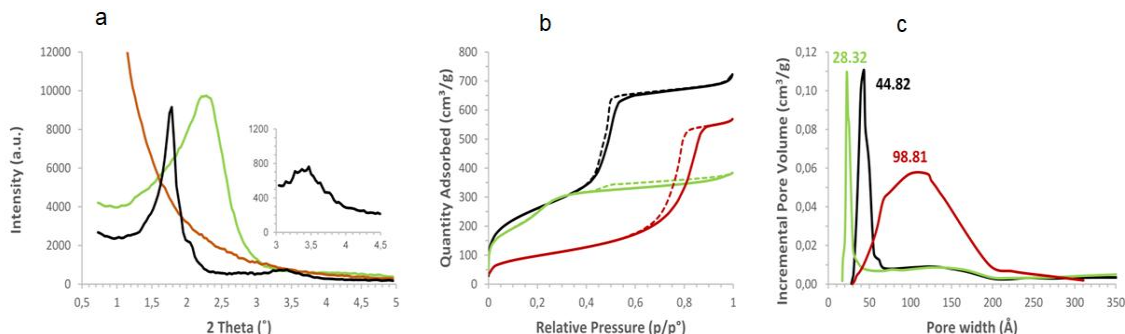
Figure 5.2 (**a**) Low angle X-ray diffraction patterns show mesoscale peaks that may be indexed on the basis of a 3D bicontinuous cubic structure (Ia3d) for NLAB3 (black line, also inset), a mixed 2D and 3D unit cell for NLAB8 (green line) and a non-ordered structure for (red line). (**b**) Nitrogen adsorption/desorption shows isotherm profile type IV for NLAB3 (black) and NLAB14 (red) and a mix isotherm type for NLAB8 (green). Solid and dotted lines show adsorption and desorption, respectively. (**c**) Pore size distribution shows a sharp small pore size for NLAB8 (green), small-medium size for NLAB3 (black) and broad and large pore size distribution for NLAB14 (red). Values display BJH Adsorption average pore width for each sample (data obtained in collaboration with Nanologica, sweden)

The qualitative analysis of carboamino-functionalisation was studied by thermogravimetric analysis (TGA). The amount of initial degree of carboamino surface functionalisation ranged from 6.8 to 24.6% w/w (Table 5.1) decreasing to 3.1-10.3% after calcination.[19] Interestingly, mesoporosity values after controlled calcinations for all three particle were similar to those prior to carboamino functionalisation.

Table 5.1 Properties of the MSPs used in this study: unfunctionalised MSP (NLAB), carboamino-functionalised MSP (NLAB-carboamino) and fluorescent carboamino-functionalised MSP after controlled calcination (NLAB-F).

Sample	Average Particle Diameter (μm) [a]	Specific Surface Area (m²g⁻¹) [b]	Specific Pore Volume (cm³/g) [b]	Average Pore size, (Å) [b]	Carboamino groups (% w/w) [c]
NLAB3	0.45	931	1.27	44.82	-
NLAB8	2	987	0.66	28.32	-
NLAB14	5	351	0.93	98.81	-
NLAB3-carboamino	0.45	671	0.98	41.13	24.55
NLAB8-carboamino	2	80	0.11	*Nd*	10.28
NLAB14-carboamino	5	353	0.99	98.09	6.79
NLAB3-F	0.45	962	1.40	44.93	10.32
NLAB8-F	2	1134	0.72	18.35	4.43
NLAB14-F	5	353	0.93	100.57	3.11

Note – Data were obtained in collaboration with Nanologica, Sweden.

Three different degrees of carboamino functionalisation were evaluated using NLAB14-F-H (high), 7.51% w/w; NLAB14-F-M (medium), 4.02% w/w; NLAB14-F-L (low), and 3.31% w/w carboamino groups.

5.3 Photophysical study of fluorescent MSPs

Interestingly, all MSPs become fluorescent only after controlled calcination of functionalised silica particles having carboamino groups. Silica particles without carboamino groups do not produce the fluorescent particles after calcination as evidenced by the fluorescence confocal images completed with the DIC image in Figure 5.3. Calcinated silica particles NLAB14-F with the three degrees of carboamino functionalisation suspended in water were examined. Even using the integrating sphere to avoid interference of light scattered by silica particles, no reliable absorption spectra could be acquired. We have recorded the fluorescence spectra of the silica particle suspensions exciting in the 320-460 nm range. Figure 5.4 represents the fluorescence emission and excitation spectra of NLAB14-F-H and NLAB14-F-M particles.
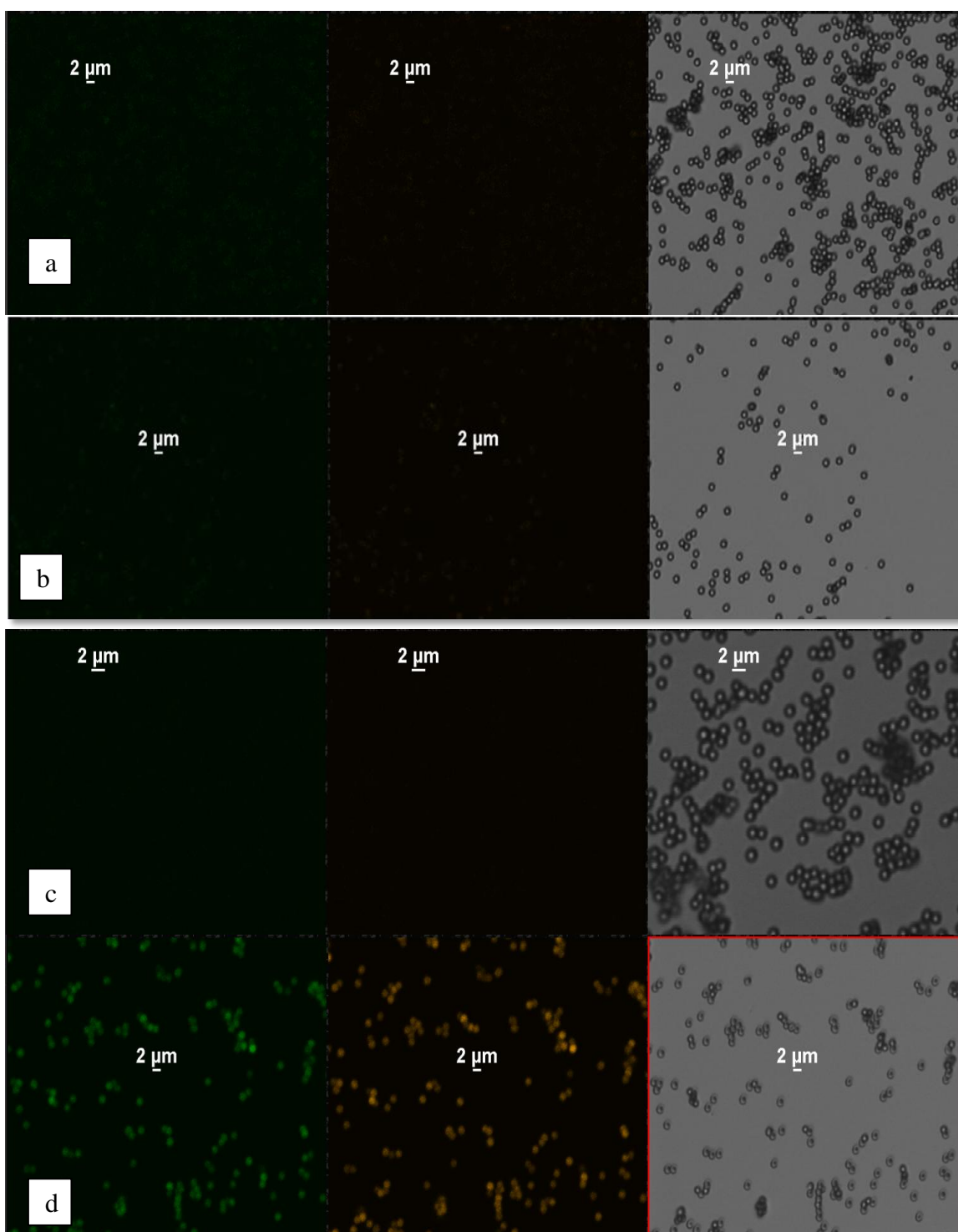
Figure 5.3 Confocal fluorescence images (in 500-550 nm range, green, and 565-605 nm range, orange) and DIC images all obtained for excitation at 488 nm of NLAB8 without carboamino funtionalisation, before (**a**) and after (**b**) calcination, with carboamino funtionalisation before (**c**) and after calcination (**d**).

NLAB14-F-L doesn't exhibit emission in water suspension in the same experimental conditions. Reliable fluorescence quantum yields could not be obtained due to scattering of these three types of particle. The fluorescence spectra extending into the visible range depend in shape and, apparently, in intensity on the excitation wavelength with the maximum shifting to the red when increasing the excitation wavelength.
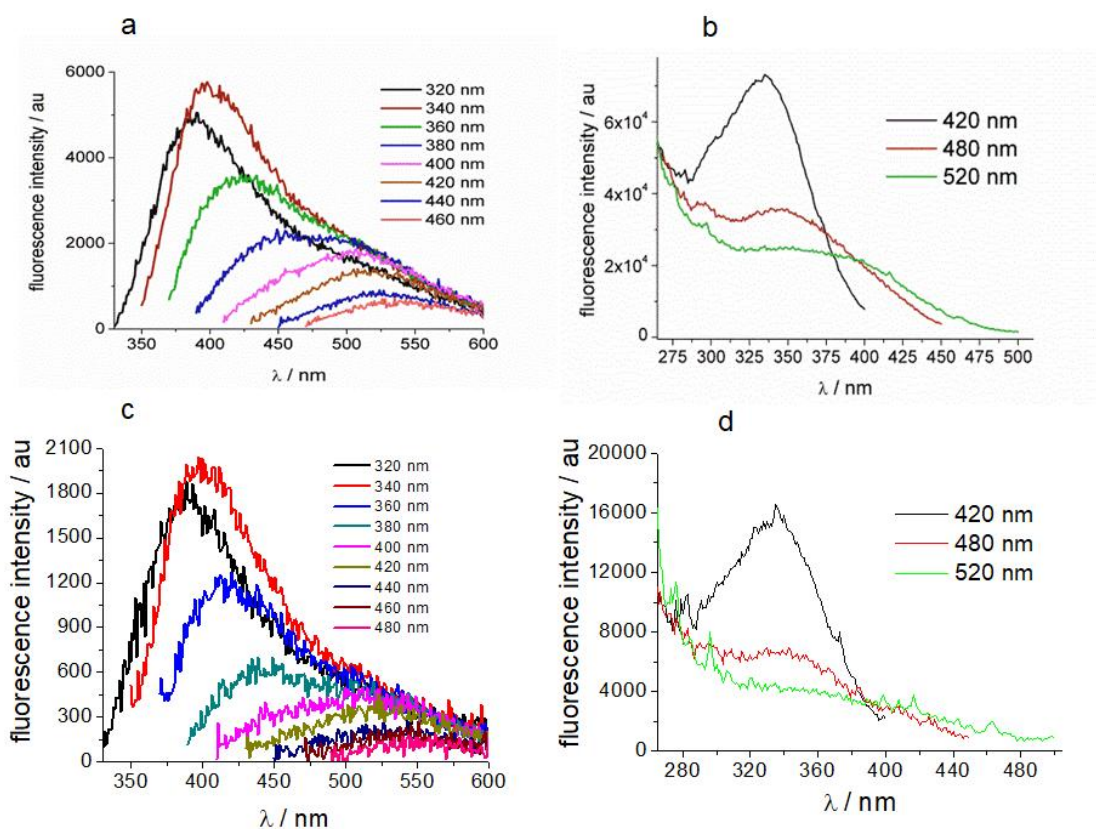
Figure 5.4 (**a**) Fluorescence emission spectra of NLAB14-F-H suspensions in water for excitation at different wavelengths; (**b**) Fluorescence excitation spectra of NLAB14-F-H suspensions in water for different emission wavelengths; (**c**) Fluorescence emission spectra of the NLAB14-F-M sample suspended in water obtained for different excitation wavelengths; (**d**) Fluorescence excitation spectra of the NLAB14-F-M sample suspended in water for different emission wavelengths; 0.5 mg/ml of MSPs; d = 1cm.

A similar trend is observed for NLAB14-F-M. This shift of the wavelength has been reported in the literature and the origin of the shift is a subject of discussion.[6,20,21,22] A similar progression can be observed in the fluorescence excitation spectra, with the maximum shifting with the changing emission wavelength. Relevant for theranostic applications is that the fluorescence excitation spectra exhibit large bands extending in the blue spectral region that can be explored in biological fluorescence imaging.

We used the time-correlated single photon counting (TCSPC) technique to examine the fluorescence decay of the suspensions of NLAB14-F-H and NLAB14-F-M exciting at 407 nm. Convergence of the fitting procedure requires a triexponential function for NLAB14-F-H and a biexponential function for NLAB14-F-M (Table 5.2). In all the samples we observed one very short lifetime that is below the instrument resolution and it is most likely due the strong scattering of particles with a mean diameter of 5 μm. Importantly, particles show a fluorescence lifetime of more than 9 ns at 520 nm which can be easily distinguish from the biological autoflourescnce having a fluorescence lifetime of ca. 3 ns associated with the fluorescence of the protein-bound NADH and free FAD cofactors.[23,24]

We also studied the silica particles by means of laser scanning time-resolved fluorescence confocal microscopy in view of their application as drug carriers. Figure 5.5 represent the confocal images of NLAB14-F-H, NLAB14-F-M and NLAB14-F-L particles examined under similar experimental conditions with excitation at 405 nm. NLAB14-F-H particles are clearly brighter than the other two silica particles having medium and low degree of functionalisation. Again in case of NLAB14-F-L, we could not detect emission under similar experimental conditions. Figure 5.5d displays a comparison of the fluorescence spectrum recorded using a spectrofluorometer (λ_{exc} = 400 nm) for a NLAB14-F-H aqueous suspension and the fluorescence spectra of different regions of interest (ROIs) observed for the NLAB14-F-H powder on the confocal microscope (λ_{exc} = 405 nm). They have very similar appearance.

Solid powder of MSPs were further characterised by means of fluorescence lifetime imaging. Figure 5.5e displays the fluorescence decays in the 500–550 nm range of NLAB14-F-H and NLAB14-F-M powders calculated for selected ROIs containing only silica particles without background. The fluorescence decay profiles are almost identical, and fitted with a tri-exponential decay function. We obtain the lifetimes reported in Table 5.2 together with their frequency after full image fitting keeping the lifetime values fixed. The fluorescence decay is dominated by the long lifetime species (Table 5.2). The long lifetime values are in agreement with those recorded for the suspensions and with other literature data.[25,26] Multi-exponential decays can be due either to different fluorophoric species, such as CDs of different size, and/or different microenvironments of the fluorophoric entities.[25,26] We also recorded the fluorescent decay in the 565–605 nm range and observed similar results although emission is weaker. Figure 5.1d-f represents the confocal fluorescence intensity images of the fluorescent particles NLAB3-F, NLAB8-F and NLAB14-F. In particular, with the larger particle, it is possible to discern the homogeneously distributed fluorescence within the particles, which propose that the carbon dots are generated throughout the entire particle. Figure 5.6 displays both slice and a 3D volume view obtained from Z-stack images of the NLAB14-F and NLAB8-F particles supporting this thesis. Note that dimensions of the carbon dots are extremely small below the spatial resolution of this confocal imaging technique so it is not possible to observe single CDs.
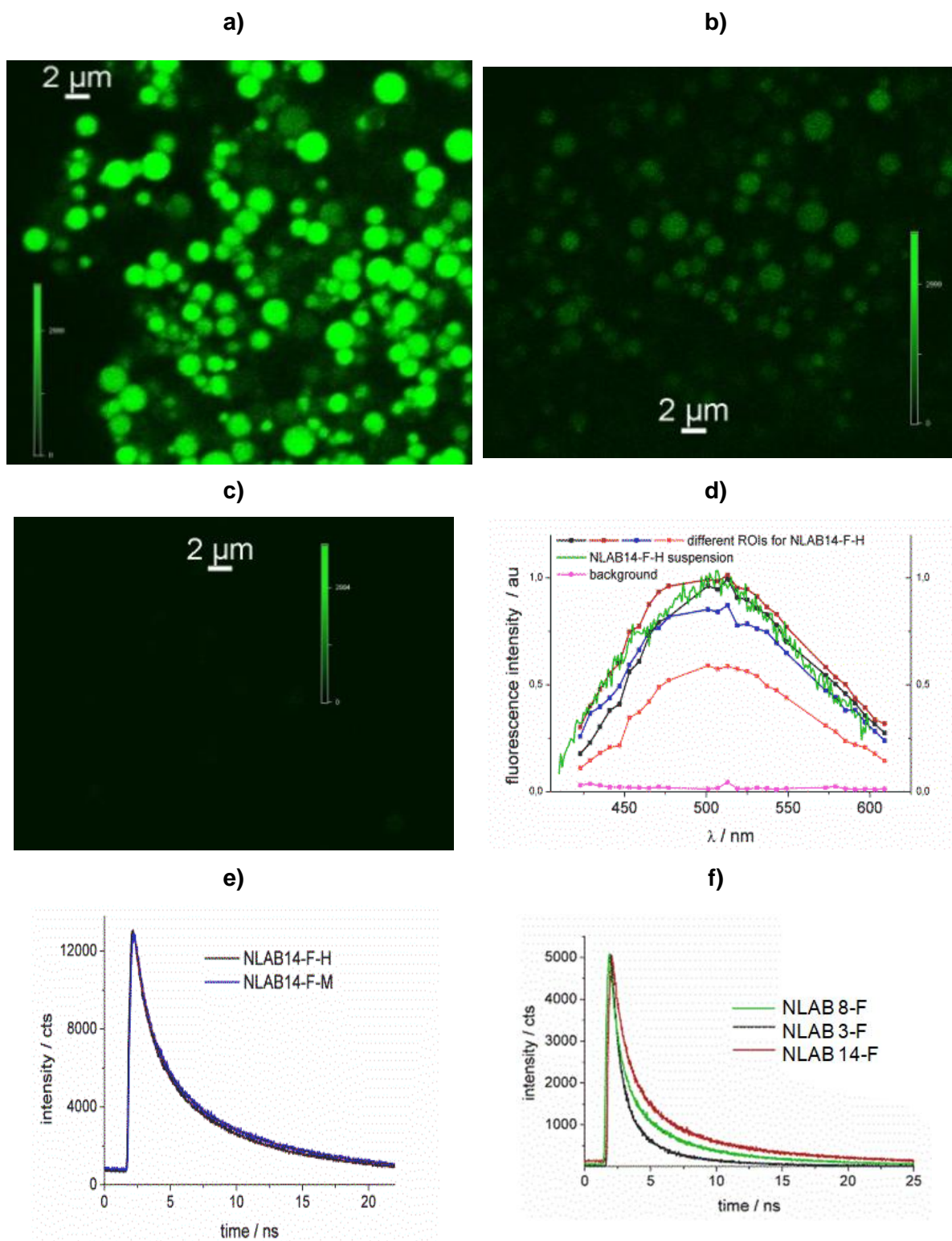
Figure 5.5 (**a-c**) Confocal fluorescence images of the particles obtained under identical experimental conditions; sample was excited at 405 nm and emission collected in the 500-550 nm range using a 60X oil immersion objective. Image intensity scale is the same for the three samples. 2 µm scale bar is shown. (**d**) Fluorescence spectrum obtained with the spectrofluorimeter, λ_{exc} 400 nm, for a NLAB14-F-H suspension in water and the fluorescence spectra of different ROIs obtained for NLAB14-F-H powder on the confocal microscope, λ_{exc} 405 nm. (**e**) Fluorescence decay of NLAB14-H and NLAB14-M powder at 520 nm, λ_{exc} 405 nm. (**f**) Fluorescence decay of NLAB3-F, NLAB8-F and NLAB14-F powder at 520 nm, λ_{exc} 405 nm.

Fluorescence lifetime imaging (FLIM) was performed exciting at 405 nm and the images obtained with the lifetimes reported in Table 5.2, are shown in Figure 5.9. The average lifetime of NLAB3-F is significantly shorter compared to that of two other silica particles. There is no correlation between the average fluorescence lifetime and the pore size, indeed, NLAB8-F with the smallest pore size has the intermediate average lifetime. We can, however, discern a correlation of the average lifetime with the residual carboamino amount, which is indeed lower in the case of NLAB8-F and NLAB14-F compared to NLAB3-F. Amine groups are well-known electron donors able to act as fluorescence quenchers causing lifetime shortening.[27]

NLAB14-F slice view

NLAB14-F 3D volume view

NLAB8-F slice view

NLAB8-F 3D volume view

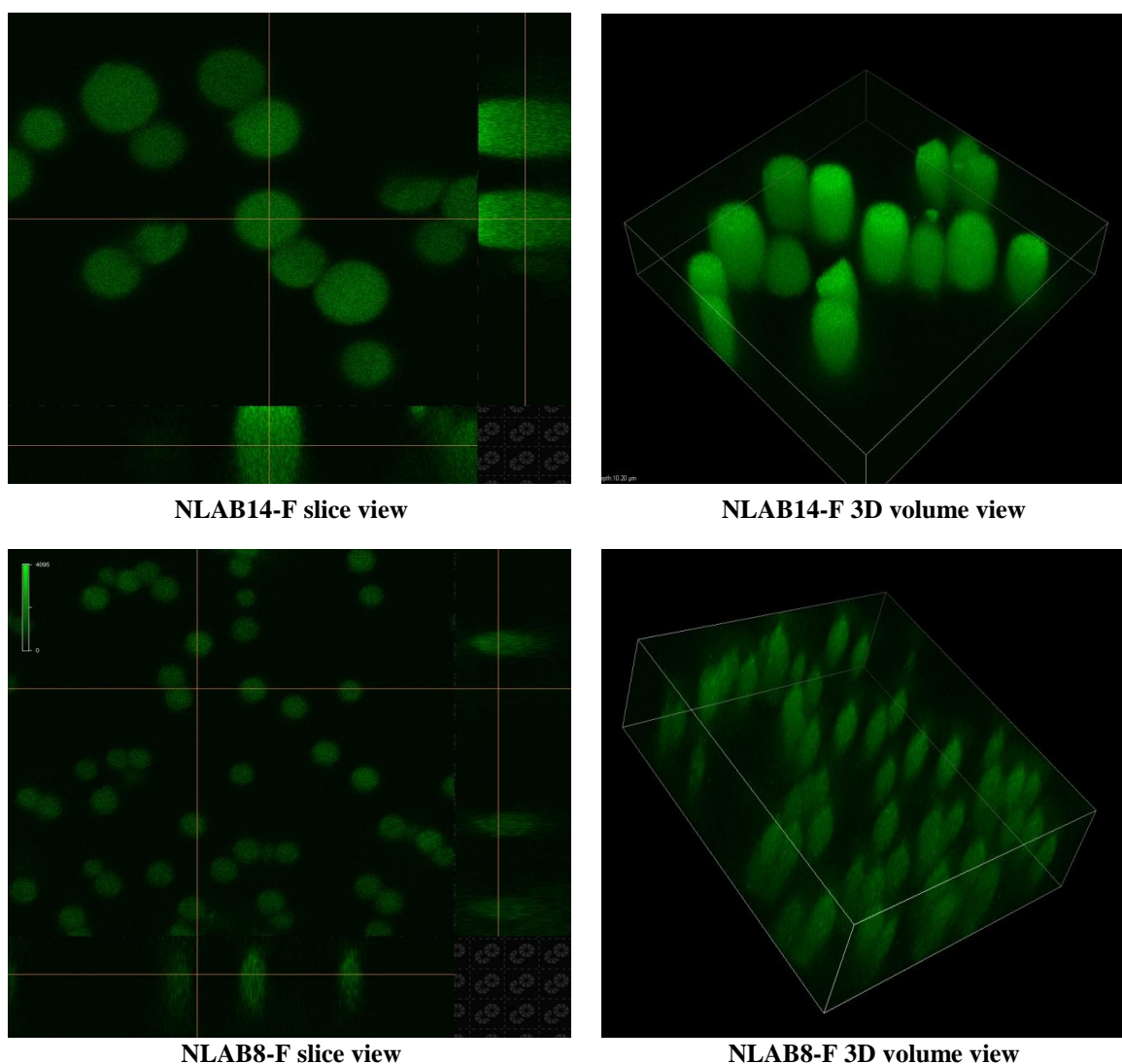**Figure 5.6** Confocal fluorescence images of the NLAB14-F and NLAB8-F collecting emission at 520 nm for excitation at 405 nm showing the slice and a 3D volume view of Z-stack images of the NLAB14-F and NLAB8-F particles

Table 5.2 Bi- and tri-exponential fitting parameters of the fluorescence decay of NLAB14-F-H and NLAB14-F-M aqueous suspensions and NLAB14-F-H/M and NLAB3/8/14-F powders.

Water[a]	τ_1 /ns	τ_2 /ns	τ_3 /ns	a_1 (f_1)	a_2 (f_2)	a_3 (f_3)
NLAB14-F-H	0.08	3.1	9.1	0.94 (47%)	0.009 (16%)	0.007 (37%)
NLAB14-F-M	0.08	9.7		1.3 (85%)	0.002 (15%)	

Powder[b]	τ_1 /ns	τ_2 /ns	τ_3 /ns	Events	Events	Events
NLAB14-F-H	0.8	2.6	10.7	0.4E6	1.0E6	3.2E6
NLAB14-F-M	0.9	2.3	9.7	0.1E5	0.7E5	3.0E5
NLAB14-F	0.8	2.8	10.9	0.8E6	2.6E6	5.4E6
NLAB8-F	0.6	2.4	8.0	1.7E5	5.7E5	9.7E5
NLAB3-F	0.6	1.7	5.5	2.8E5	5.0E5	5.4E5

[a] fluorescence decay collected at 520 nm.
[b] data from confocal fluorescence lifetime imaging.

5.4 Photophysical study of fluorescent MSPs loading CLZ

CLZ was encapsulated in the different silica particles (NLAB3, NLAB8 and NLAB14 and fluorescent MSPs NLAB3-F, NLAB8-F and NLAB14-F) to explore MSPs as drug carrier. CLZ encapsulation was performed by using solvent evaporation method with acetone as the organic solvent to dissolve the CLZ and after addition of silica particle the mixture was kept stirring and subjected to solvent evaporation under controlled atmospheric condition with rota evaporator.

The amount of CLZ loaded was determined by TGA. Differential scanning calorimetry (DSC) profiles of NLAB3-F/ CLZ and NLAB14-F/CLZ confirmed the presence of the drug in its amorphous form due to the absence of the crystalline melting peak of CLZ around 230 °C. The CLZ encapsulated amounts were 13 and 5% w/w for NLAB3-F/CLZ and NLAB14-F/CLZ, respectively. CLZ encapsulation in NLAB8-F particles with small pore size was obtained introducing a modification in the carboamino functionalisation procedure which preferentially functionalised the external silica surface and hence, the final CLZ loading amount in NLAB8-F/CLZ was about 4% w/w.

In solution the photophysical characterisation was limited to the aqueous suspension of NLAB3-F/CLZ having the smallest particle size of 450 nm as data are less affected by scattering. The peculiar CLZ absorption band at ca. 485 nm reveals the presence of CLZ in NLAB3-F/CLZ. (Figure 5.7a). These absorption spectra are comparable to that of CLZ

solubilised in a H_2O/EtOH 95/5 v/v mixture. As reported in literature CLZ is practically insoluble in water (solubility 0.225 mg /l).[28]
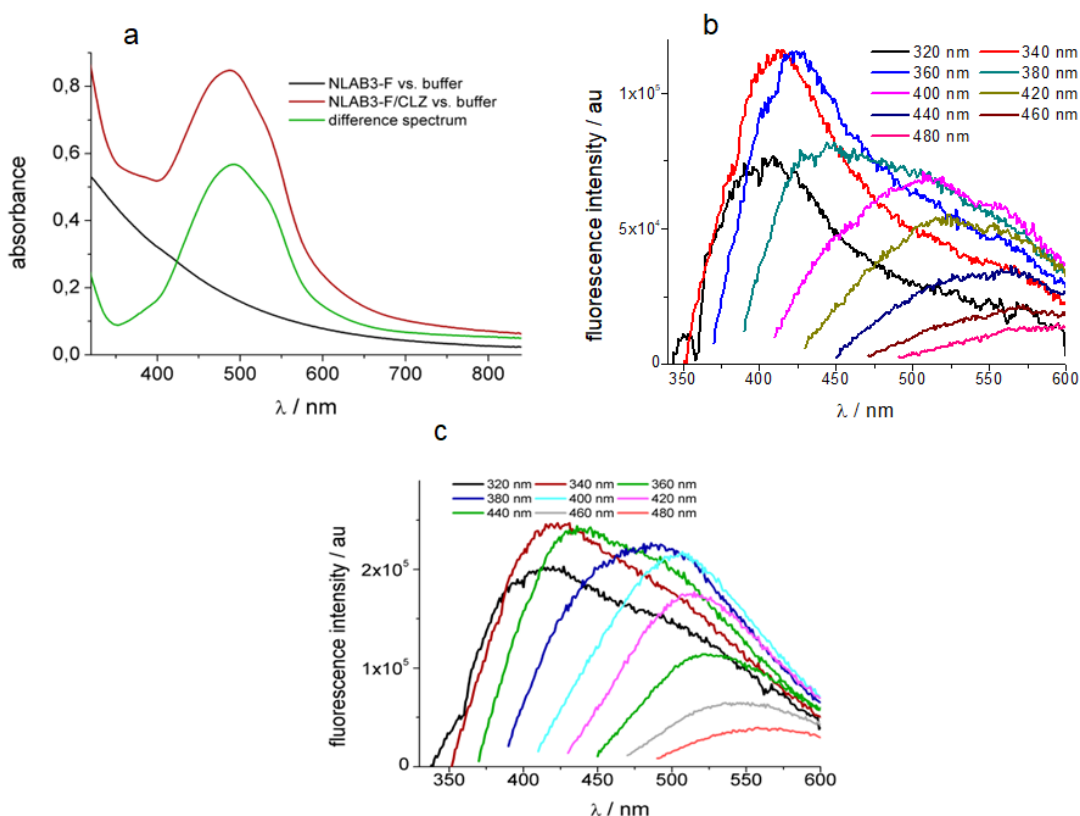
Figure 5.7 **(a)** Absorption spectra of aqueous suspensions of NLAB3-F and NLAB3-F/CLZ. 0.5 mg/ml; **(b)** Fluorescence emission of NLAB3-F/CLZ for different excitation wavelengths; **(c)** Fluorescence emission of NLAB3-F for different excitation wavelengths

CLZ dissolved in DMSO shows fluorescence in the 460–760 nm range with two lifetimes of 0.1 and 2.3 ns. The fluorescence spectra of NLAB3-F/CLZ and NLAB3-F shown in Figure 5.7b-c are significantly affected by the excitation wavelength and it is hard to identify CLZ emission peaks at 552 and 582 nm observed in DMSO because they overlap with intrinsic fluorescence of the silica particles. Anyway, especially for excitation in the visible region, the red side of the spectra of NLAB3-F/CLZ exhibit a shoulder that could be associated with CLZ emission. To ascertain the CLZ contribution we collected fluorescence decays by exciting NLAB3-F and NLAB3-F/ CLZ suspensions both at 331 and 465 nm. At the latter wavelength CLZ is absorbing well. The experiment performed under the conditions that favor the fluorescence of MSPs shows the fluorescence decay of NLAB3-F/CLZ and NLAB3-F at 480 nm is almost equivalent when excited at 331 nm (Figure 5.8a and Table 5.3).

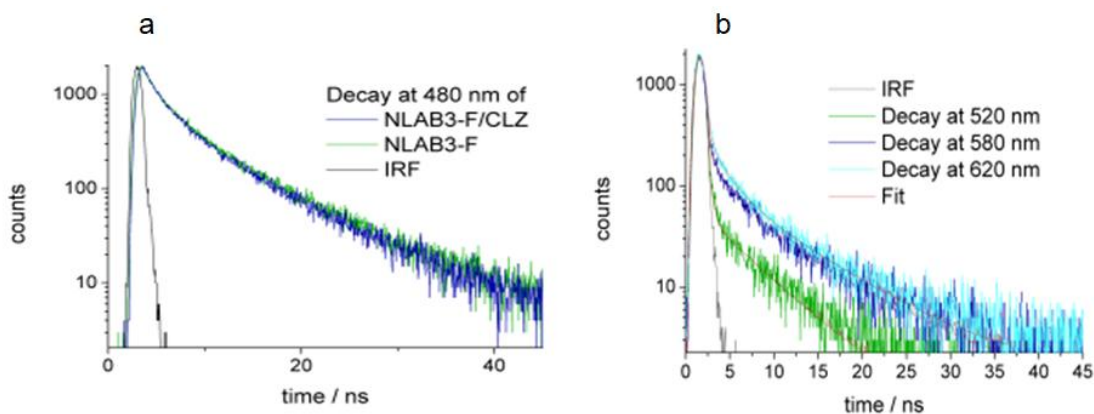**Figure 5.8** (**a**) Fluorescence decay of NLAB3-F and NLAB3-F/CLZ, λ_{exc} = 331 nm; λ_{em} = 480 nm; (**b**) Fluorescence decay of NLAB3-F/CLZ measured at different wavelengths; λ_{exc} = 465 nm; λ_{em} = 520, 580 and 620 nm.

However, when excited at 465 nm a large increase in the relative contribution of the short lifetime species appears in the overall decay (Figure 5.8b and Table 5.3) which is not due to scattering. In fact, when excited 331 nm, we do not observe any significant short-lived scattering contribution. So the short lifetime contribution in Figure 5.6b is mostly likely from CLZ that has lifetime below the instrumental time resolution. The long-lived tail of the fluorescence decay is due to the intrinsic fluorescence of MSPs.

Table 5.3 Parameters of the bi- or tri-exponential fit of the fluorescence decay obtained for water suspensions.

Excitation at 331 nm and emission measured at 480 nm

Sample	τ_1/ns	τ_2/ns	τ_3/ns	f_1 (%)	f_2 (%)	f_3 (%)
NLAB3-F	0.46	2.71	8.74	11	40	49
NLAB3-F/CLZ	0.34	2.80	9.15	11	40	49

Excitation at 465 nm[a]

NLAB3-F/CLZ	τ_1/ns	τ_2/ns	τ_3/ns	f_1 (%)	f_2 (%)	f_3 (%)
520 nm	0.01	5.30		97	3	
580 nm	0.03	2.77	8.71	86	6	8
620 nm	0.05	1.94	7.55	72	10	17

[a] decay has been measured at different wavelengths indicated in the table.

Next, we exploited the fluorescence decay features for optical imaging. The confocal fluorescence lifetime images (FLIM images) are shown in Figure 5.9 for the three types of MSPs with and without CLZ. The fluorescence decay was calculated for the regions of interest corresponding to particles and it was fitted with a tri-exponential function. The lifetime image was obtained calculating the pre-exponentials in each pixel while keeping the lifetime values fixed. The image color refers to the average lifetime value

according to the scale on the right. A long average lifetime of up to 6 ns is observed without CLZ. Differently, MSPs with CLZ exhibit average lifetime shortening to less than 1 ns confirming that CLZ has been loaded. This result was obtained for excitation performed at both 405 and 485 nm. The FLIM images also show that CLZ is uniformly distributed in the NLAB3-F and NLAB14-F particles. Noticeably, NLAB8-F/CLZ FLIM images show some particles with longer average lifetime likely representing empty particles or particles with extremely low amounts of CLZ. This variation could be due to the small nanopores which restrict the amount of loaded CLZ (about 4% w/w).
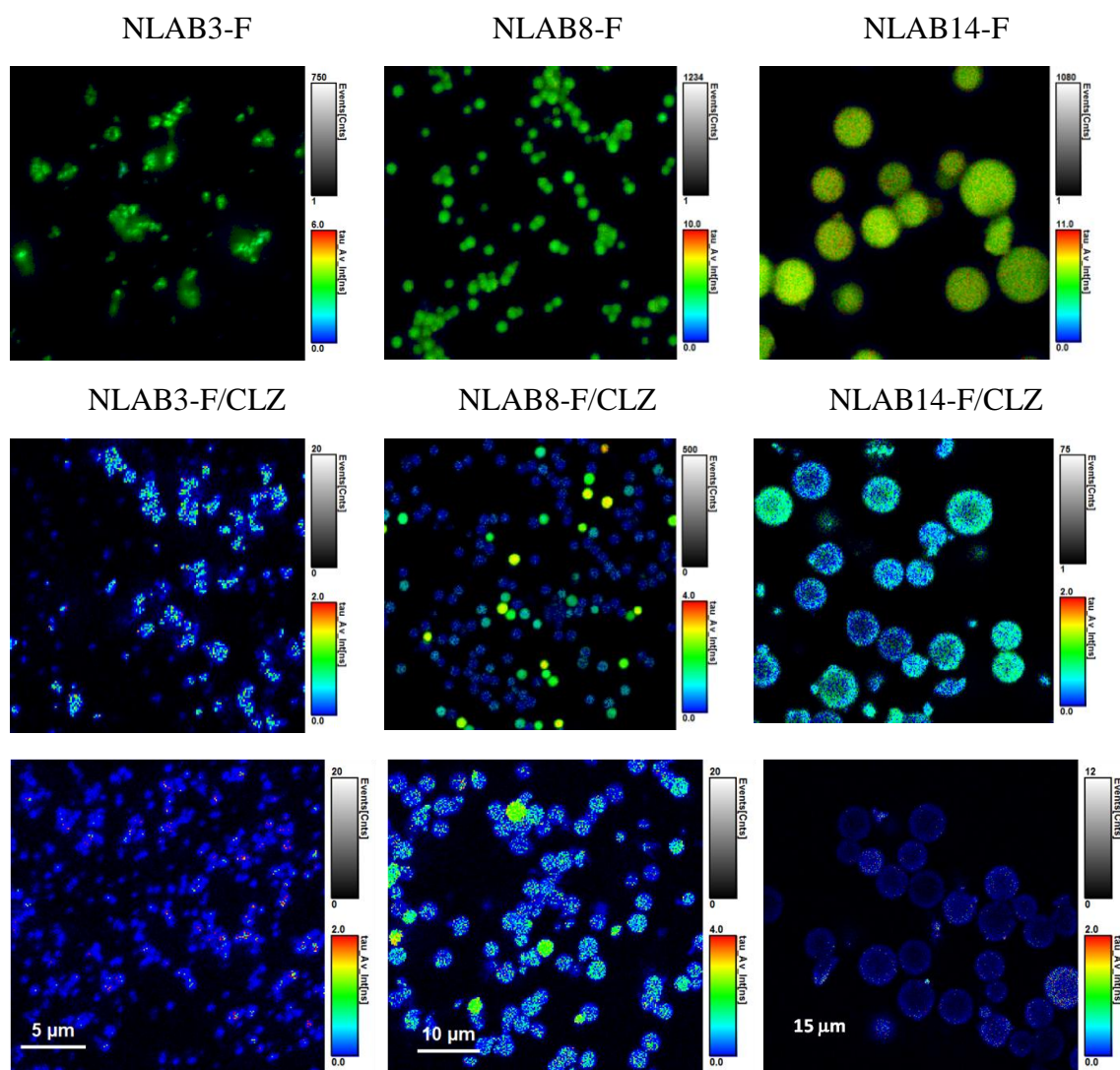
Figure 5.9 FLIM images: (top) unloaded fluorescent MSPs , decay collected in the 500-550 nm range exciting at 405 nm; (middle) CLZ loaded MSPs, decay collected in the 565-605 nm range exciting at 485 nm; (bottom) CLZ loaded MSPs decay collected in the 500-550 nm range exciting at 405 nm; the colour scale bar is representative of the average lifetime of each pixel.

This relevant piece of information about drug encapsulation escaped TGA. When we excited at 405 nm and collected photon emission in the 500–550 nm range, we observed a decay that can be fitted with a tri-exponential decay function resulting again in

short average lifetimes below 1 ns (see Figure 5.9) suggesting that CLZ fluorescence is quenching the intrinsic silica fluorescence. In order to confirm that CLZ is indeed able to emit in the MSPs and to exclude emission is due exclusively to scattering we performed spectral and lifetime imaging on the non-fluorescent MSPs loaded with CLZ.
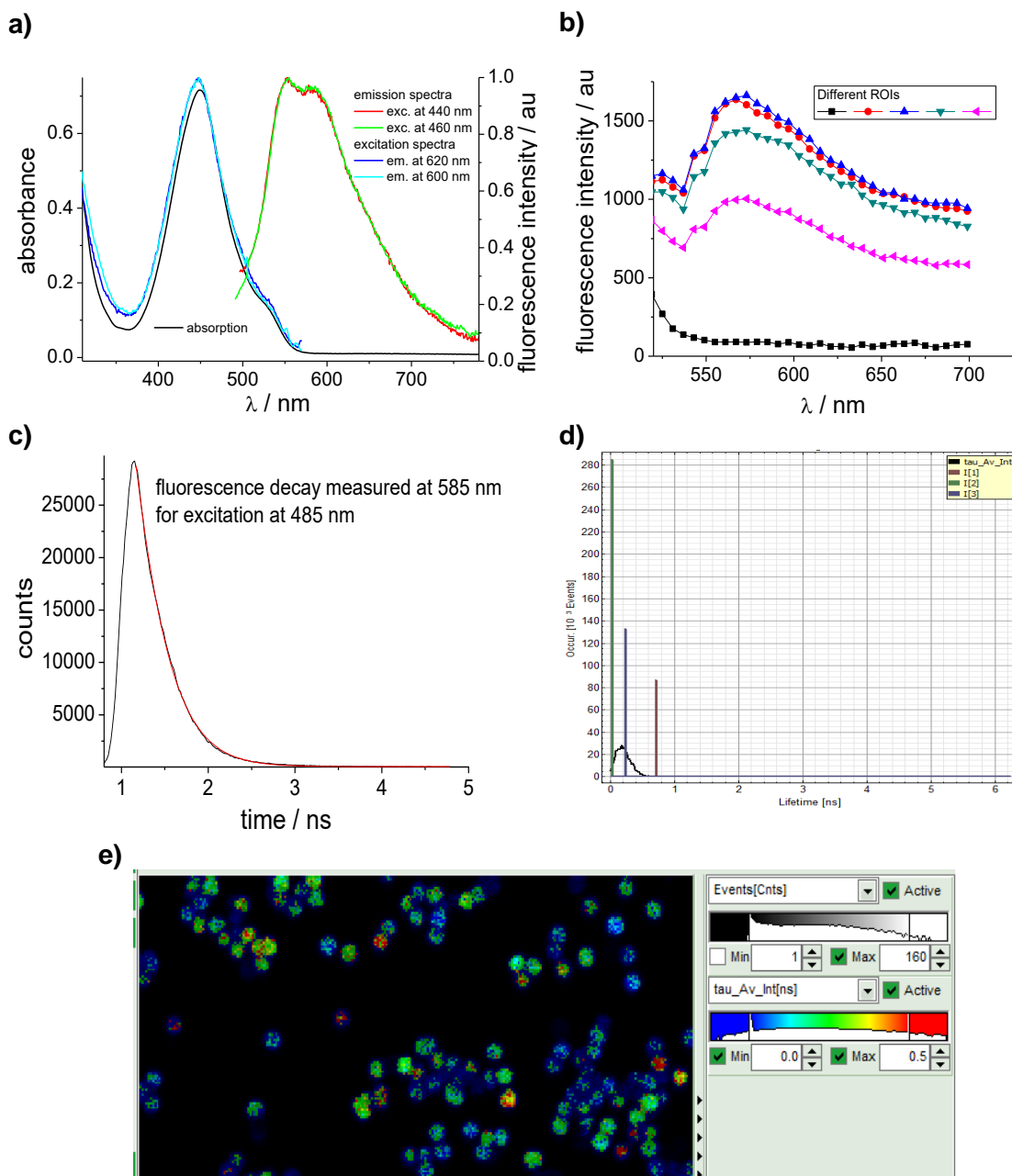
Figure 5.10 (**a**) Absorption and emission spectra of CLZ in DMSO; (**b**) Confocal fluorescence spectra of CLZ loaded in non-fluorescent NLAB3; black curve is the spectrum for a background ROI; (**c** and **d**) Fluorescence decay, calculated for selected ROI, of CLZ loaded in non-fluorescent NLAB3 and lifetime histogram after image fitting for CLZ in non-fluorescent NLAB8; excitation at 485 nm and emission measured in the 565-605 nm range; (**e**) FLIM image of NLAB8/CLZ with color corresponding to average lifetime ranging from 0 to 0.5 ns.

Figure 5.10b shows the spectra collected for ROI. We can discern a fluorescence spectrum similar to that of CLZ shown in Figure 5.10a. Fitting of the decay in Figure 5.10c yields two reliable lifetimes of 0.8, and 0.2 ns and one below the resolution (Figure 5.10d). This

is also in line with DMSO data. The 0.8 ns value is further supporting that we are not observing pure scattering. No lifetime components in the 5–11 ns range are present. Figure 5.10e shows the FLIM image of the particles evidencing the short average lifetime of ca. 0.2 ns. Importantly, the fluorescence decay behaviour can be successfully exploited as a promising tool to discriminate in a biological environment MSPs loading CLZ and not, when they release CLZ, by monitoring the average lifetime value in imaging experiments.
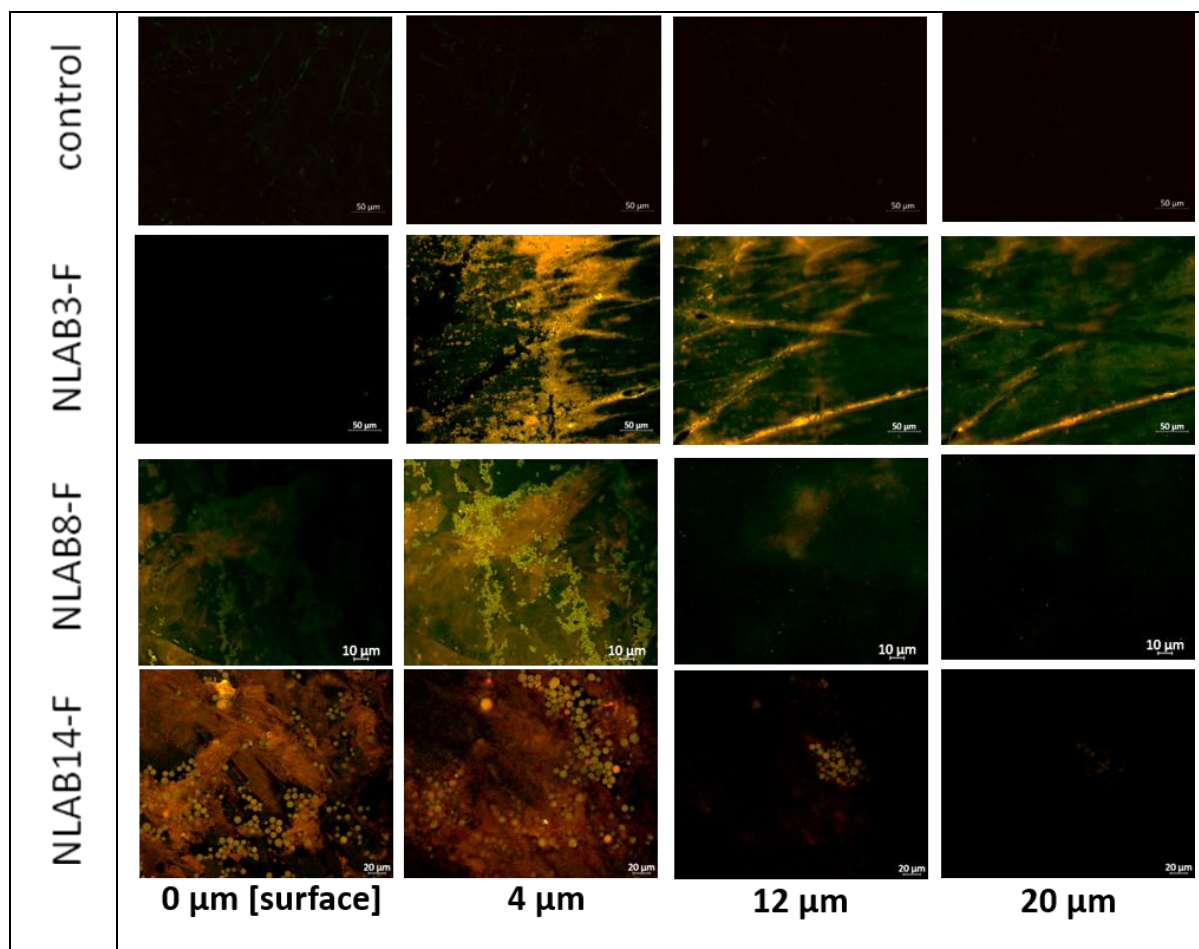
Figure 5.11 TPM data of full thickness human skin incubated with NLAB3-F, NLAB8-F, and NLAB14-F (2 mg/ml in PBS) using franz cell diffusion for 24 hours followed by rinsing with PBS. Images were retrieved from 3D volumes acquired in 1 μm z-stack images corresponding to 424 x 424 x 1 μm. 2D images at 0, 4, 12, and 20 μm depth through skin were chosen to demonstrate depth of penetration of MSPs.

Finally, we studied the distribution of fluorescent MSPs in mammalian skin by means of two-photon excitation fluorescence microscopy (TPM) at the University in Gothenburg. The luminescent MSPs were topically applied to mammalian skin samples using passive diffusion in Franz cell and the distribution was visualised using TPM. Human skin samples were collected from women after breast surgical operation. Figure 5.11 presents TPM spectral images taken at different depths through the human skin, starting at the surface (0 μm). The figure clearly demonstrates that distribution and penetration of luminescence MSPs depend on the particle size. The nanosized particles, *i.e.* NLAB3-F, were found

accumulating in the skin furrows down to a depth of 20 μm, whilst the microsize particles were limited to a penetration depth of around 12 μm. Interestingly, all particles were found to adhere with the corneocytes of stratum corneum after the washing procedure.

5.5 Drug release study of film

NLAB3, NLAB8, and NLAB14 with and without CLZ loaded chitosan films were prepared by solvent evaporation method. Around 5 mg of NLAB3-CLZ was dispersed in 0.75% and 1% chitosan solution prepared in 0.1M acetic acid and stirred overnight, and then propylene glycol 200 (0.5%) was added as a plasticizer. The resulting dispersion was degassed to remove the air bubbles and poured in the petri dish (15ml). This final dispersion was dried at $36^{o}C$ for more than 24 hours. The films formed in the petri dish were peeled off and stored at room temperature in a closed environment. These films were used at Gothenburg University to study MSPs particle penetration through the human skin using multiphoton microscopy.

NLAB3, NLAB8, and NLAB14 with and without CLZ loaded chitosan microcapsules were prepared by ionic gelation method. Around 5 mg of MSPs/CLZ was dispersed in 1% chitosan solution prepared in 0.1M acetic acid. 0.5 % Sodium tripolyphosphate has used as crosslinker for chitosan. Dropwise MSPs/CLZ loaded chitosan dispersion were added in 0.5 % Sodium tripolyphosphate aqueous solution on stirring using the syringe. NLAB3-CLZ loaded chitosan microcapsules were obtained and it was washed with water to remove the trace of crosslinker. It was dried and used for further study.

The drug release study was performed using Franz diffusion cell with PBS (pH 7.4) with 1.5% tween 20. Receptor compartment was filled with diffusion media. The prepared film was mounted on cellulose dialysis membrane (MW cut off 12,000 Da) and tightened with donor compartment using clamps. This assembly was kept stirring at room temperature for 12 hours. 3ml samples were withdrawn from the receptor compartment at fixed time intervals. Absorption spectra were recorded to calculate drug release. Sink condition was maintained by adding fresh media equivalent to sample amount withdrawn. Following this procedure, no drug release was observed and exploration of films and capsules was suspended.

5.6 Conclusions

We have studied luminescent label-free MSPs multifunctional drug nanocarrier for encapsulation of the hydrophobic drug, CLZ. The three types of MSPs (NLAB3, NLAB8 and NLAB14) display very appealing photophysical features for

theranostic applications as shown by our FLIM data. Moreover FLIM offers a tool to discern the CLZ release in a biological context as the average lifetime is significantly higher for unloaded particles. A first proof of concept was obtained by TPM imaging of the MSPs penetration in skin tissues.These fluorescent carriers loading CLZ are promising theranostic tools in view of development of new strategies for the treatment of bacterial infections.

5.7 References

1. J. M. Rosenholm, C. Sahlgren and M. Lindén, *Nanoscale*, **2010**, 2, 1870-1883.
2. S. Valetti, S. Mura, B. Stella and P. Couvreur, *J. Nanobiotechnology*, **2013**, 11, S6.
3. J. P. Celli, B. Q. Spring, I. Rizvi, C. L. Evans, K. S. Samkoe, S. Verma, B. W. Pogue and T. Hasan, *Chem. Rev.*, **2010**, 110, 2795-2838.
4. J. E. Lee, N. Lee, T. Kim, J. Kim and T. Hyeon, *Acc. Chem. Res.*, **2011**, 44, 893-902.
5. X. Xia, C. Zhou, L. Ballell and A. E. Garcia-Bennett, *ChemMedChem*, **2012**, 7, 43-48.
6. H. Chen, Z. Zhen, W. Tang, T. Todd, Y.-J. Chuang, L. Wang, Z. Pan and J. Xie, *Theranostics*, **2013**, 3, 650.
7. J. Chen, W. Liu, L.-H. Mao, Y.-J. Yin, C.-F. Wang and S. Chen, *J. Mater. Sci.*, **2014**, 49, 7391-7398.
8. Y. Ma, H. Liang, Y. Zeng, H. Yang, C.-L. Ho, W. Xu, Q. Zhao, W. Huang and W.-Y. Wong, *Chem. Sci.*, **2016**, 7, 3338-3346.
9. X. Peng, Z. Yang, J. Wang, J. Fan, Y. He, F. Song, B. Wang, S. Sun, J. Qu and J. Qi, *J. Am. Chem. Soc.*, **2011**, 133, 6626-6635.
10. H. Itoh, S. Arai, T. Sudhaharan, S.-C. Lee, Y.-T. Chang, S. i. Ishiwata, M. Suzuki and E. B. Lane, *Chem. Commun.*, **2016**, 52, 4458-4461.
11. A. Fraix, I. Manet, M. Ballestri, A. Guerrini, P. Dambruoso, G. Sotgiu, G. Varchi, M. Camerin, O. Coppellotti and S. Sortino, *J. Mater. Chem. B*, **2015**, 3, 3001-3010.
12. F. Doria, A. Oppi, F. Manoli, S. Botti, N. Kandoth, V. Grande, I. Manet and M. Freccero, *Chem. Commun.*, **2015**, 51, 9105-9108.
13. E. Baggaley, S. W. Botchway, J. W. Haycock, H. Morris, I. V. Sazanovich, J. G. Williams and J. A. Weinstein, *Chem. Sci.*, **2014**, 5, 879-886.
14. T. W. Prow, *Wiley Interdiscip. Rev.Nanomed.Nanobiotechnol.*, **2012**, 4, 680-690.
15. A. E. Garcia-Bennett, O. Terasaki, S. Che and T. Tatsumi, *Chem. Mater.*, **2004**, 16, 813-821.
16. C. Kresge, M. Leonowicz, W. Roth, J. Vartuli and J. Beck, *Nature*, **1992**, 359, 710-712.
17. K. Kusakabe, S. Sakamoto, T. Saie and S. Morooka, *Sep. Purif. Technol.*, **1999**, 16, 139-146.
18. S. Haque, M. R. Whittaker, M. P. McIntosh, C. W. Pouton and L. M. Kaminskas, *Nanomed. Nanotechnol. Biol. Med.*, **2016**, 12, 1703-1724.
19. Z. Bacsik, R. Atluri, A. E. Garcia-Bennett and N. Hedin, *Langmuir*, **2010**, 26, 10013-10024.
20. W. Liu, C. Li, Y. Ren, X. Sun, W. Pan, Y. Li, J. Wang and W. Wang, *J. Mater. Chem. B*, **2016**, 4, 5772-5788.
21. F. Messina, L. Sciortino, R. Popescu, A. Venezia, A. Sciortino, G. Buscarino, S. Agnello, R. Schneider, D. Gerthsen and M. Cannas, *J. Mater. Chem. C*, **2016**, 4, 2598-2605.

22. D. Pan, J. Zhang, Z. Li, C. Wu, X. Yan and M. Wu, *Chem. Commun.*, **2010**, 46, 3681-3683.
23. M. C. Skala, K. M. Riching, A. Gendron-Fitzpatrick, J. Eickhoff, K. W. Eliceiri, J. G. White and N. Ramanujam, *Proc. Natl. Acad. Sci. USA*, **2007**, 104, 19494-19499.
24. S. Ogikubo, T. Nakabayashi, T. Adachi, M. S. Islam, T. Yoshizawa, M. Kinjo and N. Ohta, *J. Phys. Chem. B*, **2011**, 115, 10385-10390.
25. Z. Qian, J. Ma, X. Shan, H. Feng, L. Shao and J. Chen, *Chem.-A Eur.- J.*, **2014**, 20, 2254-2263.
26. S. K. Bhunia, A. Saha, A. R. Maity, S. C. Ray and N. R. Jana, *Sci. Rep.*, **2013**, 3.
27. F. Doria, I. Manet, V. Grande, S. Monti and M. Freccero, *J. Org. Chem.*, **2013**, 78, 8065-8073.
28. C. M. O'Driscoll and O. I. Corrigan, *Analytical Profiles of Drug Substances and Excipients*, **1992**, 21, 75-108.

Chapter 6

Experimental Section

6.1 Electronic absorption spectroscopy

All the optical spectroscopic measurements were carried out at 295 K. Absorption spectra were recorded by means of a double beam spectrophotometer, in particular a Perkin-Elmer Lambda 650 or 950 spectrophotometer.Spectra were recorded in 2 cm, 1 cm, 0.5 cm or 0.2 cm path length cuvettes setting 1 nm steps, 266 nm/minute velocity and 2 nm bandpass and using water, water-alcohol mixture, PBS or CyD aqueous solutions as reference.
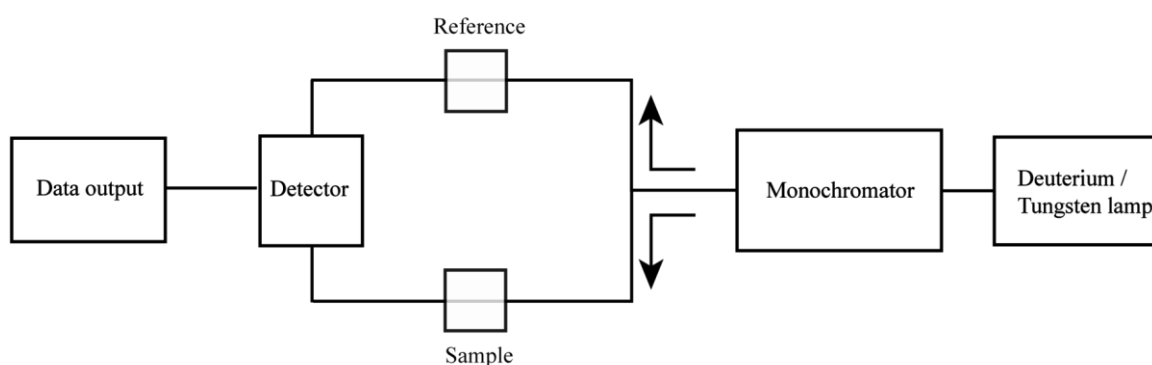

Figure 6.1 Schematic diagram of double beam spectrophotometer

UV-visible absorption spectra of fluorescent MSPs and CLZ loaded MSPs (chapter 5) were measured on Perkin-Elmer Lambda 950 spectrophotometer equipped with an integrating sphere to eliminate light scattering contribution of silica particles in the absorption spectra. All the measurements were recorded in a 1 cm path length cuvette at intervals of 1 nm, using water and buffer or unloaded silica particle suspensions as the reference.

6.2 Circular dichroism

Circular dichroism (CD) is based on the principle of differential absorption of left and right circularly polarised light by a chiral compound ($\Delta A = A_L - A_R$). Spectra are generally reported in terms of ellipticity, θ. The two circularly polarised components emerging from the chiral sample possess not only a phase difference but also different amplitudes. The polarisation of the radiation at the sample exit becomes elliptical, as the tip of the electric field vector, projected in a plane perpendicular to the travelling direction of the wave, describes an ellipse.
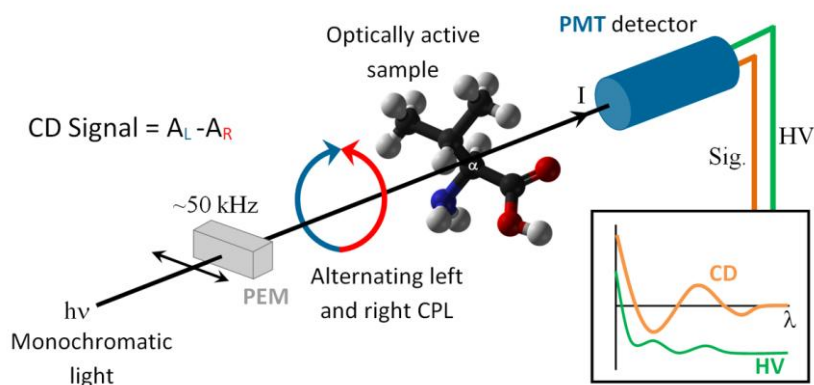
Figure 6.2 Schematic diagram of circular dichroism (PEM = phoelastic modulator based on quarter wave plate, PMT = photomultiplier tube)

The different absorption experienced by the two circularly polarised components is expressed by means of the ellipticity θ, defined as the angle whose tangent is equal to the ratio between the minor (*m*) and the major (*M*) axes of the ellipse

$$\tan \theta = m/M \qquad (6.1)$$

A CD signal will be observed when the chromophore is optically active due to intrinsic chirality or is placed in an asymmetric environment.[1] Circular Dichroism spectra were recorded with a Jasco J-715 spectropolarimeter. The spectra of the samples were registered using solvent or carrier solutions as the reference. 2 cm, 1 cm or 1 mm cuvettes were used depending on the concentration of the sample. Step size (generally 1 nm), band pass (2 nm in most cases), response time (0.5-1 s) and scanning speed (from 50 to 100 nm / minute) were optimised to improve the S/N ratio.

6.3 Fluorescence spectroscopy

Fluorescence spectra were measured on an Edinburgh FLSP920 spectrofluorimeter registering spectra with 1 nm steps and 1 s dwell time. Slits were kept as narrow as possible (1-4 nm band width) in excitation and emission. Right angle detection was used. The fluorescence measurements were carried out in a 1 cm quartz cuvette or triangular cuvette for solutions with high optical density. Steady state fluorescence spectra were registered in air-equilibrated solutions. The measurements were performed within few hours from sample preparation. Spectra were corrected for the wavelength depending response of the monochromator/PMT couple and for the excitation light intensity.
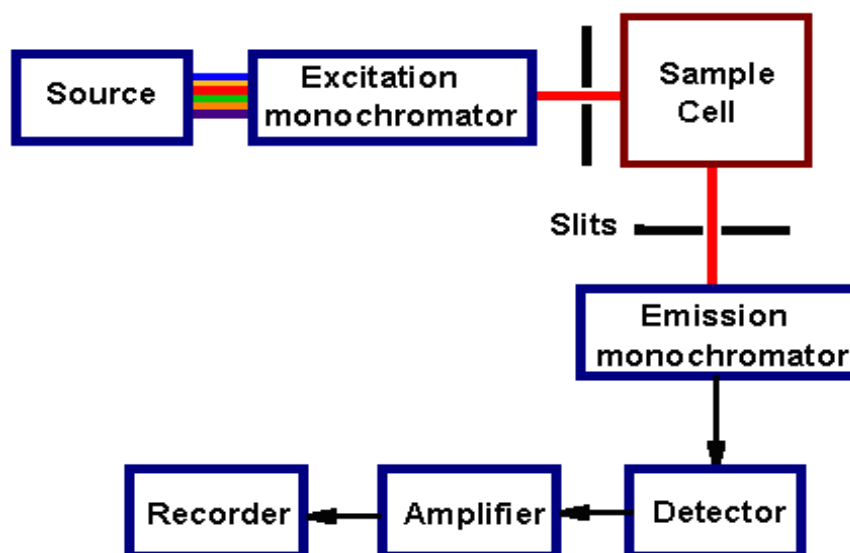
Figure 6.3 Schematic diagram of spectrofluorimeter

6.4 Time-correlated single photon counting

Fluorescence lifetimes were measured in air-equilibrated solutions with a time-correlated single photon counting system (TCSPC, IBH Consultants Ltd.). In chapter 2 and 4 a nanosecond LED source of 465 nm was used for excitation and the emission was collected at right angle at 520 or 530 nm (band width 2-16 nm) with a cut-off filter 495. An opaque glass plate is used to register the Instrument Response Function collecting photons at 500 nm using the 465 nm LED light source. 2000 counts were collected in the maximum intensity channel (channel width of 55 ps) corresponding to a total photon count ranging from 180,000 to 210,000 cts per decay. Photons were collected in 4094 channels.

In Chapter 3 a nanosecond LED source of 278 nm was used for excitation and emission was collected at 300 nm with band width of 16 and 32 nm for the booster study. 1000-2000 counts were collected in the maximum intensity channel (channel width of 55 ps) corresponding to a total photon count ranging from 13,000 to 34,000 cts per decay and photons were collected in 4094 channels.

The software package for the analysis of the emission decays was provided by IBH Consultants Ltd. Fluorescence intensity decay profiles were fitted using a mono- or multi-exponential function and deconvolution of the instrumental response function. Fitting yields both lifetime τ_i and pre exponential factor a_i of each emitting species.

$$I(t) = \sum_i a_i \times \exp(-t/\tau_i) \qquad (6.2)$$

The relative amplitude, also known as the fractional intensity, and the average fluorescence lifetime are calculated according to the following equations:

$$(6.3) \qquad f_i = a_i\tau_i / \Sigma_i \ a_i\tau_i \qquad\qquad (6.4) \quad \tau_{av} = \Sigma_i \ f_i\tau_i$$

6.5 Multiwavelength global analysis of titration data

The best complexation model, the binding constants and the spectra of the associated species were determined by multivariate global analysis of multiwavelength data from a set of spectra corresponding to different host-guest mixtures, using the program ReactLab^{TM} Equilibria (Jplus Consulting Pty Ltd). ReactLab^{TM} EQUILIBRIA provides global analysis for fitting the parameters of chemical reaction equilibria to multivariate spectroscopic titration data. The program, including all algorithms and the GUI (graphical user interface) frontend, has been developed in Matlab$^{@}$. All raw data, model entry and results output are organised in Excel Workbooks, which are launched from and dynamically linked to the ReactLab^{TM} application. Excel provides a spreadsheet format for all experimental data and analysis results, as well as the interface for entering chemical equilibria models and all fit related parameters and numerical analysis options. A saved workbook contains all information and settings associated with the analysis session as well as the numerical data and results. Launching of the fitting procedure initiates the data fitting algorithm which proceeds in the attempt to minimise the residual square sum (or ssq) which is a measure of the difference between the real data and that predicted by the current model and prevailing parameters. It does this by iteratively refining the free parameters of the model using an adaptation of a Marquardt-Levenberg algorithm and adjusting the 'coloured' spectra, according to a least squares criterion.[2] The same software has been used in chapter 2 to determine the pK of monoanionic fluorescein covalently linked to a βCyD polymer.

6.6 Time-resolved confocal fluorescence microscopy

Confocal fluorescence imaging was performed on an inverted Nikon Ti-E microscope (Nikon Co., Shinjuku, Japan). The confocal fluorescence microscope Nikon A1 is equipped with an Argon ion CW laser and a 640 nm CW diode laser as well as 405, 485 and 640 nm pulsed/CW diode lasers (PicoQuant GmbH, Berlin, Germany). Images were collected using a Nikon Plan Apo VC 60X oil immersion objective with NA 1.40. The technique has been used to study mesoporous silica particles (MSPs) reported in chapter 5. Filters were set to register the fluorescence of MSPs in the 460–500 nm, 500–550 nm and 565–605 nm ranges and the fluorescence of CLZ in the 565–605 nm range. Fluorescence lifetime imaging was performed exciting with the pulsed 405 or 485 nm diode laser and collecting photons using integrated PicoHarp 300 electronics (PicoQuant GmbH, Berlin,

Germany) for TCSPC measurements. Histograms of the collected photons consist of 1600 channels each with 16 ps width. Two single-photon avalanche diode detectors equipped with a bandpass filter were used as detectors. The repetition rate of the pulsed excitation was 40 MHz. The instrument response function of the system is approximately 220 ps. The fluorescence decay fit was performed on the histogram calculated for a region of interest corresponding to the selection of silica particles in the sample image. The fluorescence decay profile was analysed using a least-squares method, applying bi- or tri-exponential decay functions provided by Picoquant SymPhoTime software. Software calculated Instrumental Response Function was used for deconvolution. The FLIM image was created fixing the lifetimes values obtained from the global decay analysis and calculating the pre-exponentials in each pixel.

6.7 DLS particle size and zeta potential measurements

The particle hydrodynamic diameter and zeta potential was measured using NanoBrook Omni analyzer from Brookhaven Instruments Corporation. To measure the Zeta potential NanoBrook Omni relies on phase analysis light scattering (PALS) to determine the electrophoretic mobility of charged colloids like nanoparticle solutions. Unlike Laser Doppler Velocimetry (LDV), the PALS technique does not require the application of large fields which may result in thermal problems or denaturation. Indeed to measure the phase shift, the particles need only to move a fraction of their own diameter to yield good results. Zeta potential measurements are performed using the 15° detection angle to minimise diffusion broadening. Five measurements were recorded in the repetitive mode for each sample and mean value with standard deviation has been reported.

Average particle size distributions were measured by means of dynamic light scattering with the NanoBrook Omni analyzer at a fixed scattering angle of $90°$ at $25°C$ temperature. The hydrodynamic diameter was calculated applying an autocorrelation function to the scattered light intensity profile considering the particles as spheres.[3] Laser light was used in the scattering experiment. All measurements were carried out in duplicate for reproducibility. Disposable glass cuvette was used for DLS measurement.

6.8 AF4-MALS analysis

AF4-MALS was performed by using a 1100 Series HPLC system (Agilent Technologies, Palo Alto, CA), connected to a control module to control AF4 flow rates and operations (Eclipse 3, Wyatt Technology Europe, Dernbach, Germany). Online detection of the eluted

species was performed with an Agilent 1100 DAD UV/Vis spectrophotometer, a MALS DAWN HELEOS detector (Wyatt Technology Corporation, Santa Barbara, CA) and an Optilab T-rEX refractive index detector (Wyatt Technology Corporation). Carrier solutions were degassed using an online vacuum degasser Agilent, 1100 series (Agilent Technologies).

The separation device is constituted by a flat channel with a trapezoidal shape and capillary height. For the sample analysis, particles are introduced in the channel and focused, allowing the sample to concentrate on a narrow band. When the elution starts, the separation is gained by the combination of a longitudinal and a perpendicular hydrodynamic field. The channel was 152 mm long (Wyatt Technology Europe), equipped with a polyethersulfone membrane (Nadir), with a molecular weight cutoff of 10 kDa. The channel spacer was 350 μm tick, with trapezoidal shape (upstream width b0 = 16 mm; downstream width bL = 4 mm).[4]
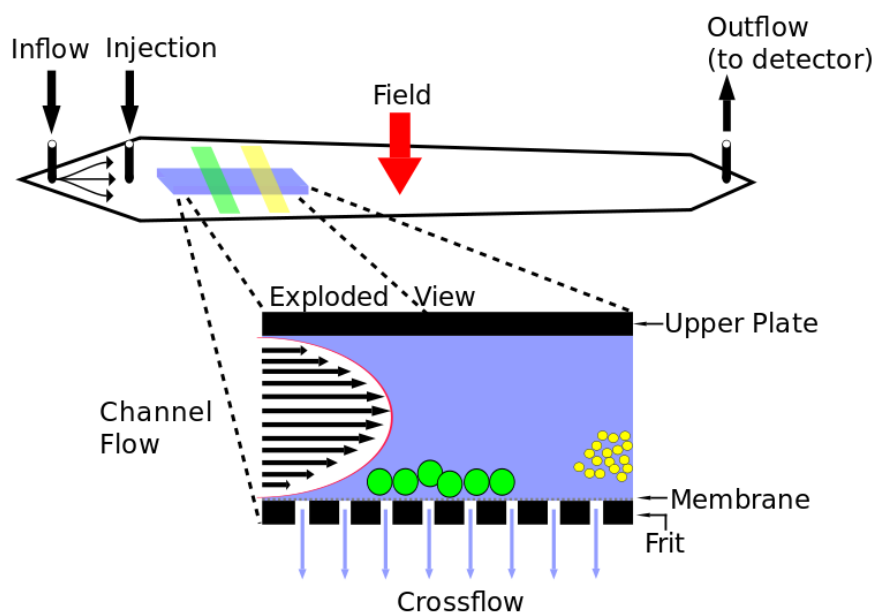

Figure 6.4 schematic diagram of asymmetric flow field flow fractionation (AF4)

6.9 RP-HPLC analysis

The equipment consisted of an Agilent HPLC system (Agilent 1100 Series) equipped with a C18 column (Kinetex 5 u C18, 100 A, Phenomenex) and an UV detector working at 280 nm. It has been used to obtain phase diagrams for ETH and booster 43266 in chapter 3. The chromatographic conditions were the following: solvent A 0.1% Trifluoroacetic Acid (TFA) in MilliQ water and solvent B 0.1% TFA in acetonitrile; 0–2 min: 0%–20% B, 2–6 min: 20%–45% B, 6–10 min: 45%–75% B, 10–15 min: 75%–0%. Flow rate: 1.0 ml/min at

room temperature. ETH and BDM43266 were simultaneously quantified using RP-HPLC analysis.

6.10 Viscometer and Microsprayer

Viscometer (Fungilab, expert series) was used to measure the viscosity of pβCyD NPs alone or containing ETH. Data are expressed in centipoise (cP). pβCyD NPs at a fixed concentration of 150 mg/ml alone or containing 2.97 0.1 mg/ml of ETH were transferred in a glass tube to determine the viscosity at room temperature.

MicroSprayer Aerosolizer (Model IA-1C-M and FMJ-250 High Pressure Syringe, Penn Century Inc., Wyndmoor, PA) was used in order to evaluate the possibility to use pβCyD NPs containing the combination for a future intrapulmonary administration, pβCyD NPs alone or containing ETH and BDM43266 were firstly filtered by a 0.22mm filter (Regenerated Cellulose, 0.22mm) and then passed through a MicroSprayer.

6.11 References

1. N. Berova, K. Nakanishi and R. Woody, *Circular dichroism: principles and applications*, John Wiley & Sons, 2000.
2. H. Gampp, M. Maeder, C. J. Meyer and A. D. Zuberbühler, *Talanta*, **1985**, 32, 95-101.
3. R. Xu, *Particuology*, **2008**, 6, 112-115.
4. B. Roda, A. Zattoni, P. Reschiglian, M. H. Moon, M. Mirasoli, E. Michelini and A. Roda, *Anal. Chim. Acta*, **2009**, 635, 132-143.

Final Remarks

The research of this thesis inserts in the nanomedicine field dealing with drug development and delivery. My research mainly focused on two antibiotics, ETH and CLZ, both facing severe problems due to their dose-dependent toxicity and low water solubility. Our objective was to identify alternative routes for their administration to pave the way for their upgrade to first-line drugs for the treatment of bacterial infections, in particular those due to MDR bacteria. Our approach was based on the use of nanosize materials with different chemical nature as drug carriers. In particular, we tried several CyD- and silica-based nanomaterials for the encapsulation of ETH and CLZ. We used different optical spectroscopic techniques like UV-Visible absorption, circular dichroism, steady-state and time-resolved fluorescence, in combination with DLS, AF4-MALS and other analytical technique to investigate the interaction of the drug with the carrier.

As to ETH encapsulation in a βCyD monomer and polymer, the polymer behaves better as it solubilises much higher drug amounts in pure water. ETH locates inside the βCyD cavity and inserts also in other microdomains of the polymeric NP. Encapsulation in the polymer prevents ETH crystallization which is one major drawback in formulating ETH. Concerning the co-encapsulation of ETH and organic booster in the pβCyD polymer our study evidenced that there is no competition between the two molecules both complexed in the polymeric NP. This formulation is very promising for microspray application in the treatment of MDR tuberculosis to enhance ETH efficacy with respect to ETH conventional administration.

Secondly, we investigated SBE-βCyD carriers for the encapsulation of CLZ. We performed molar mass determination of the two polymers, assessed the CLZ solubility and loading in the presence of the carriers, as well as the particle size before and after drug loading. We were able to obtain organic solvent-free solutions of the highly hydrophobic CLZ dissolved with the CyD-based carriers in water. CLZ/SBE-βCyD carrier systems were evaluated *in vitro* against *S. epidermidis* and some clinical MDR isolates. CLZ in the carrier has very appealing MIC values in the nanomolar range against all assayed *S. epidermidis* strains and does not exhibit any cytoxocity differently from the free drug. The SBE-βCyD polymeric carrier loaded with CLZ is a very promising system for *in vivo* testing in the next future.

In view of theranostic applications mesoporous silica particles (MSPs) endowed with intrinsic fluorescence were evaluated as CLZ encapsulating agent. In-depth photophysical characterisation evidenced that the MSPs in liquid and solid state exhibit very interesting fluorescence features, in particular absorption and emission in the visible as well as long fluorescence lifetimes, that make them an appealing tool for imaging. Successful encapsulation of amorphous CLZ in three types of MSP with different porosity was achieved. CLZ/MSPs have much shorter fluorescence lifetimes thus affording a tool that allows monitoring drug release in more complex biological environments.

In conclusion, this research has been successful in achieving new carrier systems based on nanomaterials with the potential of driving innovation in the field of known drug delivery.

List of the publication and presentation

1. **J. Wankar**, G. Salzano, E. Pancani, G. Benkovics, M. Malanga, F. Manoli, R. Gref, E. Fenyvesi and I. Manet, **"**Efficient loading of ethionamide in cyclodextrin-based carriers offers enhanced solubility and inhibition of drug crystallization**"** *Int. J. Pharm.*, **2017**, 531, 568-576.

2. G. Salzano, **J. Wankar**, S. Ottani, B. Villemagne, A. R. Baulard, N. Willand, P. Brodin, I. Manet and R. Gref, **"**Cyclodextrin-based nanocarriers containing a synergic drug combination: A potential formulation for pulmonary administration of antitubercular drugs**"** *Int. J. Pharm.*, **2017**,531, 577-587.

3. S. Valetti, **J. Wankar,** M. B. Ericson, A. Feiler and I. Manet, **"**Mesoporous silica particles as lipophilic drug vehicle investigated by fluorescence lifetime imaging**"** *J. Mater. Chem. B*, **2017**, 5, 3201-3211.

4. F. Sciscione, F. Manoli, E. Viola, **J. Wankar,** C. Ercolani, M. P. Donzello and I. Manet, "Photoactivity of New Octacationic Magnesium(II) and Zinc(II) Porphyrazines in a Water Solution and G-Quadruplex Binding Ability of Differently Sized Zinc(II) Porphyrazines" *Inorg. Chem.*, **2017**, 56, 12795-12808.

Oral presentation

J. Wankar, G. Salzano, E. Pancani, R. Gref and I. Manet, **"**New nanocarriers for the delivery of old antibiotics: spectroscopic study of the affinity of the drugs**"** *Italian Photochemistry Meeting*, 17-19 Dec 2015, Bologna, Italy.

Poster presentation

J. Wankar, I. Manet and R. Gref, **"**Nanocarriers for the delivery of antimicrobial agents to fight resistance mechanisms**"** *NanoItaly*, 21-24 Sept 2015, Bologna, Italy.